A Measurement of the Branching Ratio of the Weak Radiative Hyperon Decay

Cascade-Zero to Lambda Gamma

Catherine Chase James

Under the supervison of Professor Kenneth Heller

Abstract

The branching ratio $\Xi^\circ \to \Lambda\gamma / \Xi^\circ \to \Lambda\pi^\circ$ has been measured at the Fermilab National Acceleator Laboratory neutral hyperon facility. 30,000 $\Xi^\circ \to \Lambda\pi^\circ$ decays were detected by identifying the subsequent $\Lambda \to p\pi^-$ and $\pi^\circ \to \gamma\gamma$ decays in a multiwire proportional chamber magnetic spectrometer and an array of lead glass. A sample of 6.7×10^5 $\Lambda+\gamma$ events were analyzed for $\Xi^\circ \to \Lambda\gamma$ decays. A sample of 139 ± 12 $\Xi^\circ \to \Lambda\gamma$ decays were identified. Monte Carlo studies gave the relative acceptances of the two decay types in the apparatus, and in turn the branching ratio. The branching ratio is $1.27 \pm 0.11 \times 10^{-3}$, with a possible systematic error of $\pm 0.22 \times 10^{-3}$.

ACKNOWLEDGEMENTS

I would like to thank Ken Heller for introducing me to high energy physics, and for his patience, tolerance, and continuous support as my thesis advisor. The topic of this thesis was suggested by Oliver Overseth, whose experiences at CERN led him to believe that hyperon radiative decays were worth pursuing in the Fermilab hyperon experiments.

I would also like to thank the members, present and past, of the Neutral Hyperon Group at Fermilab who contributed to this experiment. Of particular importance on the way to becoming a physicist were the discussions, arguments, explanations, criticisms, and all other wisdoms from : Andy Beretvas, Pete Border, Tom Devlin, Bob Handler, K. Biu Luk, Byron Lundberg, Gina Rameika, Prisca Petersen, Lee Pondrom, Gordon Thomson, and last but not least, Marleigh Sheaff.

The experiment would not have been possible without the support of the Fermilab staff, especially those of the Proton Lab.

Above all, I would like to thank my parents for the support and encouragement they have given me throughout my academic career.

TABLE OF CONTENTS

LIST OF TABLES

LIST OF FIGURES

Chapter 1

Introduction

The Weinberg-Salam model of electro-weak interactions is one of the most successful theories in recent physics. The model's successes appear, however, only when it is applied to problems where the electro-weak interaction alone is at work. There are some long-standing weak interaction problems that have not yet been solved, among them the $\Delta I=1/2$ selection rule, CP violation, and non-leptonic decays of hyperons. All of these problems involve weak interaction processes acting in the presence of strong interactions. Strong interactions are not yet well understood, and the models developed, like QCD, present many technical difficulties for calculations. The weak radiative decay modes of hyperons offer a simple system in which to study the effects of strong interactions on weak decays.

Hyperons are the class of baryons containing strange quarks. The lowest mass hyperons decay through the weak interaction, with strangeness changing by +1, and all have the long lifetime, $\sim 10^{-10}$ sec., associated with weak decays. The only exception is the decay $\Sigma^{\circ} \rightarrow \Lambda\gamma$, which is an electromagnetic decay and has a lifetime $7.6 \pm 0.5 \pm 0.7 \times 10^{-20}$ sec[1]. Table 1.1 shows the lowest lying hyperons, their quark content, the dominant decay modes with their branching fractions or ratios, and the weak radiative decay modes.

The dominant weak decay modes always involve a baryon and a meson in the final state. The decay diagrams are of the type shown in Fig. 1.01, which have a recombination of the quarks in the final

Table 1.1 [22]
Properties of Hyperons

hyperon	mass GeV	lifetime sec	quarks	dominant decay mode	branching ratio	rare radiative decay mode
Λ	1.1156	2.632×10^{-10}	u d s	$p\pi^-$ $n\pi^\circ$	64.2% 35.8	$n\gamma$
Σ^+	1.1894	0.8×10^{-10}	u u s	$p\pi^\circ$ $n\pi^+$	51.64% 48.36	$p\gamma$
Σ°	1.1192	5.8×10^{-20} (1) $7.6\pm0.5\pm0.7\times10^{-20}$	u d s	$\Lambda\gamma$	100%	electromagnetic (no weak decay)
Σ^-	1.1973	1.482×10^{-10}	d d s	$n\pi^-$	100%	no radiative decay mode
Ξ°	1.3149	2.90×10^{-10}	u s s	$\Lambda\pi^\circ$	~100%	$\Lambda\gamma$ $\Sigma^\circ\gamma$
Ξ^-	1.3213	1.641×10^{-10}	d s s	$\Lambda\pi^-$	~100%	$\Sigma^-\gamma$
Ω^-	1.6725	0.819×10^{-10}	s s s	ΛK^- $\Xi^\circ\pi^-$ $\Xi^-\pi^\circ$	68.6% 23.4 8.0	$\Xi^-\gamma$

state into the daughter particles. The radiative decays, on the other hand, are less complex. They involve only a single baryon in the initial and final states, and a photon is emitted. Precisely how the decays occur, however, is not at all obvious. The parent and daughter particles in the hyperon radiative decays differ in makeup by only one quark: a strange quark appears to have converted into a down quark plus a γ. Such a process would be a strangeness-changing neutral current if it occured directly; these currents are strongly suppressed by the GIM[2] mechanism and have not been observed.

The hyperon radiative decays have been of theoretical interest for some time, because of their simplicity compared to other hyperon decays. The experimental data, however, have been sparse, so there are not many checks on the predictions from any model. The theory should be able to predict particle properties, such as branching ratios and decay asymmetries, from first principles. There are two complementary types of models used to describe the decays, long distance pole models, and short distance quark level models.

The first theoretical work on the subject, which predicted the decays, appeared in 1956.[3] This first paper and subsequent works on non-leptonic hyperon decays described the decays in terms of current algebra and pole models. These were phenomenological models which looked at long distance effects, outside the range of what is known today as quark confinement.[4] Fig. 1.02 shows typical pole diagrams for a radiative hyperon decay; the initial hyperon is changed to an intermediate baryon followed by the radiation of a photon, or visa-versa. Models of this type gave branching ratios of the right order of magnitude, but the measured asymmetry for $\Sigma^+ \rightarrow p\gamma$ was not predicted. The reason was that the pole models were structured in such a way that if only left-handed currents were used, the parity-violating amplitude vanished. A decay asymmetry implies a parity-violating amplitude in the decay. Some models used that result as an argument to introduce right-handed currents,[5] but these were later shown not to work.[6] In the last few years, pole models have been re-examined with the inclusion of new intermediate states[7] and QCD bag model corrections.[8] A good summary of work to date on long distance models, and on non-leptonic hadronic decays in general, can be found in Ref. 9.

Models using short-distance analyses appeared in the mid 1970's. These models attempted to

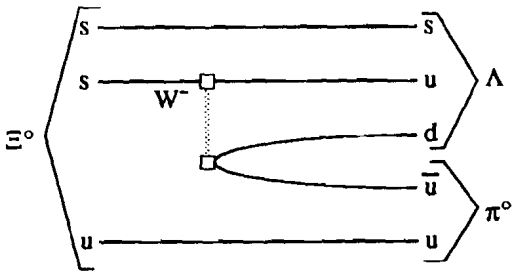

Fig. 1.01 : Diagram for the weak decay of a Ξ° to a Λ and a π°. The s's, u's and the d all represent quarks. W is the boson which carries the weak force.

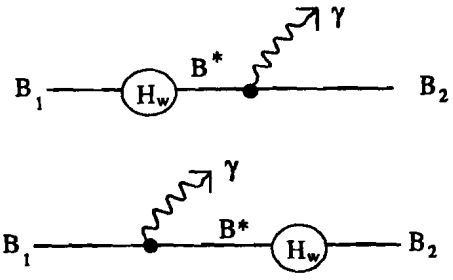

Fig. 1.02 : Pole diagrams for a hyperon radiative decay. H_w is the weak force Hamiltonian, B_1 is the initial baryon, B_2 is the final baryon, and B* is an intermediate baryon state.

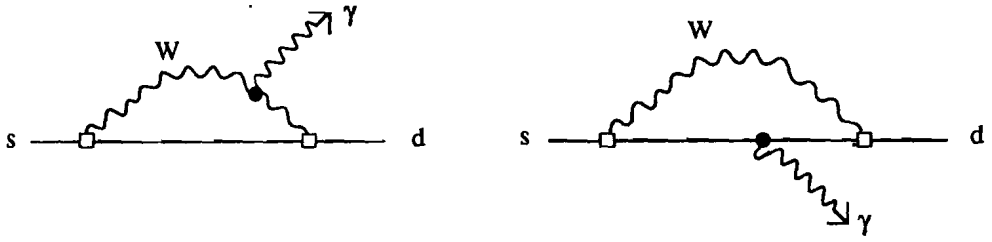

Fig. 1.03 : Single quark transition models. The W boson line connects a single quark line, and mediates the transition of an s quark directly to a d quark plus a photon.

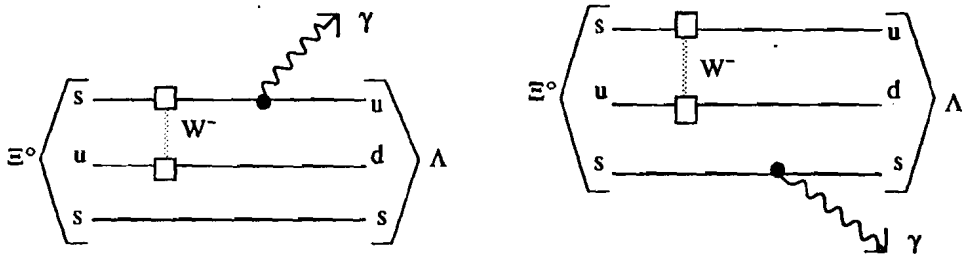

Fig. 1.04 : Two and three quark transition models. The W line connects two quark lines, mediating flavor changes s→u and u→d. In the two quark model, the gamma is radiated from one of the two active quark lines; in the three quark model it is radiated from the spectator quark line.

understand the decays at the level of the quarks and leptons. In general, the models found local operators which corresponded to the amplitude for the transition of an s quark to a d quark plus a photon. At first only single quark transition operators, as in Fig.1.03, were investigated. Single quark transition models were ruled out when it was shown that the general method gave results inconsistent with the data for $\Sigma^+ \rightarrow p\gamma$ and $\Xi^- \rightarrow \Sigma^-\gamma$ decays.[10] Subsequent papers[11] used two and three quark transitions, such as those in Fig. 1.04.

The next step was to add strong interaction corrections to the weak interaction hamiltonian. The first applications of QCD corrections to weak decays, which included the penquin diagram[6] in Fig.1.05, showed an enhancement of the $\Delta I=1/2$ part of the effective hamlitonian over the $\Delta I=3/2$ part, something that had never before come out of first principles.[6],[12] The most recent work on hyperon radiative decays uses this type of short distance analysis with QCD corrections. Vertices of the type in Fig. 1.06, $s \rightarrow d+\gamma+$gluon or s+gluon$\rightarrow d+\gamma$, are examined, using either using a lattice[14], or a QCD bag model.[13]

Table 1.2 gives predictions from some of the references cited, compared to the data available at the time of their publication. All these models used data from $\Sigma^+ \rightarrow p\gamma$ measurements to fix free parameters. The history of these measurements is given in Table 1.3 As can be seen, prior to this experiment, the only significant samples of hyperon radiative decays were from $\Sigma^+ \rightarrow p\gamma$ experiments. All the branching ratios are on the order of tenths of a percent.

The major problem in any of these experiments is to separate the rare radiative decay mode from a backround of one or more of the dominant decay modes. The task is made more difficult by the fact that the radiative and dominant decay modes often differ by only a single daughter particle; most often they differ by a single γ, one from the radiative decay versus two γ from a π°. An experiment's ability to separate the radiative decays from a background of the dominant decays will depend on the design of the experiment. So far there have been few experiments dedicated solely to the detection of radiative hyperon decays. Most of the data come from experiments designed for other purposes, whose data acquisition did not exclude the detection of radiative decays.

The experiment reported here is one of the class which was not initially designed to detect a rare

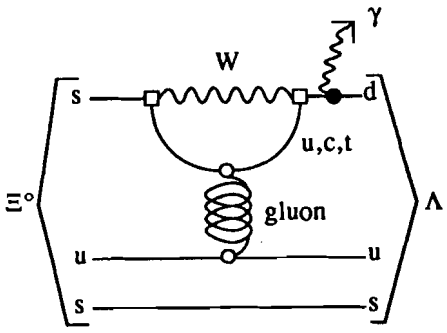

Fig. 1.05 : The penquin diagram. Somewhat similar to a single quark transition, but now strong interactions are introduced through the gluon exchange between the u quark line and the virtual u,c,t quark line.

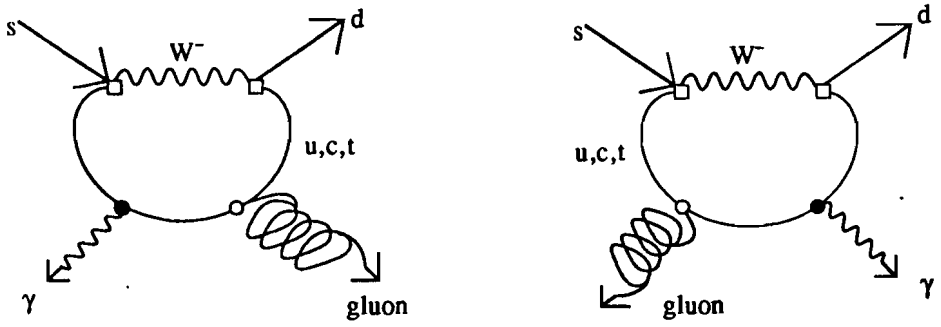

Fig. 1.06 : Modified penquin diagram. The gamma is now radiated from the virtual u,c,t quark line.

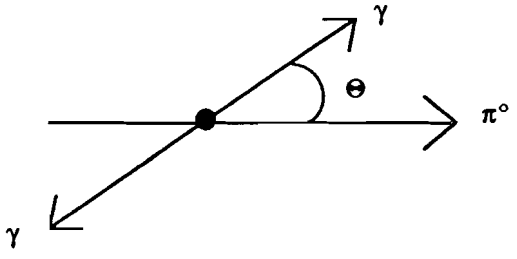

Fig. 1.07 : The π° center of mass system. The π° line shows the π° boost direction in the lab reference frame. Θ is the angle between the γ's from the π° decay and the boost direction.

Table 1.2

Predictions

Authors and reference #	predicted branching ratio x 10^{-3}		measured branching ratio used by the author(s) x10^{-3}
Gilman and Wise (10)			
$\Sigma^+ \to p\gamma$	1.24	input	1.24 ± 0.18
$\Lambda \to n\gamma$	22		none
$\Xi^\circ \to \Sigma^\circ\gamma$	9.1		< 70
$\Xi^\circ \to \Lambda\gamma$	4.0		5 ± 5
$\Xi^- \to \Sigma^-\gamma$	10		< 1.2
$\Omega^- \to \Xi^-\gamma$	41		none
Eckert and Morel (11)			
$\Sigma^+ \to p\gamma$	1.17	input	1.17 ± 0.14
$\Lambda \to n\gamma$	0.82		none
$\Xi^\circ \to \Sigma^\circ\gamma$	1.1		< 70
$\Xi^\circ \to \Lambda\gamma$	0.12		5 ± 5
Kamal and Verma (11)			
$\Sigma^+ \to p\gamma$	1.24	input	1.24 ± 0.18
$\Lambda \to n\gamma$	1.70		none
$\Xi^\circ \to \Sigma^\circ\gamma$	0.23		< 70
$\Xi^\circ \to \Lambda\gamma$	1.36		5 ± 5
$\Xi^- \to \Sigma^-\gamma$	1.20		< 1.20
$\Omega^- \to \Xi^-\gamma$	0.60		none
Rauh (8)			
$\Sigma^+ \to p\gamma$	0.82		1.17 ± 0.14
$\Lambda \to n\gamma$	1.02		none
$\Xi^\circ \to \Sigma^\circ\gamma$	5.87		< 70
$\Xi^\circ \to \Lambda\gamma$	2.29		5 ± 5

hyperon radiative decay. Experiment 619 at Fermilab was a measurement of the $\Sigma^\circ-\Lambda$ transitionmagnetic moment by Primakoff production of Σ°. It was performed during March to June 1982 in the Proton Center beam line. The Σ° transition magnetic moment was measured through the production cross-section of Σ° by Λ via the Primakoff effect. A beam of Λ's was required to produce Σ°, and the experimental apparatus detected the subsequent $\Sigma^\circ\rightarrow\Lambda\gamma$ decay. The results of the Σ° part of the experiment are given in References 1 and 15.

A description of the apparatus is contained in Chapter 2. The componets for Σ° detection also provided the necessary ingredients for $\Xi^\circ\rightarrow\Lambda\gamma$ detection. One difference was that the Σ° experiment required the resolution of three drift chambers, not needed or used in the analysis of these results. The incoming neutral beam contained Ξ° as well as Λ, and nothing in the apparatus discriminated between the decays $\Sigma^\circ\rightarrow\Lambda\gamma$ and $\Xi^\circ\rightarrow\Lambda\gamma$. The dominant decay $\Xi^\circ\rightarrow\Lambda\pi^\circ$ was also detected because the γ detection did not distinguish between a single γ or two γ's from π° decay. This experiment detected about $1\text{x}10^5$ fully reconstructed $\Xi^\circ\rightarrow\Lambda\pi^\circ$ decays. If one assumes the acceptances in the experiment for $\Xi^\circ\rightarrow\Lambda\pi^\circ$ and $\Xi^\circ\rightarrow\Lambda\gamma$ decays are roughly equal, then based on the only previous measurement[16] we would expect to obtain several hundred $\Xi^\circ\rightarrow\Lambda\gamma$ decays. Many of the $\Xi^\circ\rightarrow\Lambda\pi^\circ$ decays in the apparatus had only one γ detected, making the event topology appear as a $\Lambda+\gamma$ decay. When the invariant mass of the $\Lambda+\gamma$ is calculated, most of the events do not reach the region of the Ξ° mass. The missing γ from the π° decay carries off too much energy. Some proportion of π°'s decay, however, so that the angle Θ in Fig. 1.07 between the π° direction and the emitted γ's is small. In that case, one of the γ's has almost all the momentum of the π°. The $\Lambda+\gamma$ mass is closer to the $\Lambda+\pi^\circ$ mass, and the events of this type could overlap the mass region occupied by real $\Xi^\circ\rightarrow\Lambda\gamma$ decays.

Identifying the characteristics that could separate background $\Xi^\circ\rightarrow\Lambda\pi^\circ$ decays from signal $\Xi^\circ\rightarrow\Lambda\gamma$ decays depended upon a detailed computer simulation of the experiment, known as a Monte Carlo. Detected $\Xi^\circ\rightarrow\Lambda\pi^\circ$ decays were used to develop a $\Xi^\circ\rightarrow\Lambda\pi^\circ$ Monte Carlo. In the simulation, a particle was generated with the mass of the Ξ° and a momentum (magnitude and direction) matching that of the detected Ξ°. The particle decayed in flight to a Λ and π°, and their momenta were calculated from the

Table 1.3

Measured Results

decay	# events	branching ratio $x10^{-3}$	group
$\Sigma^+ \to p\gamma$	1	<0.68	Cartara et al., PL **12**, 72 (1964)
	24	3.7±0.8	Bazin et al., PRL **14**, 154 (1965)
	4	1.7	Quareni et al., NC **40a**, 928 (1965)
	45	2.1±0.3	Ang et al., Z. Phys. **228**, 151 (1969)
	31	2.76±0.51	Gershwin et al., PR **188**, 2077 (1969)
	35	2.11±0.38	Manz et al., PL **96B**, 217 (1980)
	155	2.46±0.32	Biagi et al., Z. Phys. **C 28**, 495 (1985)
	194±25	α only	K. Miyake et al., Intl. Sym. on Lepton-Photon Interactions at High Energies, Kyoto, 1985
$\Xi^\circ \to \Lambda\gamma$	1	5±5	Yeh et al., PRD **10**, 3545 (1974)
$\Xi^\circ \to \Sigma^\circ\gamma$	0-1	<65	Yeh et al., PRD **10**, 3545 (1974)
$\Xi^- \to \Sigma^-\gamma$	0	<1.5	Yeh et al., PRD **10**, 3545 (1974)
	11	0.23±0.10	Biagi et al., Z. Phys. **C 35**, 143 (1987)
$\Omega^- \to \Xi^-\gamma$	0	<3.1	Bourquin et al., PL **88B**, 192 (1979)
$\Lambda \to n\gamma$	31	1.02±.33	Biagi et al., Z. Phys. **C 30**, 201 (1986)

relativistic kinematics of two body decays. The $\Lambda \rightarrow p\pi^-$ and $\pi^\circ \rightarrow \gamma\gamma$ decays were carried out in the same fashion. Given starting positions and momenta, the particles could be projected through the apparatus of the experiment, and their location in each of the detection devices found. The simulated events were then analyzed through the same process as the data to recover the Ξ°. The details of the Monte Carlo simulation are discussed in section 3.40. Once the $\Xi^\circ \rightarrow \Lambda\pi^\circ$ Monte Carlo reproduced the data well, the same basic Monte Carlo could be used to generate $\Xi^\circ \rightarrow \Lambda\gamma$ decays. The $\Xi^\circ \rightarrow \Lambda\gamma$ signal Monte Carlo events gave the only information on the behavior of these decays in the apparatus, and how one might separate them from backround $\Xi^\circ \rightarrow \Lambda\pi^\circ$ decays.

Chapter 2 describes the apparatus of the experiment. Chapter 3 covers the basic event reconstruction: detection of Λ decays and γ shower identification. The reconstruction of $\Lambda\gamma\gamma$ events to $\Xi^\circ \rightarrow \Lambda\pi^\circ$ decays is also covered, followed by a discussion of the Ξ° Monte Carlo. Chapter 4 describes the $\Lambda\gamma$ event reconstruction, background reduction and extraction of the $\Xi^\circ \rightarrow \Lambda\gamma$ signal. The branching ratio calculation and conclusion are contained in Chapter 5.

Chapter 2

Apparatus

2.0 Introduction

The spectrometer used in this experiment was set up for detecting Λ's in coincidence with high energy gammas. A Ξ° produced by protons decayed in the laboratory to Λ and π°. These particles subsequently decayed $\Lambda \rightarrow p\pi^-$ and $\pi^\circ \rightarrow \gamma\gamma$. The basic componets of the spectrometer are a sweeping magnet and collimator to establish the neutral beam, a vacuum for the neutral hyperon decay region, multiwire proportional chambers for detection of the charged decay products, an analysis magnet for their momentum measurement, and a lead glass calorimeter for photon detection. This section will describe the componets of the spectrometer and how they are used.

2.10 Beam and Channel

Hyperons were produced by 400 Gev protons striking a 1.0 mm square, 1/4 interaction length (4.6 cm) lead target called the production target. The intensity of the proton beam varied between 10^{10} to 10^{11} protons per 1 second spill; a spill occured every 20 seconds. The primary proton beam was transported by a series of dipoles and focused by five quadrupole magnets as shown in Fig. 2.01. The beam was focused at the production target and was approximately the size of the target. The size and position of the proton beam at the target was monitored by a segmented wire ion chamber (SWIC) with

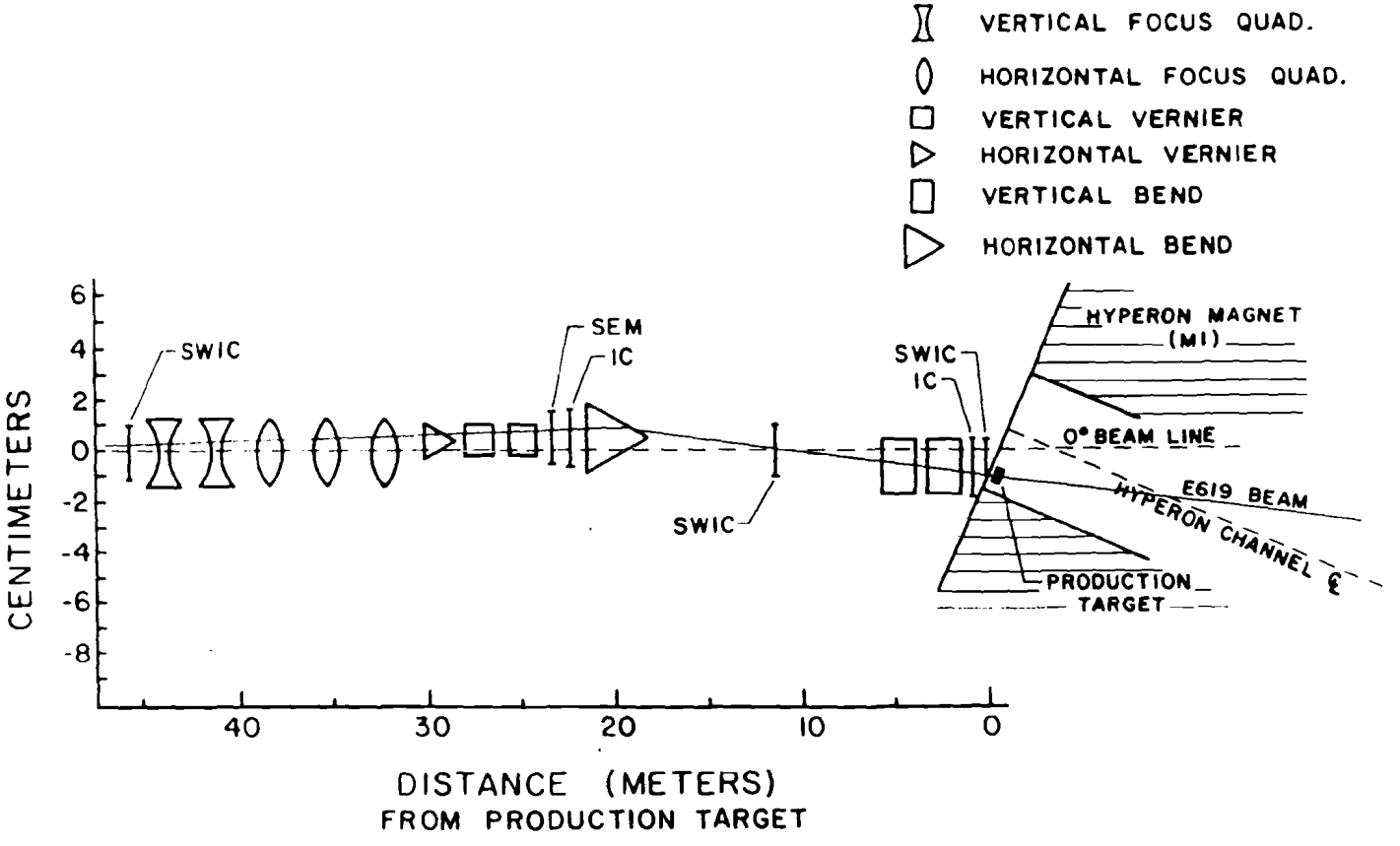

Fig. 2.01 : Plan view of the beam transport system in the pre-target area.

Note that the x scale has been expanded.[15]

0.5 mm wire spacing. The target was placed 30 cm inside a 7.33 m long dipole magnet, M1. The 35 kgauss vertical field of magnet M1 swept charged particles to the sides, leaving the neutrals. The neutral particles were collimated by a channel placed inside the length of the magnet shown in Fig. 2.02 b,c. The neutral beam production angle was defined by the angle between the incident proton beam and the collimator direction into the spectrometer. The production angle was in the vertical plane and controlled by four vertical bending magnets.

The composition of the neutral beam and the momentum spectra of the componets depended upon the production angle. The neutral beam emerging from the collimator consisted of γ, n, K°, Λ, and Ξ°. The flux of the neutral beam was roughly measured by a beam monitor at the very rear of the spectrometer. The monitor consisted of a scintillation counter, 0.5 radiation lengths of lead, a second counter, 4" of iron, a third counter, and finally a lead glass block. Logical combinations of the signals from the counters and glass block were made to estimate beam rates. Some charged particle background was also present, consisting primarily of muons from pion decay, but also containing e^+e^- pairs from gamma conversion, and products of neutron interactions. If the charged pions produced in the target can be dumped into the steel around the collimating channel before they decay to produce muons, most of the muons will not enter the apparatus. This was achieved by bringing the proton beam in at a finite production angle. The number of Λ's produced per proton on target decreases with increasing production angle, so there was a trade off between background reduction and neutral beam composition. By taking data at several angles, the optimum production angle was estimated to be ± 3.2 mrad. After the experiment, comparison of the Λ momentum spectrum to measured cross sections[17] put the production angle at +3.1 and -2.8 mrad.

The collimating channel was constructed primarily of brass blocks drilled with circular holes. The defining aperture of the collimator was a tungsten block 76.0 cm long with a hole 0.20 cm in diameter. The downstream end of the defining aperture was 5.03 m from the production target. The small size of the target and collimator aperture were directly related to the resolution of reconstructed Ξ°.

Early in the experiment a γ filter was installed to reduce the number of γ that might convert in

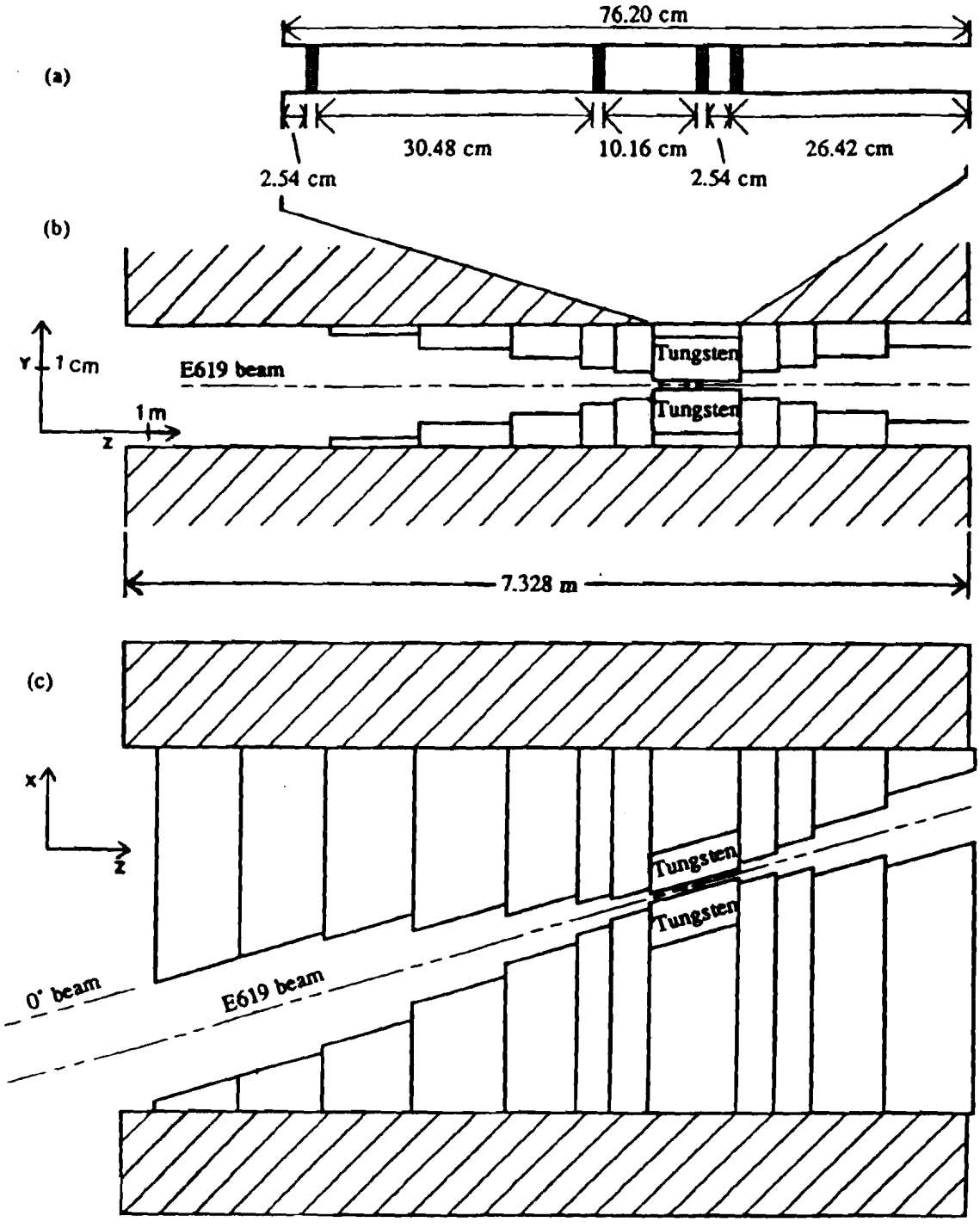

Fig. 2.02 : Elevation (b) and plan (c) views of the collimator which was embedded in the sweeper magnet, M1; (a) is an expanded view of the defining aperture of the collimator showing the location of the uranium foils used as a gamma filter.

material and cause high charged particle rates seen by the chambers. The γ filter consisted of four uranium plugs 0.95 cm long inserted at varying intervals, Fig. 2.02 a, inside the defining aperture. The uranium caused gammas to convert to pairs, which were then swept out of the beam by M1. There were 14 radiation lengths of uranium, corresponding to 0.67 interaction lengths. The beam monitor indicated a reduction in the γ flux by a factor of 5, and the ratio Λ/γ in the neutral beam increased by a factor of 2.

2.20 Spectrometer

The layout of the spectrometer is shown in Fig. 2.03. Neutral particles pass veto scintillation counters S1 and S2, and decay into charged particles in the decay volume. The decay volume consisted of a 10 m evacuated pipe, 3.5 m upstream of chamber C1, and 6.5 m downstream. The narrow upstream section of the pipe was 4" in diameter, and the downstream section was 18" in diameter. The windows of the vacuum pipe were 10 mil (0.025 cm) thick aluminum, except for the downstream window which was made of 20 mil (0.051 cm) thick stainless steel. The charged particles were detected by multiwire proportional chambers (MWPC's); the gammas by a lead glass calorimeter. The spectrometer coordinate system was right handed. The z axis was along the neutral beamline, with +x to the left facing downstream, and +y up. This was the coordinate system used throughout the experiment.

The MWPC's were of conventional design and have been described in detail previously[18]. Seven in all were used, four upstream of the analysis magnets, three downstream. Each chamber had two orthogonal signal planes, oriented in x and y, and three vertical high voltage planes. The exception was u,v chamber C3 which was rotated 45° relative to the others. Chamber C4 had one u plane in addition to x and y planes. The signal wire spacings were 1mm in C1, $2\sqrt{2}$ mm for the u plane in C4, and 2 mm for all others. The chambers were operated using a gas mixture of argon and argon-freon bubbled through methylal at 0°C, giving a final mixture, by volume, of 94.51% argon, 5.46% methylal, and .03% freon. The operating high voltage was between 2.8 and 3.2 kilovolts.

Each of the analyzing magnets M2 and M3 was 2.5 m long. Their defining apertures were 61x25

cm^2 and 61x30 cm^2. The average field values were 15 and 12 kgauss respectively, and together gave an average transverse momentum transfer to charged particles of 1.57 GeV/c. A small magnet, MV, with a horizontal field, was used only during the lead glass calibration to separate e^+e^- pairs.

Between all the chambers (except C1 and C2) and inside the analysis magnets were helium filled polyethylene bags to reduce multiple scattering of the charged particles. The windows of the bags were 5 mil (0.013 cm) thick.

Just downstream of the last chamber was the lead glass array. The array was stacked in two sections, a main array (MA) of 66 blocks stacked horizontally in six rows, and a front wall (FW) of 24 blocks hung vertically in two rows, shown in Fig 2.04. Each block was 10x10x38.4 cm^3 type F2 lead glass with radiation length 3.2 cm, manufactured by Ohara and by Schott. There were 15 radiation lengths of glass for gammas to pass through; 3 in the vertically placed FW blocks, and 12 radiation lengths in the MA. The blocks were viewed along their length with RCA 6342A/V1 phototubes, which were 5 cm in diameter. The phototubes were mounted in a threaded collar, and each screwed into a hole cut in a lucite block epoxied to the lead glass. This system provided uniform pressure to the optical grease coupling between phototube and glass. Each lucite block also contained a small hole for a light fiber. The fibers delivered light from 6 neon flash lamps used to monitor the array for tube or cable failures, or drifts in the phototube response.

Each row in the MA was offset 1/2 block from the adjacent rows to give the minimum number of nearest neighbors (6). The entire array shadowed the exit aperture of the analysis magnets. The center block in the array was removed to allow the neutral beam to pass through without interfering with γ detection. Three more blocks to the -x side of center were removed so the protons from Λ decay could also pass, making a 10x40 cm^2 hole in the MA and FW. The MA and FW were separated by 10 cm.

Counter S7 shadowed nearly the whole face the lead glass. This large counter had BBQ waveshifter bars on the horizontal edges to transmit light to two phototubes on the -x side. Counter S7 was used to veto events with charged particles which would enter the glass array. The side of the counter opposite the phototubes was found to be inefficient, so S7a was installed on the +x side in front of S7.

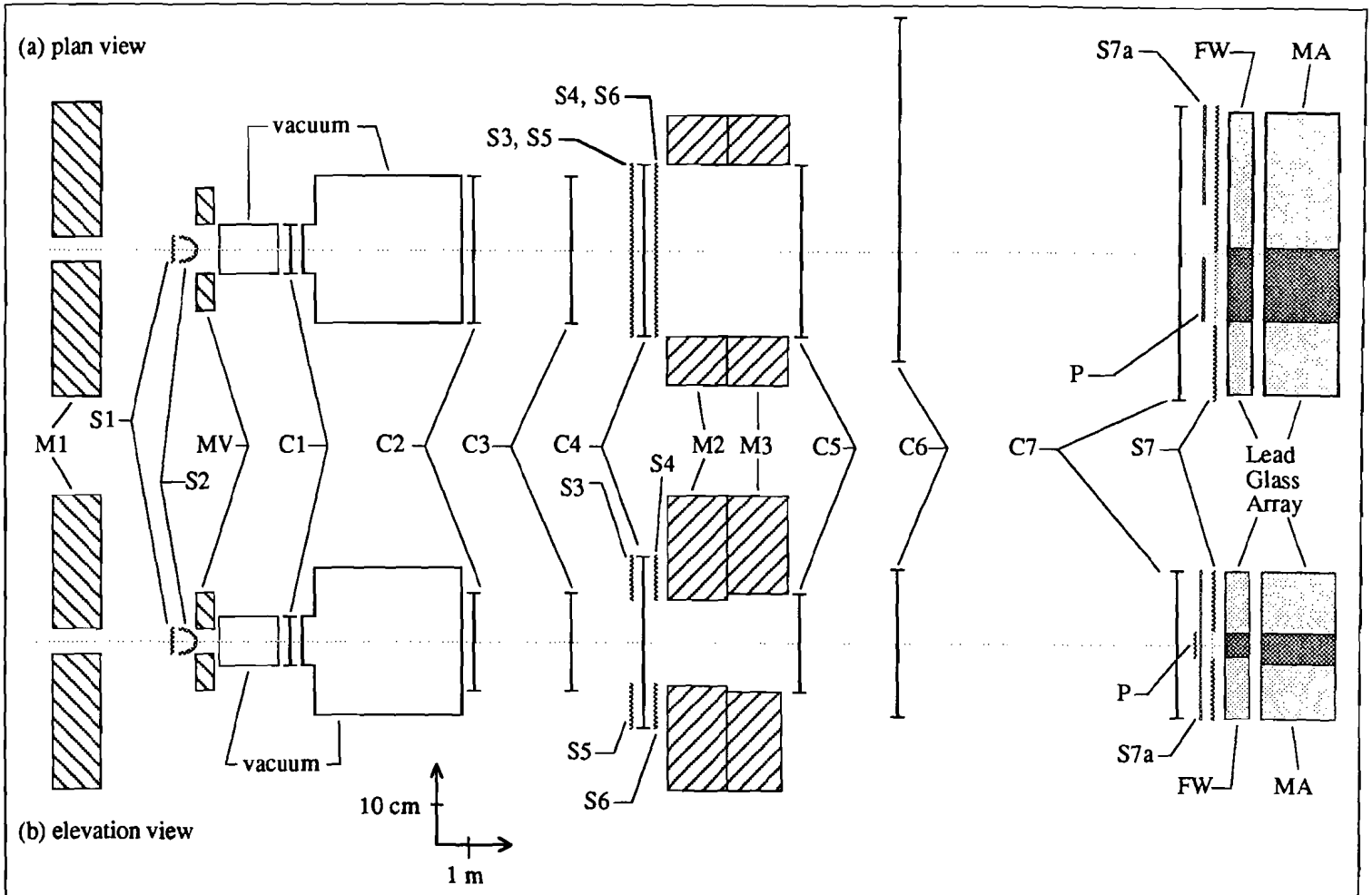

Fig. 2.03 : Plan (a) and elevation (b) views of the E619 spectrometer. C's are multi-wire proportional chambers, S's and P are scintillation counters, M's are dipole magnets.

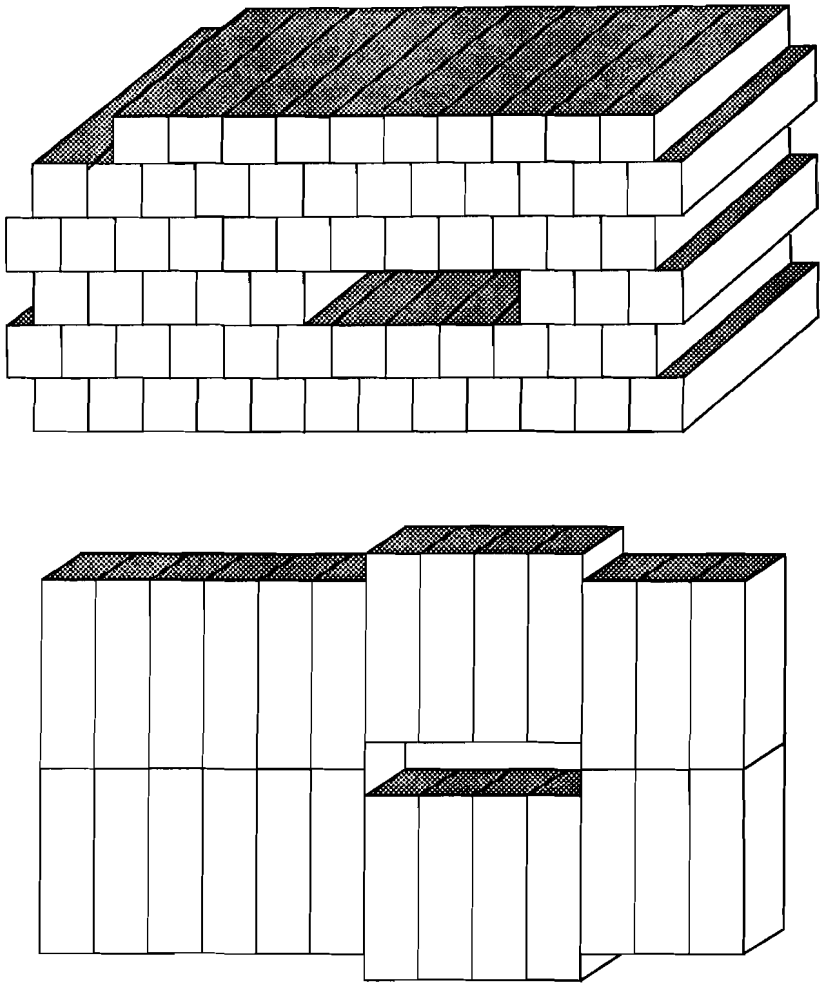

Fig. 2.04 : Diagram of the lead glass array. The upper drawing shows the main array, which lay 10 cm behind the front wall, lower drawing. Each part held a four block wide hole to allow passage of the neutral beam.

Just 1 cm downstream of S7 was a sheet of lead covering the area of the counter and 1.7 radiation lengths (3/8") thick. The lead added to the total radiation lengths of material for gamma detection. Counter S7 and the lead sheet both had 40x10 cm^2 holes matching the one in the glass array.

Counter P, in front of S7, was 10.2 x 32.7 cm^2, nearly covering the area of the hole in the lead glass, and aligned with the -x side of the hole. The counter did not cover the area occupied by the neutral beam. It was used to detect high momentum positive particles and insure that they passed through the hole in the lead glass array. The counter also determined the timing for the experiment. Since it was a small counter, timing jitter was estimated to be less than 1 nsec in the trigger, ADC gates, TDC gates, and latch gates.

In $\Xi^\circ \rightarrow \Lambda\pi^\circ$ decays, if only one γ from the π° hit the glass array, most often the other γ did not clear the magnet aperture. Gammas which hit above and below the magnet aperture were detected by a scintillator-lead-chamber-scintillator sandwich on the upstream face of M2. Chamber C4 extended 22.6 cm above and below the magnet aperture. Upstream and downstream of the extended areas were 66x22 cm^2 scintillators, 3/8" thick, with 1.5 radiation lengths of lead between. A γ which converted in the lead was detected by both the chamber and the second scintillator in the sandwich. The counters were S3 and S4 above the magnet aperture, S5 and S6 below.

Two other scintillators were used as part of the trigger. S1 and S2 were veto counters used to insure that neutral particles entered and exited a Primakoff target, used to measure the Σ° transition moment. S1 was a 1/8" thick flat scintillator; S2 was a capped tube of scintillator which fitted around the primakoff target and target holder. The entire primakoff target apparatus, used for the Σ° part of the experiment, is shown in Fig. 2.05. The Primakoff target will be discussed in section 3.40, in terms of its effects on Ξ° acceptances. Table 2.2 lists the properties of the Primakoff targets.

2.30 Trigger

The topology of a $\Lambda \rightarrow p\pi^-$ decay in the apparatus appears as a 'V'. The two charged decay products point back to a vertex where the Λ decayed. The charged particles are of opposite sign and are

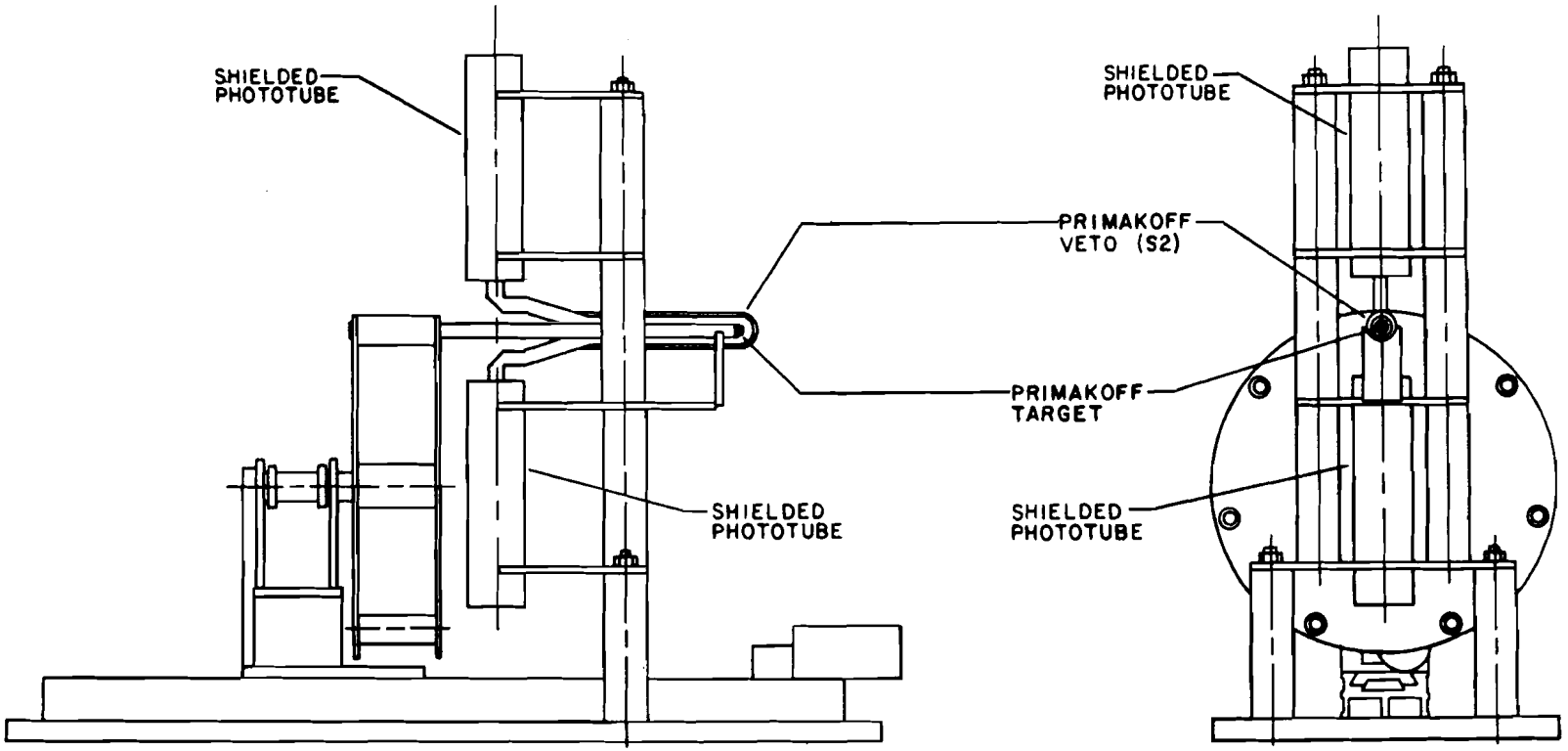

Fig. 2.05 : Design of the Primakoff target manipulator. Each target was held in an aluminum tube. All the tubes were held by a drum. To change targets, the drum was moved away from the phototube stand, freeing the target and its holder from the scintillator sleeve, rotated to the next target position, and then moved forward to engage the new target.[15]

bent with opposite angles in the analysis magnets. The topology downstream of the magnets is asymmetric about the z axis. Because the proton is more massive than the pion, it has most of the momentum of the parent Λ and is therefore deflected less by the analysis magnets. Detection of Λ decays takes advantage of the asymmetry of the decay products to discriminate against contamination from K° decays. The decay $K^\circ \rightarrow \pi^+\pi^-$ also has the 'V' topology, but since the π^+ and π^- have the same mass, the topology after the magnets is typically symmetric. In the spectrometer, counter P was positioned to detect the high momentum proton from a Λ decay, and chamber C6 was shifted 24 cm left (+x) of center to catch the lower momentum π^-.

The chamber and counter signals were arranged to make a logical decision, the trigger. The Λ trigger required no signal from S1 and S2 and charged particles in C2, indicating a neutral particle entered the decay region but charged particles exited the region. A signal from counter P insured one charged particle was a high momentum (>80 GeV) positive particle. To insure the event would also contain a negative particle, chamber C6 was divided electronically to give a promt signal from the side left of center only. Each chamber produced a fast pulse initiated by any charged particle which traversed it. The C2 signal was an OR of all horizontal and vertical wires. The C6 signal was an OR of the appropriate vertical wires only. The logical statement for the Λ trigger is written $\Lambda = \overline{S1}\cdot\overline{S2}\cdot C2\cdot C6L\cdot P$. A more exclusive Λ trigger, called Λ', required that no charged particles entered the lead glass by using counters S7 and S7a in veto, written $\Lambda' = \Lambda\cdot(\overline{S7+S7a})$.

The good event trigger, GE, required, in addition, the existence of lead glass information. The lead glass part of the trigger required a minimum energy , or pulse height, from the phototubes. The signal from each phototube was split three ways: one went to LeCroy 2280 analog to digital converters (ADC's), a second signal to LeCroy ECLine 4416 discriminators and then to LeCroy 2770A time to digital converters (TDC's), and the third signal to the glass trigger. All glass trigger signals were sent to LeCroy LRS127 linear adders. The signals from the FW and MA were summed separately. The two resulting signals were sent to a discrimator whose threshold was set for a minimum energy in both the FW and the MA. The threshold corresponded approximately to an energy of 2.5 GeV in the MA, and

0.4 GeV in the FW. The final GE trigger was GE=Λ'·FW·MA .

Requiring a level of energy deposition in the FW separate from the MA helped the glass trigger reject hadron events that would not be of interest. Lead glass has an interaction length about 10 times longer than the radiation length. It was unlikely for a hadron to deposit enough energy in the FW to pass the trigger. The glass trigger thus helped discriminate against hadron showers, mostly protons scraping along the glass blocks at the boundry of the hole in the glass. The lead sheet and FW in front of the MA provided better containment of the γ shower. A typical photon (20 GeV) deposited about 25% of its energy in the FW.

The final trigger consisted of a mixture of GE, Λ' and Λ triggers. All GE triggers were accepted and written to magnetic tape. Λ and Λ' triggers were electronically divided (pre-scaled) by a factor of 2^9 for most data tapes, and 2^{10} for the last 1/4 of the data.

2.40 Data Acquisition

A schematic of the trigger electronics is shown in Fig. 2.06. If the event satisfied the trigger, several simultaneous signals were then generated. One signal, the chamber enable,with a width of about 150 nsec, was returned to each chamber in coincidence with the delayed wire hit signals, causing the wire information to be latched for read-out. Another signal gate, with a 100 nsec width, initiated ADC encoding; likewise a 'common stop' was sent to the TDC units for the lead glass to start their encoding. A 'busy' signal sent to the electronic gating system prevented more events from being accepted until all event related information had been read out. A priority interupt sent to the computer initiated the read-out process in the CAMAC crates. For each event the data read-out contained:

1) latches for all scintillators and trigger logic configurations

2)MWPC wire hits read serially through an MWPC-CAMAC interface

3)ADC information for all lead glass signals

4)TDC information, consisting of a block number and timing counts for each glass block with a signal above the ECLine 4416 discriminator threshold.

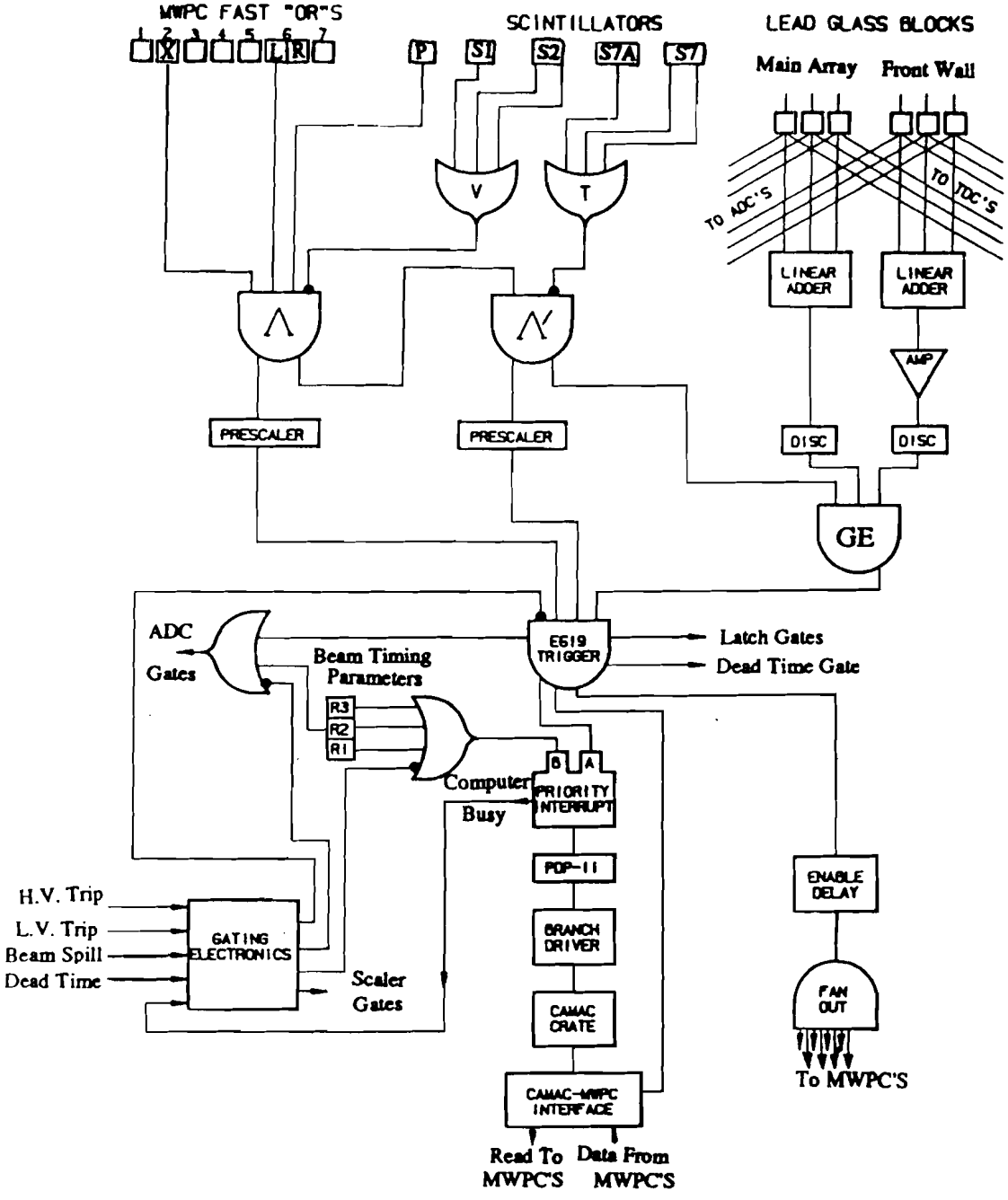

Fig. 2.06 : Schematic of the trigger electronics. (15)

The information was transferred to the PDP 11-45 computer via a CAMAC-PDP interface. Each event was transferred first to a memory buffer and then to 6250 b.p.i. magnetic tape. The computer then cleared all units and the logic was reactivated to accept another event. The on-line computer program was a Fermilab system standard, RT-MULTI[19]. About 200 events per one second proton spill were written to magnetic tape, up to 80% of them GE triggers. The other events were a mixture of Λ and Λ' triggers.

A second priority interupt, generated by timing signals from accelerator control, initiated a data read-out between spills. The data consisted of glass ADC's and scalers. The flash lamps on the glass blocks were fired and the ADC counts recorded; then the pedestal levels in the ADC's were read out. Both were monitors of the consistency of lead glass behavior. The scalers recorded the rates per spill seen by each trigger type, the rates in each counter in the apparatus, the singles rates in C2, and beam monitor rates.

The MWPC's were monitored continuously during the run of the experiment. Each chamber had a 1-μCu Fe55 source pointed at one signal wire outside the fiducial area. The signals from these wires went through an emitter-follower and were observed on an oscilloscope in the counting room. When the chamber was running with optimum efficiency, the 5.9 keV x-rays from the source gave a wire signal of about 5mV pulse height. The pulses were checked at least every 8 hours, and the high-voltage on each chamber adjusted accordingly.

The on-line computer program used for data read-out and transfer to magnetic tape also provided histograming capabilities. Every channel in the experiment, all chamber wires, ADC's and TDC's, could be displayed as the data was being taken. The histograms were an important on-line diagnostic for malfunctioning equipment.

2.50 Data Taking Conditions

The Σ° part of the experiment depended on material in the neutral beam, Primakoff targets, for production of Σ°'s. There were 7 targets in all, including one empty, air target. Data taking was

Table 2.1

Data Tape Summary

Data taking conditions and the number of data tapes taken for each

	Production Angle (mrad)				
	M1 Current (amps)				
Primakoff	-3.2	+3.2	-3.2	+3.2	
Target #	-3300	-3300	+3300	+3300	Totals
1	3	0	0	3	6
2	1	0	2	2	5
3	2	1	0	3	6
4	5	1	3	8	17
5	8	3	7	13	31
6	2	1	2	3	8
7	8	5	5	13	31
Totals	29	11	19	45	104

Table 2.2

Properties of the Primakoff Targets

Target Number	Material (Z)	Length L (cm)	$L / L_{absorption}$	$L / L_{radiation}$
1	Air (7)	-------	-------	--------
2	Be (4)	1.1197	0.0305	0.0317
3	Be (4)	5.3303	0.1452	0.1510
4	Sn (50)	0.6942	0.0303	0.5737
5	Sn (50)	1.2082	0.0528	0.9985
6	Pb (82)	0.0821	0.0044	0.1467
7	Pb (82)	0.5609	0.0304	1.0016

emphasized on the higher radiation-length targets since they would produce the most Σ°'s. Approximately equal amounts of data were taken at the ±3.2 mrad production angle. About halfway through the data taking period the current in the sweeper magnet M1 was reversed, and the proceedure repeated. Table 2.1 shows the relative proportions of data under these conditions. In all, 104 Σ° trigger data tapes were taken and used for the Ξ° analysis.

Other types of data tapes were written which determined alignment and calibration of the apparatus. These consisted of two 'straight through' tapes, for definition of the spectrometer coordinate system; and several lead glass calibration tapes were taken.

2.51 Chamber Alignment

The spectrometer coordinate system was defined by a 'straight through' beam of protons. A low intensity (~10^6) proton beam was sent straight through the collimator channel. All magnets were turned off, and all targets removed. Scintillators placed at the upstream and downstream ends of the spectrometer acted to form a trigger for a proton passing through all chambers. The +z axis was defined as this undeflected proton beam. The x=y=0 origin in each chamber was defined as the centroid of wire hits from the proton beam, and was determined to a precision of about 0.01 cm. Although the chambers were placed using optical survey techniques, they were not all precisely perpendicular to the beam. The small rotational corrections were found by minimizing the residuals of straight tracks from data taken with the analysis magnets off.

2.52 Lead Glass Calibration

Two sets of lead glass calibration data were recorded, one at the start of data taking, and the other about 1/3 of the way through. In addition there were several preliminary calibration runs. An e^+e^- beam was made by placing a lead foil converter between S1 and S2. A γ in the beam converted in the lead foil to an e^+e^- pair. Magnet MV, just downstream of the converter, separated the pair vertically. The analysis magnets M2 and M3, operated at reduced current, separated the pair horizontally. The magnet

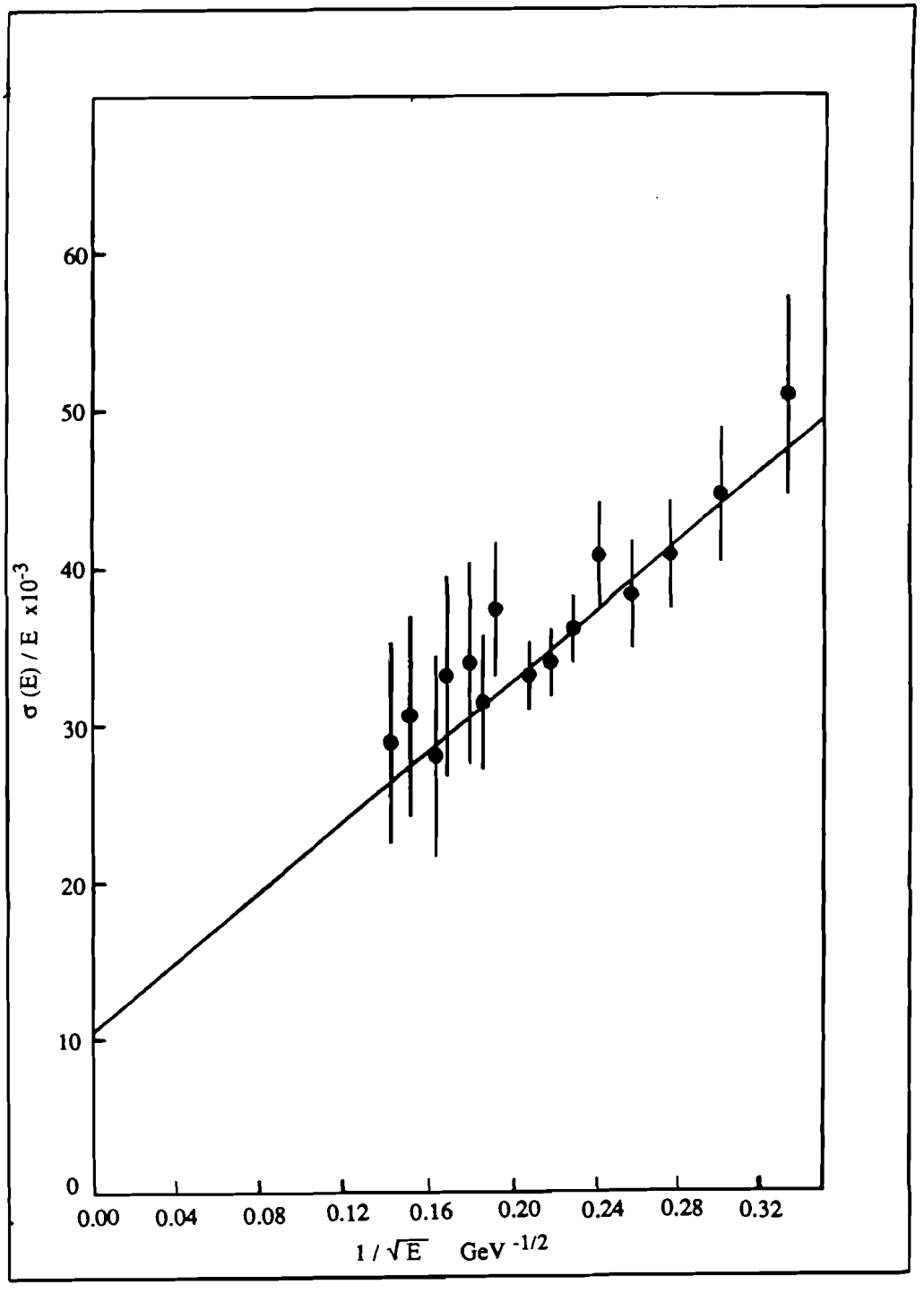

Fig. 2.07 : The lead glass energy calibration. The line is a least squares fit to the points. (15)

currents were set so that electrons (positrons) of energy similar to the desired photons hit the glass. Since the lead glass array was stacked on a cart set on rails perpendicular to the beam, the combination of moving the lead glass and adjusting the field of MV allowed each block to be illuminated by e^+ or e^-. Pairs in the spectrometer appeared as a single track upstream of the analysis magnets, and as a 'V' downstream. The trigger for pairs was much like the Λ trigger, but using only S1 as a veto and S7+S7a in coincidence: $\overline{S1}\cdot S2\cdot C2\cdot C6L\cdot C6R\cdot(S7+S7a)$.

The preliminary calibration runs studied the best magnet current and glass position settings to use; they were also used to roughly equalize the gains for all blocks. Since the glass trigger used summed pulse height signals, it was important that the gain of each block and phototube be roughly equal.

The e^+e^- track data were analyzed to yield the momentum of both particles in the pair. A correspondence was made between pulse heights in the glass ADC's and the energy of the particles entering them. The calibration constants for the lead glass blocks are values in GeV/count which convert ADC counts to an amount of energy deposited in the block. A simple block clustering algorithm was used to define the electromagnetic shower from the e^+ or e^-. The MA lead glass block with the largest energy was defined as the center of the shower. Any of the six surrounding MA nearest neighbors, and up to six FW nearest neighbors which had energy deposited in them were included as part of the shower.

The e^+e^- track data were analyzed using the same track fitting program as for the Λ reconstruction, and is discussed in Sec. 3.10. The momentum of each track was given by the bend in the analysis magnets, and each track was projected to the glass array. The shower from the e^+ or e^- was the cluster found around the location of the projected track. The shower energy in the cluster was set equal to the energy of the measured track, E_j. The pulse height counts s_{ij} for each ith block in cluster j was known. The calibration constants c_i were calculated from minimizing the quantity

$$\sum_j [\, E_j - \sum_i c_i \cdot s_{ij} \,]^2 \qquad \text{(Eq. 2.1)}$$

The resolution in energy was obtained from the half width of the distribution ($E_{glass} - E_{track}$) and was found to fit

$$\frac{\sigma(E)}{E} = \frac{0.111}{\sqrt{E}} + .01 \qquad \text{(Eq. 2.2)}$$

A plot of the function and data points is shown in Fig. 2.07.

A tape to tape monitor of the lead glass calibration was done by using gammas from π° decays. The π° came from $\Xi^\circ \rightarrow \Lambda\pi^\circ$ events which were present on every data tape. Any change in the glass calibration resulted in a change in the reconstructed π° mass. The method of using π° for calibration is discussed in section 3.31 as part of the Ξ° reconstruction.

Chapter 3

Analysis I

3.0 Introduction

The events of interest to this analysis were $\Xi^\circ \to \Lambda\pi^\circ$ and $\Xi^\circ \to \Lambda\gamma$ decays. To calculate the branching ratio, $\Xi^\circ \to \Lambda\gamma / \Xi^\circ \to \Lambda\pi^\circ$, one needs the number of both decay types detected, and their acceptance in the apparatus and analysis. The determination of the number of each decay type present is the point of the analysis. The apparatus and analysis acceptances for each type were found by generating simulated (Monte Carlo) Ξ° decays, and processing them through the event reconstruction and selection proceedure used for the data. This chapter will discuss the reconstruction and selection of $\Xi^\circ \to \Lambda\pi^\circ$ decays, and the methods used to generate Monte Carlo $\Xi^\circ \to \Lambda\pi^\circ$ decays. Chapter 4 will discuss the $\Xi^\circ \to \Lambda\gamma$ event reconstruction and selection.

Identification of Ξ° decays required several stages of analysis, the major parts being:

1. charged track reconstruction and identification of $\Lambda \to p\pi^-$ decays
2. lead glass shower cluster analysis to obtain gamma energies and positions
3. kinematic reconstruction of Ξ° decays.

Identified Λ decays were placed into two classes, those which passed the G.E. trigger, and those which were Λ or Λ' triggers only. The Λ or Λ' trigger events were for the most part Λ's produced at the production target by protons, called beam Λ's. Identified Λ decays which were G.E. triggers were divided

into two classes by the lead glass analysis, a Λ with a single γ shower, and a Λ with 2 or 3 γ showers. All events with a Λ and 2 or 3 γ showers were sent to the $\Xi^\circ \rightarrow \Lambda\pi^\circ$ reconstruction. A constraint on the reconstructed Ξ°'s required that they be within the area of the neutral beam cone, which was determined by using the beam Λ's. The neutral beam had a diameter of 0.2 cm at the exit of the collimator and an angular divergence of 0.2 mrad. full width half maximum. Identified $\Xi^\circ \rightarrow \Lambda\pi^\circ$ decays were in turn used to recalibrate the lead glass. Section 3.1 will cover the reconstruction of Λ decays, section 3.2 will discuss the lead glass analysis. The kinematic reconstruction of Ξ° decays is contained in section 3.3, and section 3.4 will discuss the generation of Monte Carlo Ξ° decays.

3.10 Λ Reconstruction

About 100 data tapes were used with approximately 10^5 triggers per tape, giving 10^7 events to be analyzed for Λ decays. These events were any of the three trigger types, Λ, Λ', or GE, Sec. 2.30. The decay topology of $\Lambda \rightarrow p\pi^-$ requires two charged tracks which diverge from a common decay point, and are bent through opposite angles in the analysis magnets. A common decay point must be found for both the x and y views. To start, the MWPC wire hits were fit to straight lines by the least squares method. The y-plane chamber hits were fit first, because the charged particles were not bent in the y-z plane. If two and only two tracks were found, then the upstream x-z hits were fit to lines and correlated to the y plane tracks by using the u,v chamber C3. The x-z line segments from the chamber hits downstream of the analysis magnets were required to intersect the upstream segments at a given bend point approximately midway through the magnets. The momentum of the tracks was calculated based on the bend angle in the magnet. The decay vertex was calculated in both x and y planes and constrained to have the same z. The process resulted in slopes for the y view tracks and slopes for both upstream and downstream segments of the x view tracks, and a decay vertex (x,y,z). A χ^2_g was calculated for this geometrical fit and events selected with χ^2_g / d.f. < 3.0. About 40% of all triggers passed the geometric fit requirements.

The Λ reconstruction efficiency determined from the Monte Carlo was 78%. The low efficiency

was due to the fact that the aperture of C5 was not aligned with the aperture of C6, which was in the trigger. Consequently, a low momentum π^- could satisfy the trigger by hitting the left side of C6, and missing S7a (therefore also missing C7), yet pass through an inactive area of C5. These events failed the reconstruction because only a single point on the pion track was available downstream of the analysis magnets. Monte Carlo events were generated with C5 in the misaligned position. When the events missing C5 were eliminated from the sample, the track reconstruction for Λ decays was 98% efficient.

Three types of neutral decays have the topology which may pass the geometric requirements: $\Lambda \rightarrow p\pi^-$, $\Lambda \rightarrow p\pi^+$, $K^\circ \rightarrow \pi^+\pi^-$. Because the Λ trigger arrangement required a high momentum positive and the Λ' a low momentum negative, the latter two decay types were strongly suppressed. The invariant mass of the neutral parent was calculated from $M^2 = m^2_+ + m^2_- + 2E_+E_- - 2\mathbf{p}_+ \cdot \mathbf{p}_-$, using masses $(m_+,m_-) = (m_p,m_\pi)$, (m_π,m_p), or (m_π,m_π). If the invariant mass from the (m_p,m_π) hypothesis was within 6σ, or approximately 15 MeV, of the Λ mass, 1.1156 Gev, then the event was classified as a Λ. Approximately 4% of these events also came within 25 MeV of the K°_s mass, .4977 GeV, when reconstructed under (m_π,m_π) ; and they were classified as ambiguous Λ decays. The ambiguity occured when the ratio

$$\frac{p_-}{p_+} = \frac{(m^2_\Lambda - m^2_K)}{(m^2_p - m^2_\pi)} - 1 \qquad \text{(Eq. 3.1)}$$

Actual contamination of K°_s at this point was small,[17,18]; both classifications of Λ decays were included in the sample of identified Λ decays.

Approximately 92% of the events passing the track reconstruction geometric requirements were identified as Λ decays. The mass of Λ daughters from Ξ° decays is shown in Fig 3.01; it has a full width half maximum of 4 MeV. The χ^2_g for these Λ's is shown in Fig 3.02, and the χ^2/d.f. in Fig. 3.03. In all the figures of histograms, unless otherwise noted, the points with error bars are the data, and the line is the Monte Carlo $\Xi^\circ \rightarrow \Lambda\pi^\circ$ decays, shown for comparison. The beam Λ mass distribution is about 1 MeV wider than the distribution for daughter Λ's, because the beam Λ's had a higher average momentum.

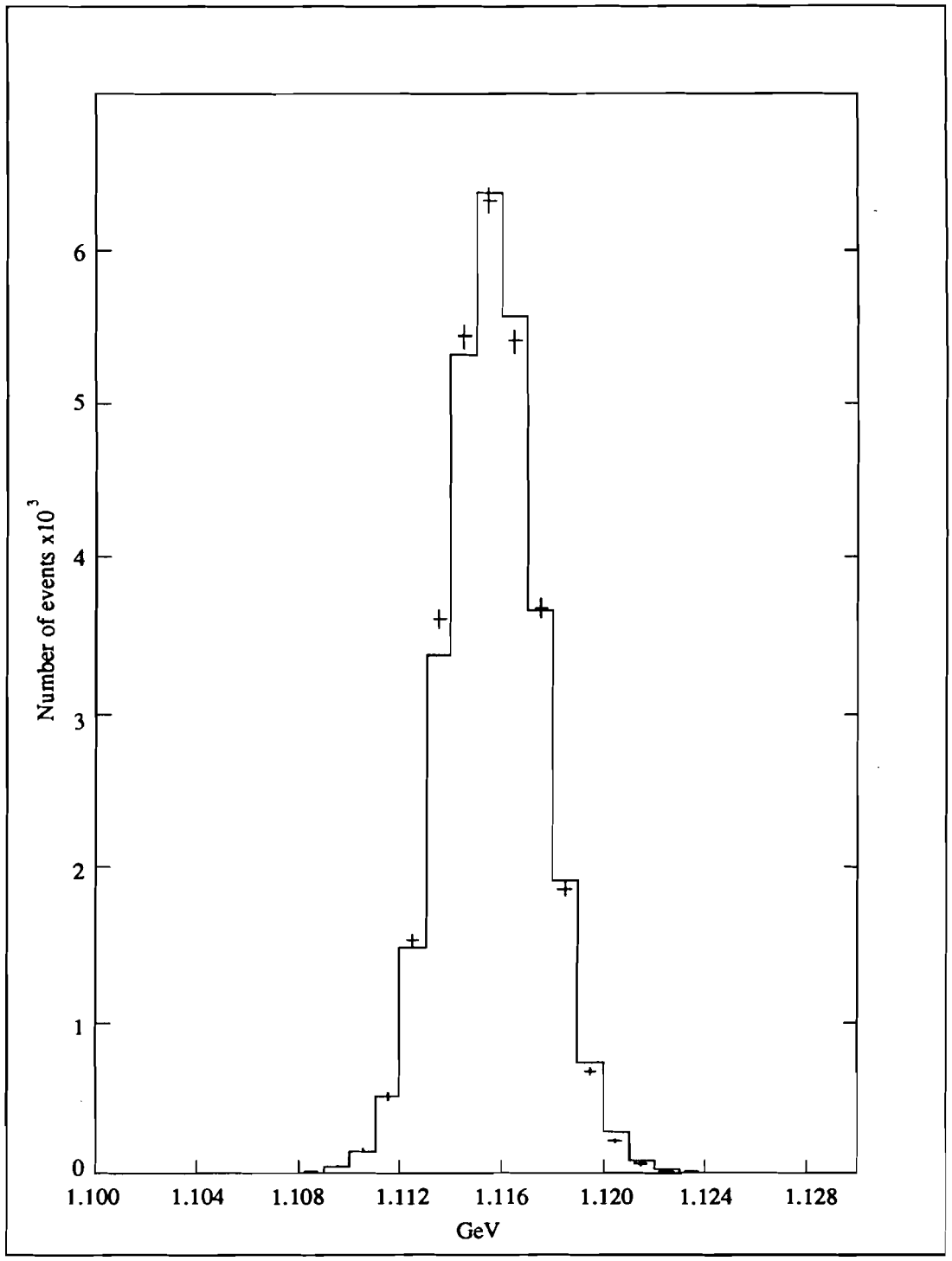

Fig. 3.01 : The mass distribution of daughter Λ's from $\Xi^\circ \rightarrow \Lambda\pi^\circ$ decays.

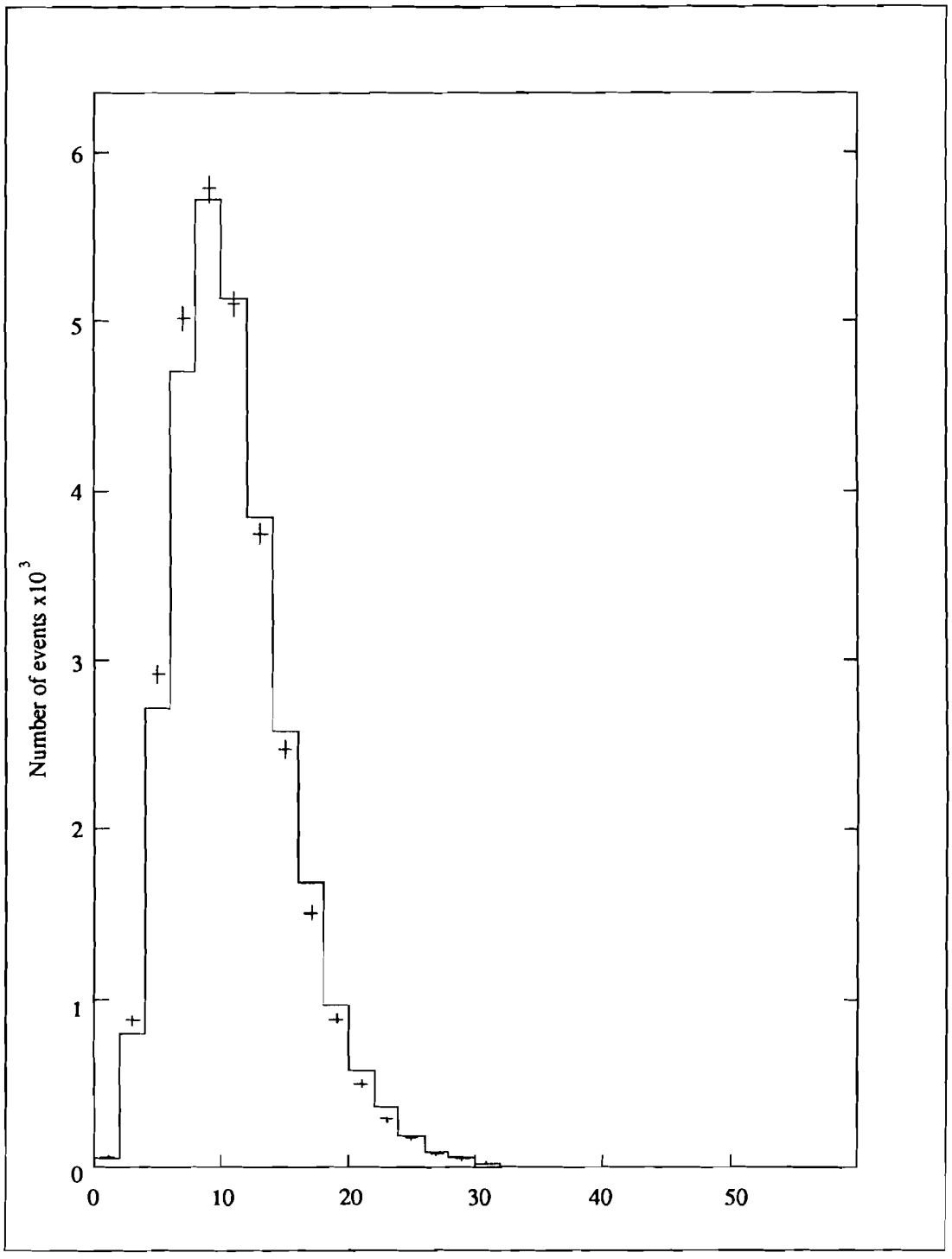

Fig. 3.02 : The chi-squared from the geometric straight track fit, χ^2_g.

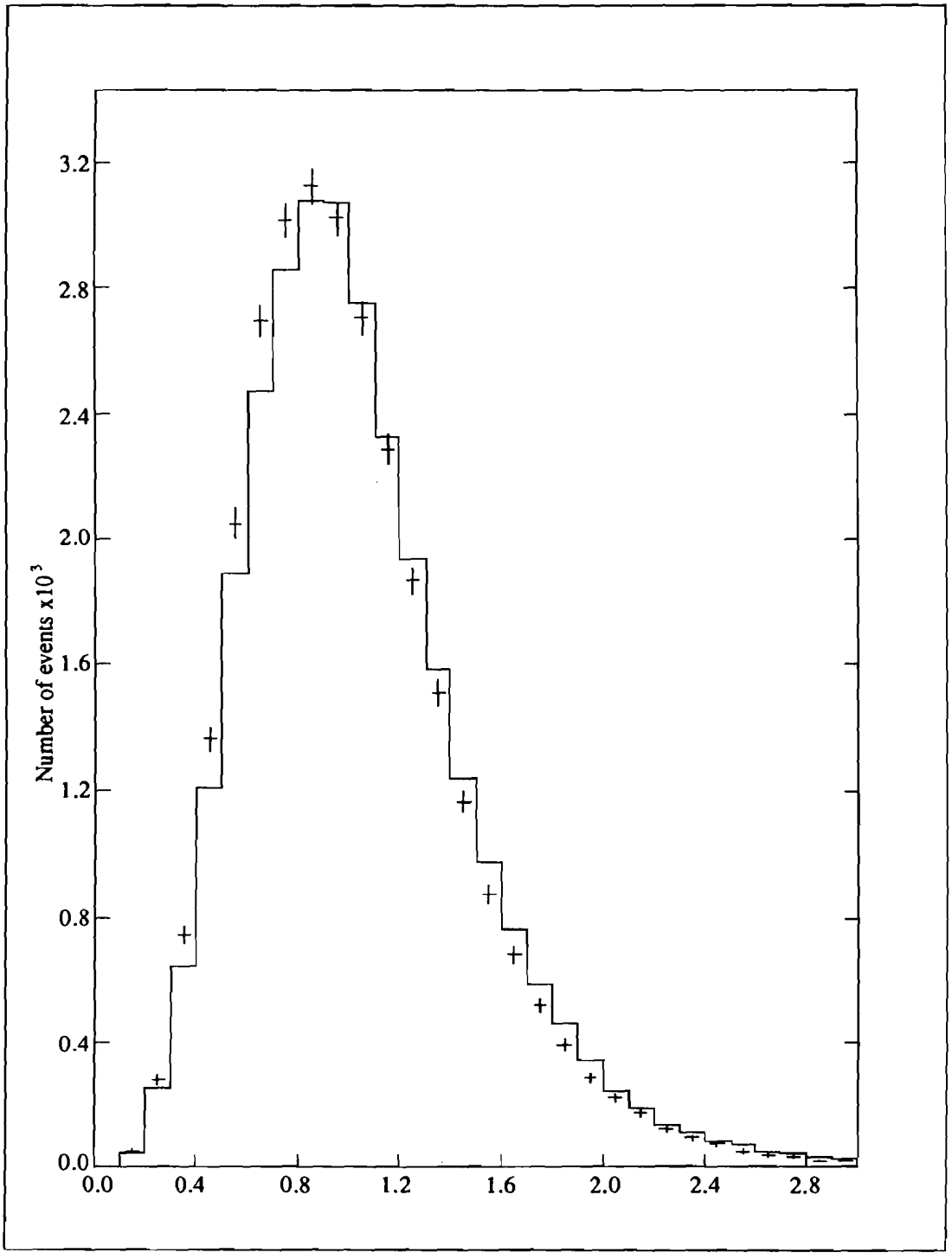

Fig. 3.03 : The tracking geometric chi-squared per degree of freedom, χ^2_g / d. f. The distribution is cut at a value of 3.0.

3.11 Magnetic Field Corrections

In the track reconstruction, the curved path followed by a charged particle through the magnets is approximated by a single bend plane where the track kinks. For a single homogeneous dipole, the position of the bend plane can be calculated exactly. In reality, there were two dipoles with a very small gap between them. The position of the bend plane was modified by second order corrections based upon the particle's entering angle and momentum.

The analysis magnets were mapped using a Fermilab device called Ziptrack. It consisted of 3 orthogonal coils which traveled along a rail positioned anywhere in the magnet aperture. Despite optical surveying when the magnets were installed, the Ziptrack field mapping found that the second magnet was slightly lower, and rotated by 7.5 mrad, with respect to the first. The fringe fields, B_z vs. y, were mapped at each aperture. The fringe fields were expected to be zero at the midplane, but since the two magnets were not aligned this was not true. The $\int B_z \cdot dl$ of the fringe field was about 1% of the $\int B_y \cdot dl$ of the analysis bending field. Fig. 3.04 shows the B_y and B_z fields from the Ziptrack mapping. The data were not corrected for any of these effects, but the fringe fields and magnet misalignment in y were included in the Monte Carlo simulation.

The currents in the analysis magnets varied by about 4% over the course of the experiment. On a single data tape, taken over a time period of about 2 hours, the current values were typically constant to within a percent. Events identified as Λ decays based on the expected magnet transverse momentum transfer of 1.560 GeV/c were adjusted on a tape to tape basis to give the correct average Λ mass. The events were refit using the new momentum transfer values.

3.12 Λ Kinematic Fit

To be certain the Λ momentum vector was measured as accurately as possible, identified Λ decays were sent through a kinematic fitting proceedure. The track slopes found by the geometric fit were allowed to vary within their measurement errors while the Λ mass was constrained to its known value. A χ^2_k was calculated for the fit. The decay vertex was then moved, within errors, and the fit repeated

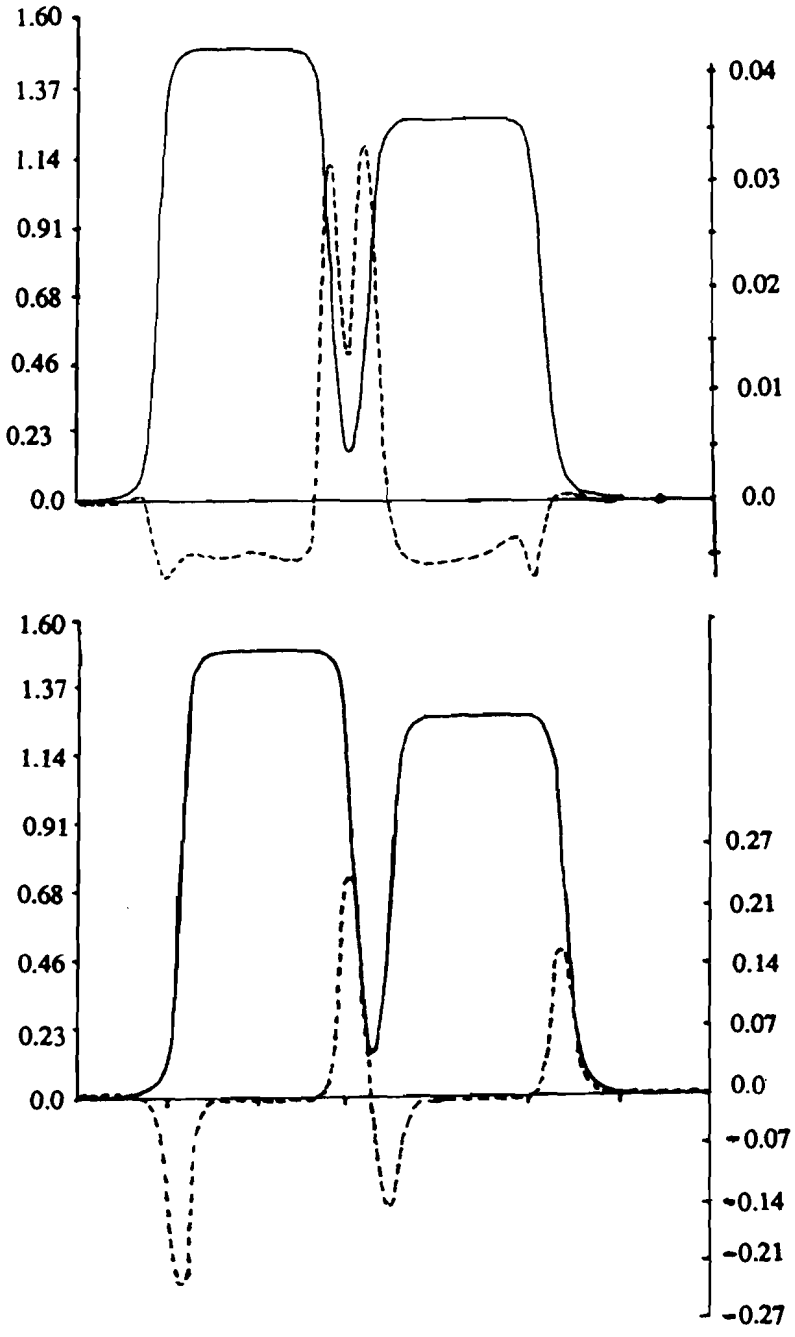

Fig. 3.04 : Mapping of the magnetic fields in the analysis magnets. The vertical scales are in Tesla; the left side for the solid lines, right side for the dashed lines. The horizontal scale represents a line parallel to the beamline through the aperture of the magnets. The solid lines are the By fields in M2, left, and M3, right; the upper plot dashed line is the midplane fringe field, Bz, and the lower plot dashed line is a fringe field 3.2 cm vertically off the midplane.

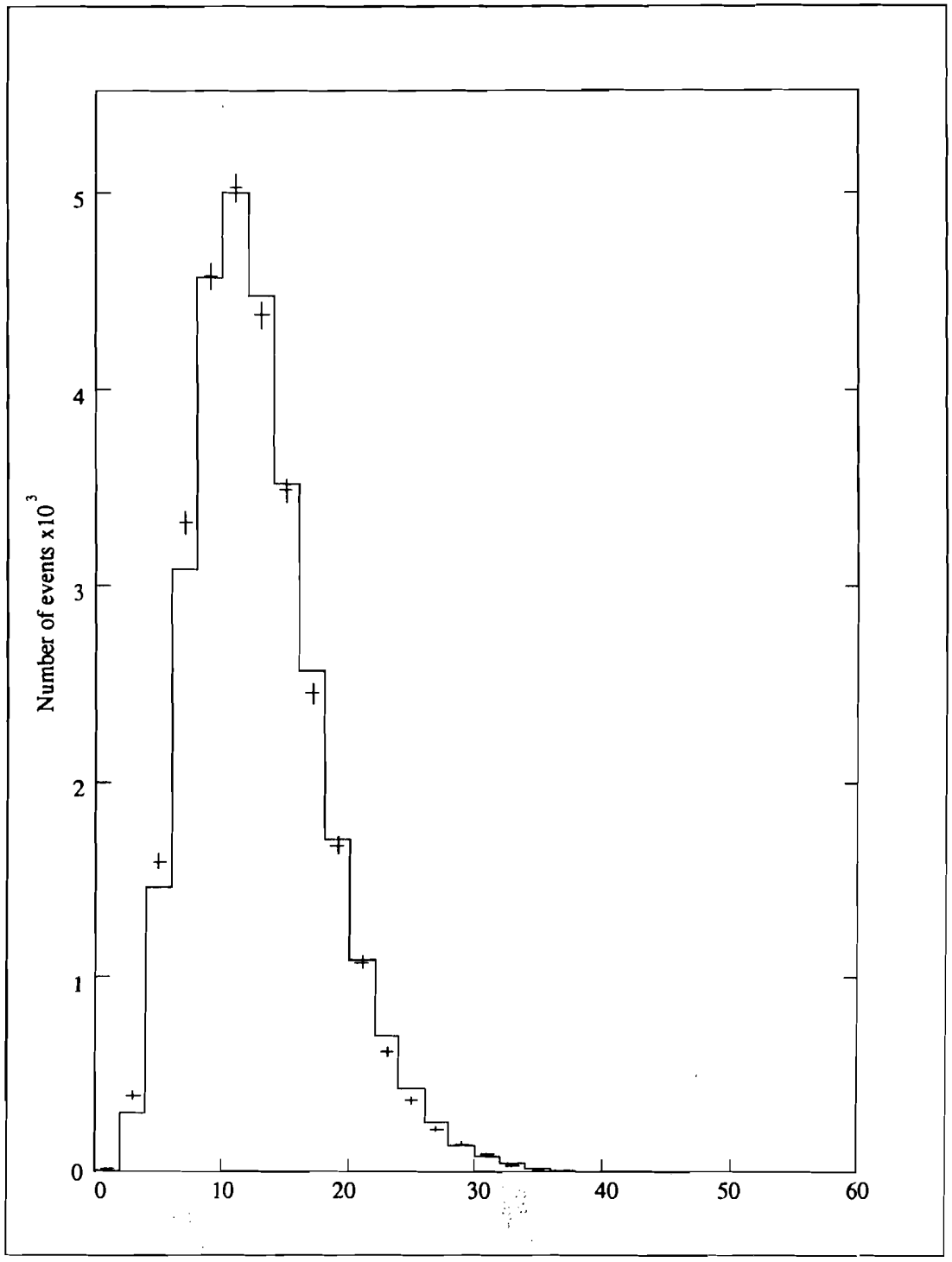

Fig. 3.05 : The chi-squared from the Λ kinematic fit, χ^2_k. The mass of the Λ has been added as a constraint.

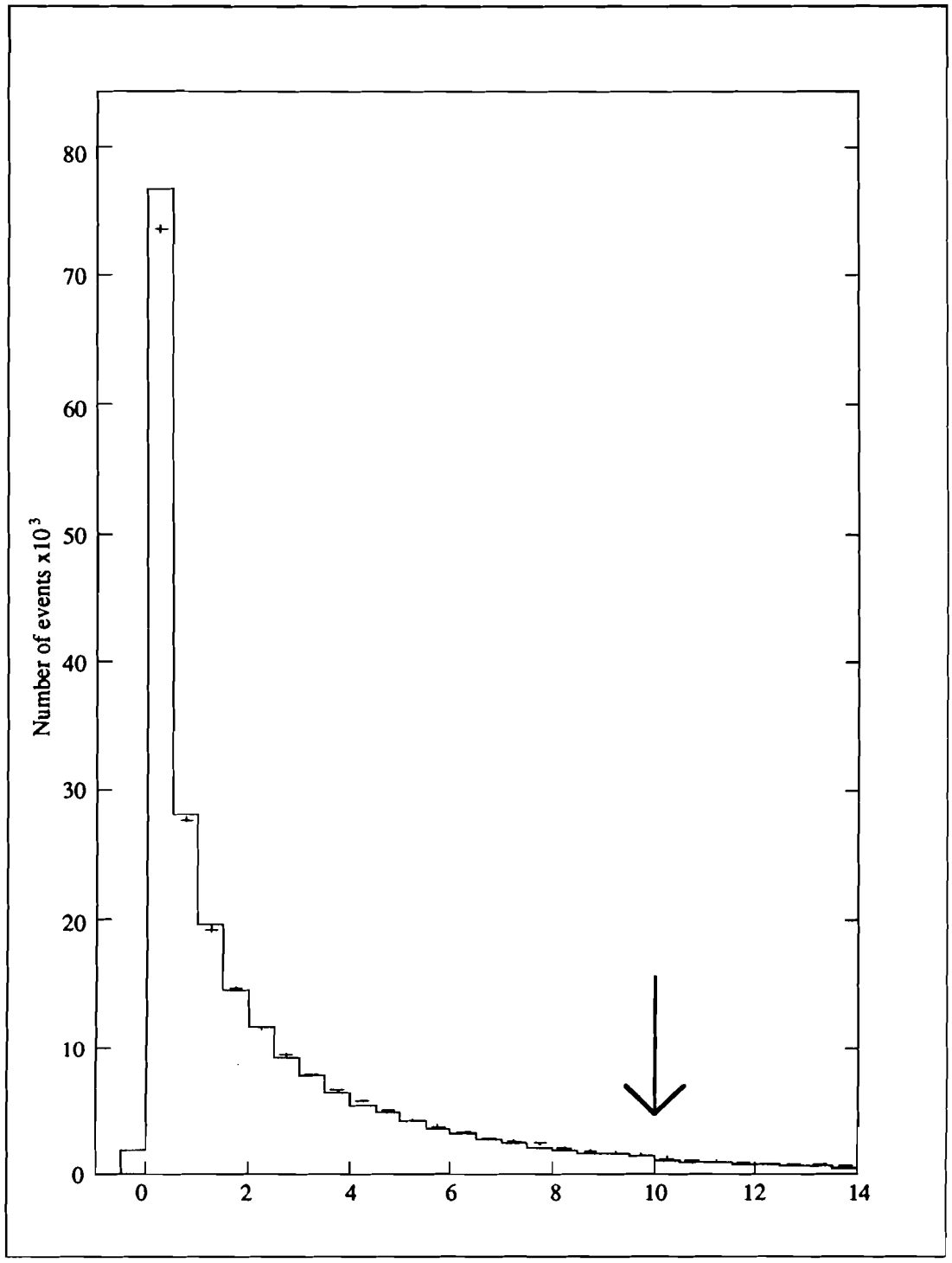

Fig. 3.06 : The difference between the two Λ chi-squares, $\chi^2_k - \chi^2_g$. A cut was made for events with a difference greater than 10, as indicated by the arrow.

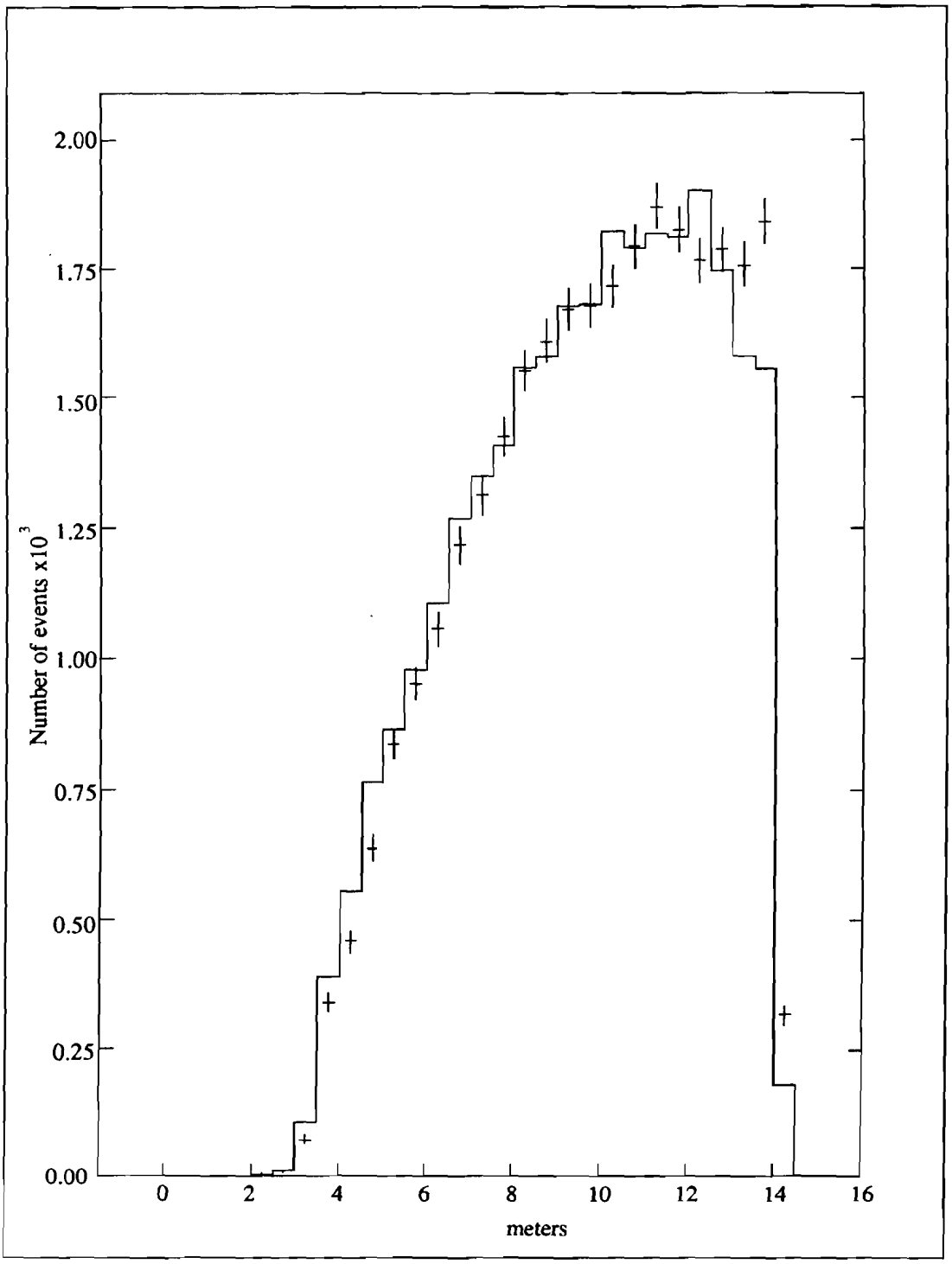

Fig. 3.07 : The $\Lambda \rightarrow p\,\pi^-$ decay vertex distribution, showing the shape typical of daughter decays.

until the minimum χ^2_k, shown in Fig 3.05, was found. The difference $\Delta\chi^2 = \chi^2_k - \chi^2_g$ was used as a background cut; events with a good geometric χ^2 were required to fit the Λ mass well also. A plot of the difference is shown in Fig 3.06; the cut eliminated events with a difference greater than 10. The decay vertex, Fig. 3.07, resulting from the process was required to be within the volume defined by the trigger: downstream of veto S2 and upstream of chamber C2. Of the identified Λ decays, 99% were within the defined decay volume, and 88% of these passed the $\Delta\chi^2$ cut.

3.13 Beam Λ Analysis

A beam Λ is one produced by protons at the production target, as opposed to a daughter Λ from Ξ° decay, or a Λ produced or scattered in any material in the neutral beam. Reconstructed Λ decays which were Λ or Λ' but not G.E. triggers were primarily beam Λ's. There was some contamination, <10%, of this sample by daughter Λ's from Ξ° decays which were not flagged as satisfying the G.E. trigger because neither γ from the π° hit the lead glass. True beam Λ's define the cone of the neutral beam, and have their decay vertex within it. Daughter Λ's tend to decay outside of the beam centroid, due to the momentum available in the decay of the Ξ°. Therefore, beam Λ's were used to define the location of the neutral beam centroid with respect to the MWPC coordinate system.

If the collimator were perfectly aligned with the MWPC coordinate system, then the center of the collimator and the center of the production target would be at the x,y origin. The neutral beam, however, came through the collimator with a slightly different slope than the straight-through proton beam which defined the MWPC coordinate system. Also, the neutral beam centroid could and did vary slighty from run to run due to variations in targeting the proton beam. Projecting beam Λ momentum vectors to a specific x-y plane gave a gaussian distribution of points (x,y) which were centered about a point (x´,y´), called an offset. If the neutral beam were exactly along the coordinate z axis, (x´,y´) would be (0,0). The offset points at the center of the production target (z=-7.01 m) and at a point between S1 and S2 (z=3.35m) were plotted for a whole data tape and the mean values used for later analysis of that tape. A first estimate of the offset values came from projecting the momentum vectors of all identified

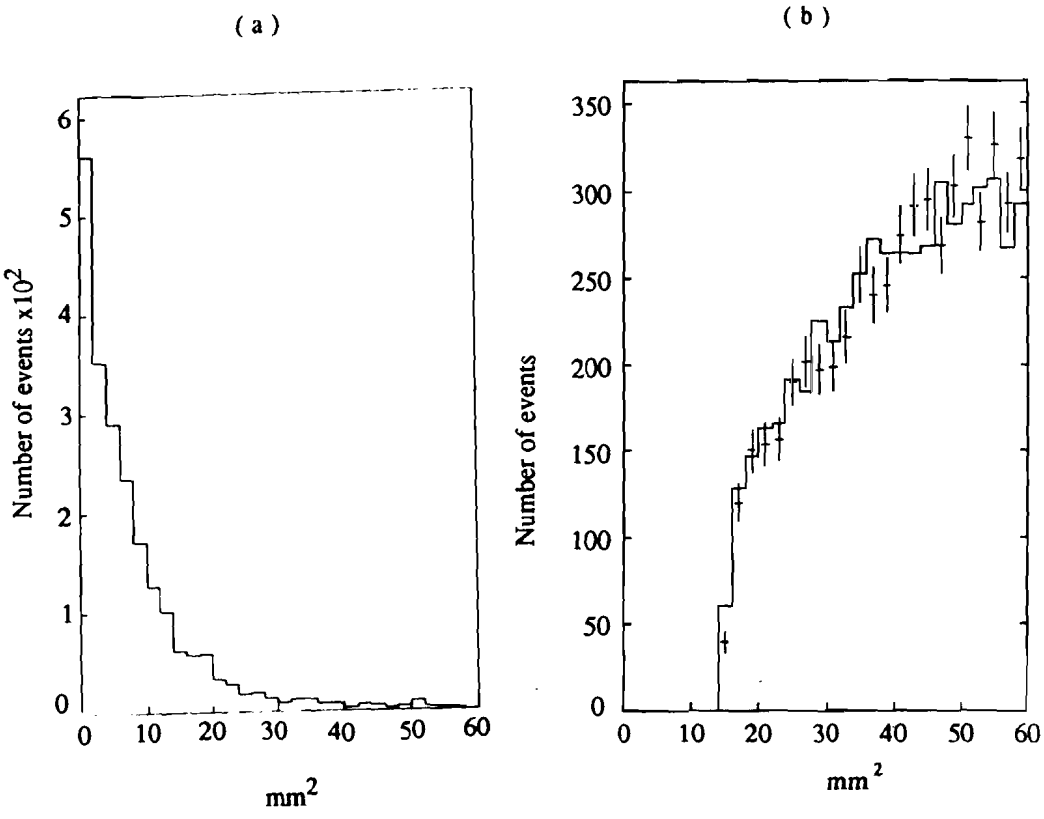

Fig. 3.08 : Distributions of the target pointing parameter R^2 for (a) beam Λ's and (b) daughter Λ's from $\Xi^\circ \rightarrow \Lambda\pi^\circ$ decays, both shown here for a comparison of their shapes. A cut was made, as shown, on the daughter Λ distribution to help reduce contamination of the Ξ° sample by beam Λ's plus accidental γs. Plot (a) shows only data (solid line); plot (b) has data (points) and Monte Carlo (solid line). The two distributions have not been normalized to the same number of events. About 70% of the events for (b) are off the scale of the plot.

Λ's which were not GE triggers. Once rough offsets were known, they could be used to calculate the the target pointing parameter R^2 of the Λ. R^2 is the distance squared between the position that the Λ momentum vector intersects the x-y plane at the center of the production target, and the average beam position at the target center given by the offsets. The offset values were recalculated using better selected beam Λ with an R^2 cut, which required events to have $R^2 < 10$ mm^2. The R^2 distributions for beam Λ's and for daughter Λ's from Ξ° decay are shown in Fig. 3.08.

3.20 Lead Glass Analysis

An event which passed the GE trigger and was identified as a Λ decay next had the lead glass examined for electromagnetic showers. The lead glass analysis found the number of showers present and their energy and position. Events with two γ showers were reconstructed with the Λ as $\Xi^\circ \rightarrow \Lambda\pi^\circ$ decays. The reconstruction of events with a single γ plus a Λ will be discussed in the next chapter. The energy of the gamma came from the pulse heights from the phototubes of the lead glass blocks identified as comprising a γ cluster. The calibration constants were known to first order from the e^+e^- calibration. The block clustering algorithm used to identify γ showers was slightly more sophisticated than the one used in the e^+e^- calibration, mostly in the manner in which the FW clusters were incorporated.

A cluster was defined as a set of contiguous blocks with signals bounded by blocks without signals or by an edge of the array. The main array (MA) was searched for clusters first, then the front wall (FW), and the alignment of all clusters in the two areas was checked. In the MA, at least one block in each cluster was required to contain an energy of 0.8 GeV or greater, and the total energy in the cluster was required to exceed 1.5 GeV. To suppress hadron initiated showers, no MA cluster was accepted which contained more than 7 blocks: a central block plus at most the 6 nearest neighbors. The distribution of the number of MA blocks in a γ cluster from reconstructed π°'s is given in Fig. 3.09 a. The cluster position was found by an energy-weighted average of each hit block's center position, given by Eq. 3.1a, where w_{block} is the x or y center position of the block. The variance in Eq. 3.1b was also calculated for each cluster for both x and y. Limits on the values of the variance effectively required at

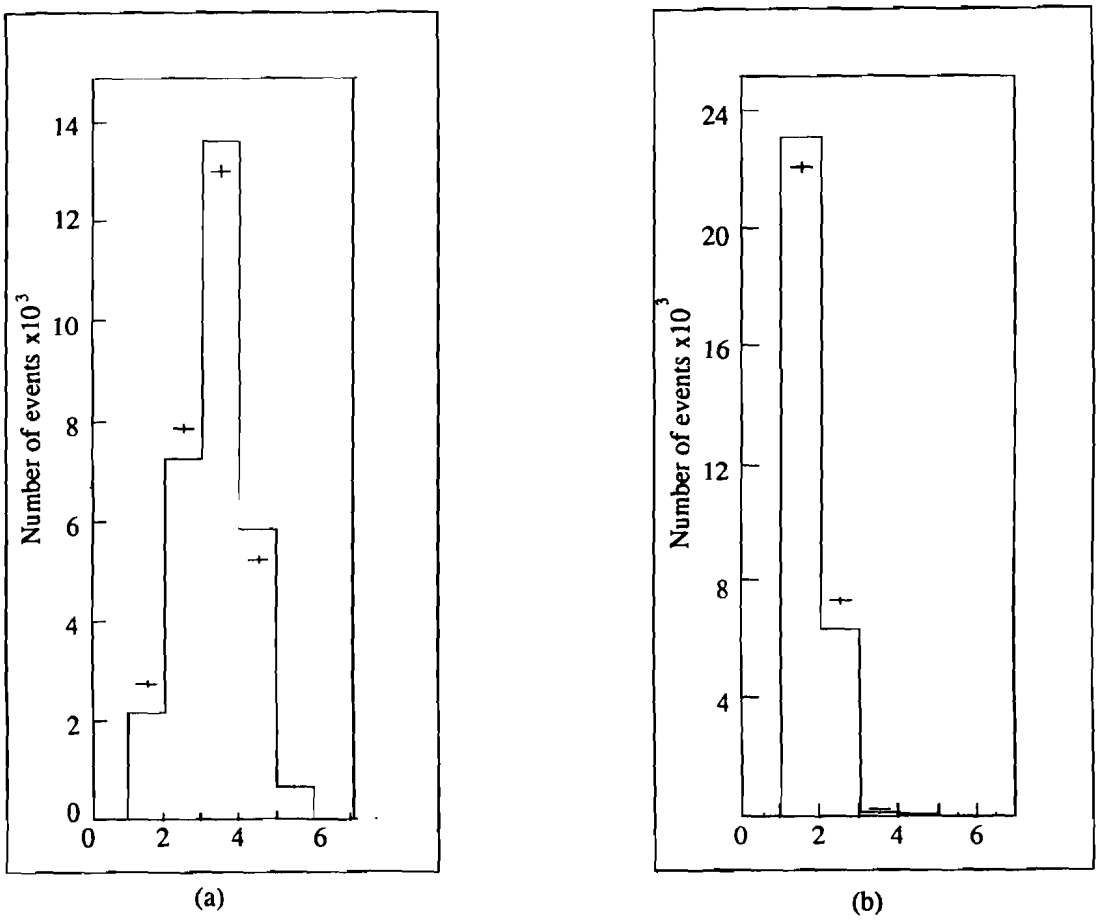

Fig. 3.09 : Distributions of the number of lead glass blocks in a cluster contained in (a) the main array and (b) the front wall.

least 88% of the cluster energy to be contained in no more than 3 adjacent blocks. The variance cut discriminated against hadronic showers, since, if they occur, tend to spread energy out more than γ showers. The cut also discriminated against overlapping showers. 10% of Monte Carlo 2-γ Ξ° events do not pass the 2 shower requirements; however only 1% pass the criteria for 1 shower. The Monte Carlo γ reconstruction efficiency is given in Table 3.1.

$$w_{cluster} = \frac{\sum_{block} (w_{block} \cdot E_{block})}{E_{cluster}} \qquad \text{Eq. 3.1a}$$

$$\text{variance}(w) = \frac{\sum_{block} (w^2_{block} \cdot E_{block})}{E_{cluster}} - w^2_{cluster} \qquad \text{Eq. 3.1b}$$

$$w = x, y$$

Showers found in the MA were then correlated in position with FW hits. Clusters were defined in the FW in the same manner as in the MA, except the energy required was at least 0.4 GeV per cluster, and the number of blocks, Fig. 3.09b, was limited to 4. The shower starts in the FW or in the lead sheet just upstream, and the lateral spread should be less than in the MA. The position of a MA shower was projected to the FW and only 1 to 4 FW blocks were allowed to be assigned to that shower, depending on the way FW blocks overlapped the MA row. If more than 1 FW block with a signal was unassigned to a MA shower, or if the unassigned block had an energy greater than 0.3 GeV, the event was eliminated from the data sample.

In special cases where the γ hit the FW near a vertical or horizontal boundry between two blocks, the energy sharing between those blocks gave a more accurate estimate of the x or y position than using the MA information alone. In these cases only the position information from the FW shower was used. Otherwise the x position from the FW shower was averaged with the x of the MA shower, and the y position came only from MA information. The spatial resolution depended on which of these cases were in force; the special cases had a more accuratly determined position. The average spatial resolution, determined from the e^+e^- data, was 1.5 cm.

The p and π^- tracks were extrapolated into the glass to see whether they caused one or part of one of the shower clusters detected. If the p hit any glass block and its position at the glass was within one block diagonal, 11.4 cm, of any shower center, then that cluster was eliminated from the list of gamma showers. If the π^- was tracked into the glass the event was eliminated; this made up for any inefficiency in the veto counters S7 and S7a.

3.21 TDC Rematching

Accidental coincidences between Λ events in the spectrometer and lead glass showers were reduced by measuring the time difference between the trigger and the γ hit using time to digital converters, or TDC's, which gave two counts per nsec. The TDC's had a memory buffer so that it was possible to store several events before readout. The experiment did not intend to use this feature, and a read and clear command was issued to the module after each event. The clear function failed, however, giving rise to a problem which caused TDC information from one event to be written into the data buffer of a different event. The problem was not discovered until after the experiment, and the data was 're-matched' in the offline analysis. The signals sent to the glass TDC unit passed through an amplifier and then a discriminator. The discriminator signal had to be above a certain threshold to register TDC information. Due to gain variations, the threshold energy from block to block varied from 0.4 to 5.5 GeV. The re-matching could only be done on events which had TDC hits, and requiring the event to have this information was in effect an energy cut. Also, since a 2-γ event has more blocks hit than a 1-γ event, the 2-γ event was more likely to be matched. A software energy cut of 6 GeV per cluster for 2-γ events, and 12 GeV for 1-γ events was made in the analysis of both data and Monte Carlo events to even out a possible bias. The timing cut required the γ to hit the glass within $\pm$10 nsec of the Λ trigger. If a non-shower block was out of time, only the block was eliminated. If the block was contained in a shower, the event was eliminated. After the energy cut and matching cuts, about 3% of the events did not pass the timing cut.

3.30 Ξ° Reconstruction and Kinematic Fit

There were 2.2 x 10^5 events detected with a reconstructed Λ and 2 or 3 showers in the lead glass. The reconstructed Λ was required to pass the kinematic cuts described in section 3.12. The glass could contain 2 or 3 clusters. Events with 3 clusters were allowed since one of the clusters may have been energy deposited by the proton; if one of the 3 clusters was not due to the proton, the event was not used in the Ξ° reconstruction. Any event with signals in the γ detectors S3 or S4, described in section 2.20, or with signals in the part of C4 covering the scintillators, were excluded from the data sample. Each γ shower in the glass was required to have an energy of at least 6 GeV, and pass the timing cuts. Events with 2 and only 2 showers were sent through the Ξ° analysis, which tested the decay chain hypothesis $\Xi^\circ \rightarrow \Lambda\pi^\circ$, $\Lambda \rightarrow p\pi^-$, $\pi^\circ \rightarrow \gamma\gamma$.

A Ξ° kinematic fit was developed to reconstruct these events assuming the $\Xi^\circ \rightarrow \Lambda\pi^\circ$ decay chain. The momenta of the charged particles from Λ decay and the Λ momentum and decay vertex were known from the Λ reconstruction. Also the energies and positions of the 2 γ's were measured by the lead glass array. Both the Λ and the 2γ's must fit to a common vertex, since the π° decays almost instantaneously. The Ξ° decay point is not known, but is constrained to be along the path of the Λ momentum vector and within the cone of the neutral beam as defined by the beam Λ's, discussed in section 3.13. The Ξ° momentum direction is constrained to be along the line drawn from the chosen vertex and through the defining aperture of the collimator, to the production target position. The initial Ξ° decay position was found by projecting the Λ vector to an x,y plane at z=0.4 of the distance between the downstream face of the hyperon magnet (z=0) and the Λ decay z position. The whole fit was performed, forcing the masses of the Λ, π° and Ξ°, and varying the measured parameters within their errors. The vertex was then moved along the Λ momentum vector line,within the neutral beam cone, until the minimum χ^2_Ξ was obtained. The vertex was not allowed to go downstream of the Λ vertex, but there was no constraint in the upstream direction. The final output for the best χ^2_Ξ was a z position of the Ξ° decay, and fitted momentum vectors for all the particles: Ξ°, Λ, π°, $\gamma 1$, $\gamma 2$, p, π^-.

The Ξ° kinematic fit could be used in three modes. One is described above, and is the case when

all the particles in the decay chain have been detected. A second mode is used when only one of the two γ's has been detected, and will be discussed in section 4.32. The third mode is similar to the first and is discussed in the following section. These techniques have been used in previous experiments[20].

3.31 π° Bootstrap Calibration

The Ξ° kinematic fit could be done without constraining the two γ energies to their measured values as calculated using the e^+e^- calibration constants. The Ξ° events reconstructed this way were allowed to vary the γ energies to fit to the best π° mass, yet constraining the π° momentum to fit the $\Xi^\circ \rightarrow \Lambda\pi^\circ$ hypothesis. In practice this proceedure was implemented by making the γ energy resolution artificially large, increasing it by two orders of magnitude from its measured value. The fit then had room to vary the measured energies without the χ^2_Ξ function becoming large. The χ^2_Ξ is shown in Fig 3.10, and has the expected shape for a one-constraint fit.

For events with $\chi^2_\Xi < 4$, the γ energies emerging from the fit, $E1_j$ and $E2_k$, were used to calibrate the lead glass array in the same way as the measured e^+e^- energies in Eq. 2.1. The χ^2_Ξ cut was severe and greatly reduced the number of events which were used for the π° bootstrap calibration, as it was called. The bootstrap gave a continuous running check on the overall calibration, since there were typically 1000 π°'s from $\Xi^\circ \rightarrow \Lambda\pi^\circ$ decays on every data tape, before cuts. The proceedure automatically gave a more precise calibration to those blocks used most often for Ξ° events. Edge blocks which may have lost some energy out their sides had their calibration values pulled higher by the bootstrap to make up for the loss; if too much energy was lost, though, the event was penalized by being given too high a χ^2_Ξ to be used for the bootstrap. A fiducial volume cut on the position of the showers in the array was made to reduce the number of events which might lose a large proportion of energy out the edges of the array. The cut was not, however, as large as that used in the final analysis, because the number of events then used by the bootstrap became too small, and statistical fluctuations became too large. A 'middle ground' was found using a cut on shower positions 4.0 cm inside all the outer edges and 4.0 cm around the edge of the hole. After preliminary Λ and γ energy cuts, 97% of the $2\gamma + \Lambda$ events were

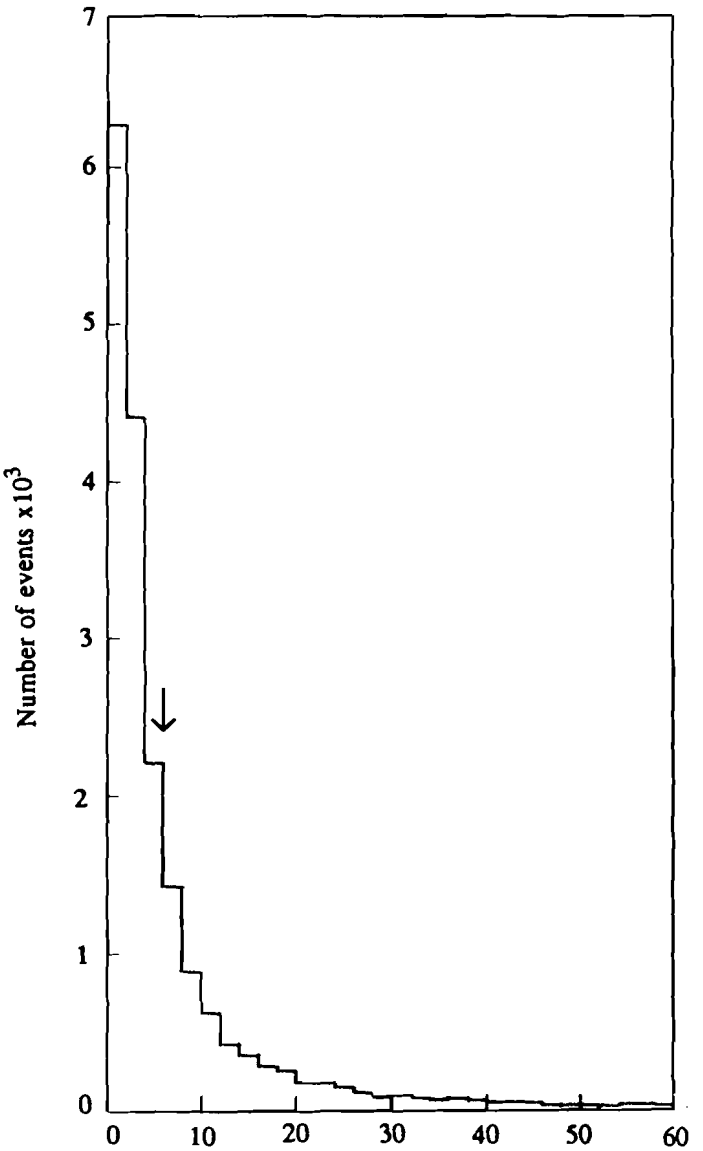

Fig. 3.10 : The chi-squared distribution, χ^2_{Ξ}, for the 1-constraint fit to the decay chain $\Xi^\circ \rightarrow \Lambda\pi^\circ$, used in the π° bootstrap glass calibration. Events used for the calibration were required to have a value of $\chi^2_{\Xi} < 4$, shown by the arrow.

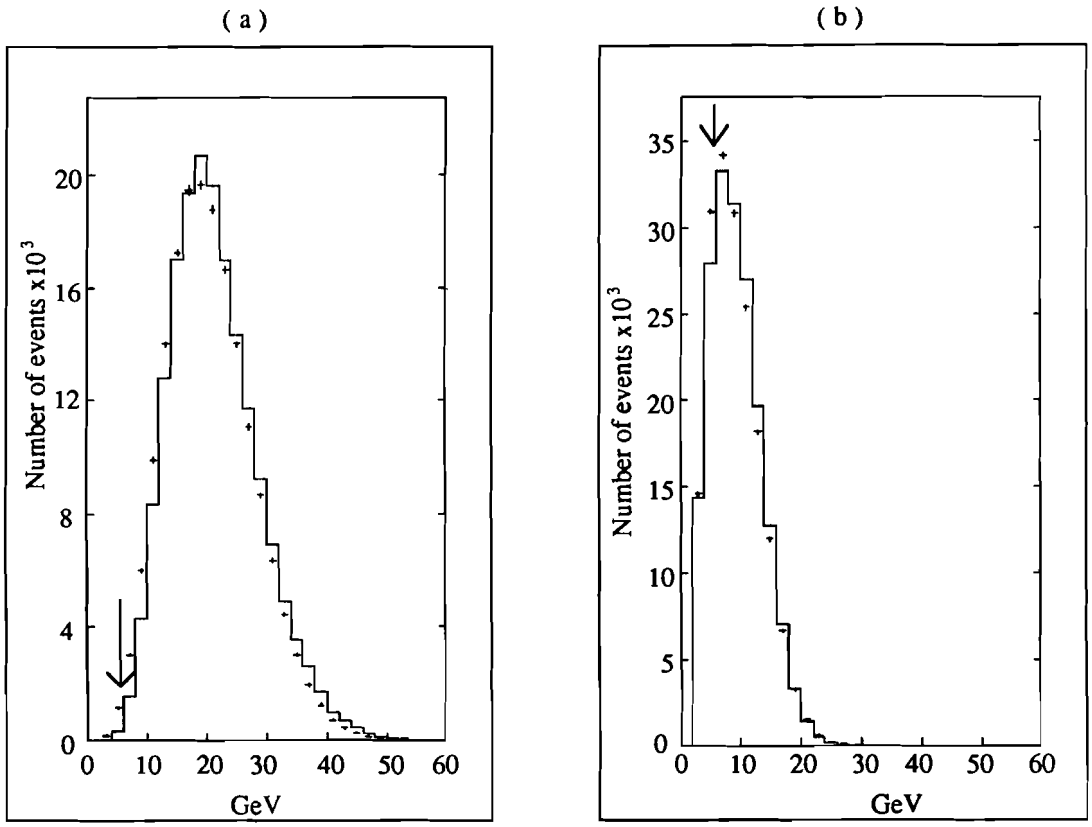

Fig. 3.11 : Distributions of the higher (a) and lower (b) gamma energies after the bootstrap calibration, but before the final Ξ° reconstruction cuts. The arrows show where the 6 GeV cut was made.

inside the fiducial volume.

The mean values of the calibration constants from the bootstrap were used for all subsequent Ξ° analysis, both $\Xi^\circ \rightarrow \Lambda\pi^\circ$ and $\Xi^\circ \rightarrow \Lambda\gamma$. The average values from the π° bootstrap typically fell within 1 σ of the e^+e^- calibration values. A few blocks changed their calibration dramatically during the experiment, and the tape by tape bootstrap calibration was a helpful monitor. The calibration constants for blocks near the center rose slowly (2%) during the course of the experiment due to radiation damage. Fig. 3.11 shows the γ energies after the bootstrap calibration and before any final analysis cuts.

3.32 Final Ξ° reconstruction

The 2-γ data were sent through the Ξ° kinematic fit again, this time with the energy errors on the gammas at their measured values, and using the π° bootstrap calibration constant values. The lead glass fiducial volume cut was increased to match that used in the 1-γ analysis. The cut eliminated events within 5.56 cm., or 1/2 block plus 0.5 cm., from any edge. Events passing all the basic Λ and γ cuts discussed so far were sent through the Ξ° fit; these cuts and their effects are given in Table 3.1.

The decay vertex for the Ξ° was sometimes located inside the collimator; a cut required it to be no more than 1.0m inside, at a z position of -1.0m. Monte Carlo Ξ°'s which decayed within the defining aperture of the collimator (< -1.98m) did not pass their decay products into the apparatus. A Ξ° with a generated decay vertex of 0.0m, however, often reconstructed to a fitted vertex less than that; the Ξ° vertex resolution was about $\pm$1.0m. The loosest reasonable cut on the vertex was found to be at -1.0m. The z position of the Ξ° decay vertex is shown in Fig. 3.12.

The Ξ° and π° masses were reconstructed using the fitted vertex and measured γ energies and Λ momenta. If the fitted momenta were used, the resulting Ξ° mass would have no resolution width, because the mass was forced in order to calculate the fitted momentum vectors. The reconstructed π° momentum vectors were calculated from the measured γ energies and positions, and the fitted Ξ° vertex. The Ξ° momentum vectors were calculated from the fitted vertex, the reconstructed π°, and the Λ from the kinematic fit described in section 3.12. The reconstructed Ξ° momentum vectors were used to

determine the angular divergence of the Ξ° beam from the beam centroid direction given by the offsets described in section 3.12. Fig. 3.13 shows the angular divergences Θ_x and Θ_y, with respect to the beam centroid. A cut was made requiring each Θ to be between ± 0.30 mrad. The transverse momentum p_t of the Ξ° with respect to the beam centroid is shown in Fig. 3.18. The p_t variable was important for the 1-γ analysis, and will be discussed more in the next chapter. The distribution is included here to show the comparison between fully reconstructed Ξ°'s where both γ's were detected.

The χ^2_Ξ distribution is shown in Fig 3.14. A cut was made at $\chi^2_\Xi > 30$ to eliminate badly reconstructed Ξ°'s. The shape is different from the χ^2_Ξ in the π° bootstrap, because the γ energy information is now well measured and the fit becomes 3 constraint instead of 1 constraint. The R^2 for the Ξ° is shown in Fig 3.15, and it is clear that these events originated in the production target. A cut was made, retaining Ξ° with $R^2 < 35$ mm^2. The R^2 of the Λ, Fig. 3.08, was required to be greater than 15 mm^2. The results of these cuts is also in Table 3.1.

The resolution of Ξ° reconstruction is not as good as for Λ, as can be seen from the R^2 distribution and also from the Ξ° mass. Both the π° and Ξ° masses, Fig 3.16 and 3.17, have a FWHM of 25 MeV, compared to the Λ mass width of 4 MeV. All the resolution for Ξ° comes from the resolutions in the lead glass and from the uncertainty in the decay vertex position. There were 2.95 x 10^4 of these well reconstructed $\Xi^\circ \rightarrow \Lambda\pi^\circ$ decays, used in the determination of the branching ratio.

3.40 Monte Carlo

Fig 3.01 through 3.17 compare various data distributions with $\Xi^\circ \rightarrow \Lambda\pi^\circ$ Monte Carlo events. In all these plots, the solid line represents the monte carlo and the crosses are data points with their statistical errors. The Monte Carlo has four times more events than the data. In the next chapter, the Λ-γ analysis will be discussed, and how a $\Xi^\circ \rightarrow \Lambda\gamma$ signal was observed. Since the previous, and only, measurement of the branching ratio $\Xi^\circ \rightarrow \Lambda\gamma / \Xi^\circ \rightarrow \Lambda\pi^\circ$ is essentially an upper limit,[16] a high statistics result was not expected (<500 events). For this reason, a comparison of $\Xi^\circ \rightarrow \Lambda\gamma$ Monte Carlo events to observed $\Xi^\circ \rightarrow \Lambda\gamma$ events is not a sensitive test of the behavior of the apparatus or of the analysis

Table 3.1

2-γ $\Xi^0 \rightarrow \Lambda\pi^0$ analysis cuts

cut requirement	fraction of data passing	fraction of Monte Carlo passing
MC Λ reconstruction efficiency		0.78
MC γ reconstruction efficiency		0.70
-0.3 mrad < $\Theta_{x,y}$ < 0.3 mrad	0.88	0.92
Λ inside decay volume limits	0.99	0.99
$\chi^2_k - \chi^2_g < 10$	0.88	0.91
TDC matched with event	0.86	----
both γ > 6 GeV	0.74	0.77
γ in time with trigger	0.97	----
γ inside glass fiducial volume	0.40	0.40
z of Ξ^0 decay vertex > -1.0	0.95	0.96
$\chi^2_\Xi < 20$	0.78	0.79
$R^2_\Lambda > 15$ mm^2 ; $R^2_\Xi < 35$ mm^2	0.95	0.95
total effect of cuts	0.133	0.184
total MC 2-γ analysis acceptance		0.00999

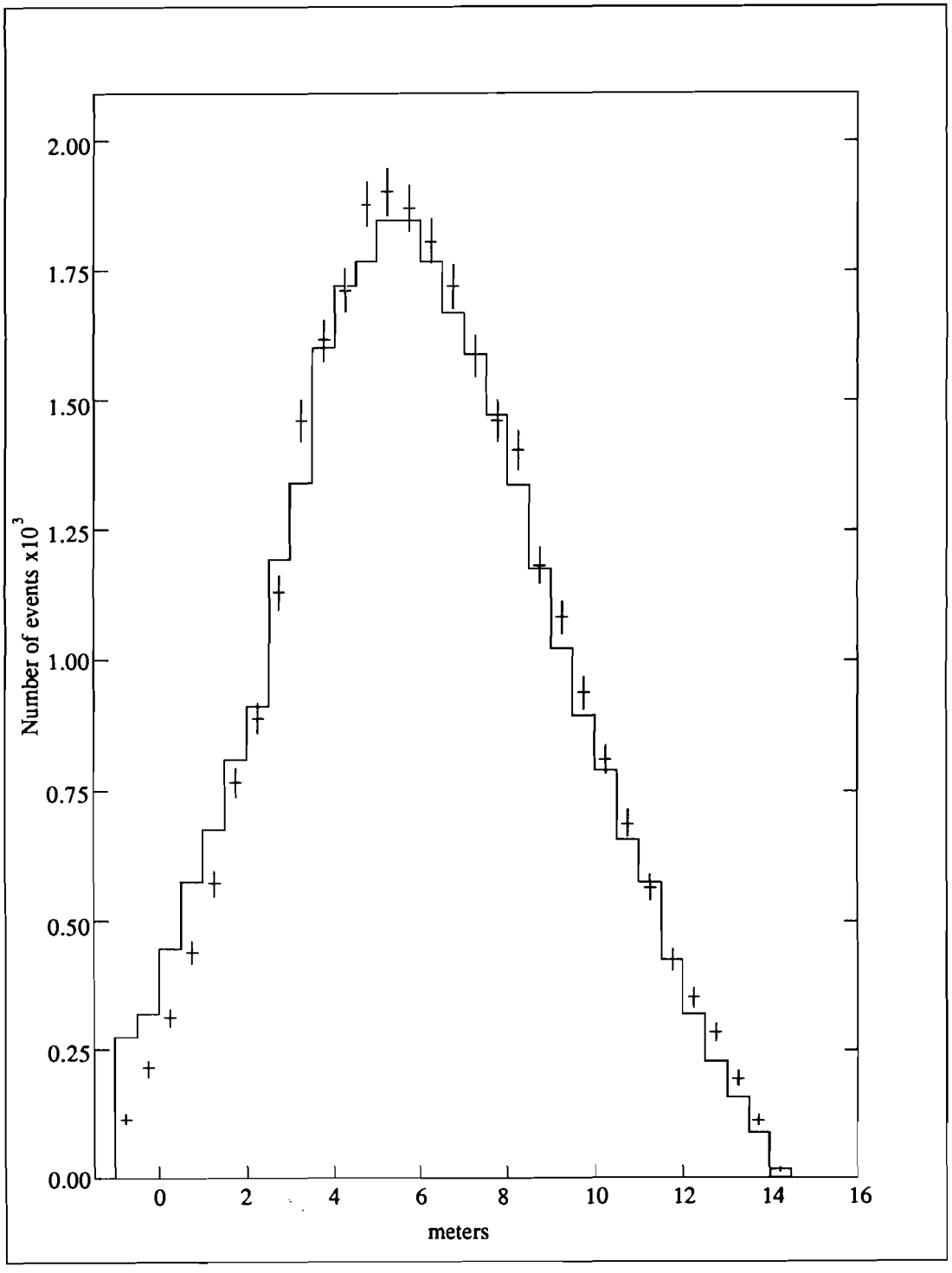

Fig. 3.12 : The $\Xi^{\circ} \rightarrow \Lambda\pi^{\circ}$ decay vertex distribution.

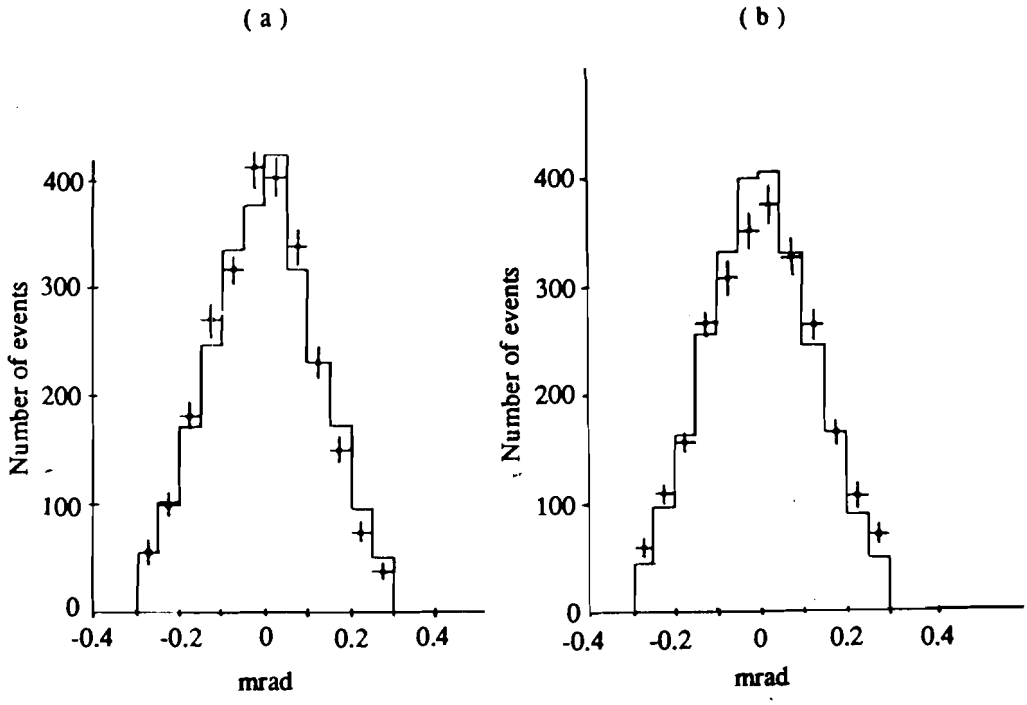

Fig. 3.13 : The divergence Θ_x, (a), and Θ_y, (b), of the Ξ° beam, measured in mrad from the beam centroid. The data points are a fraction of the total data sample.

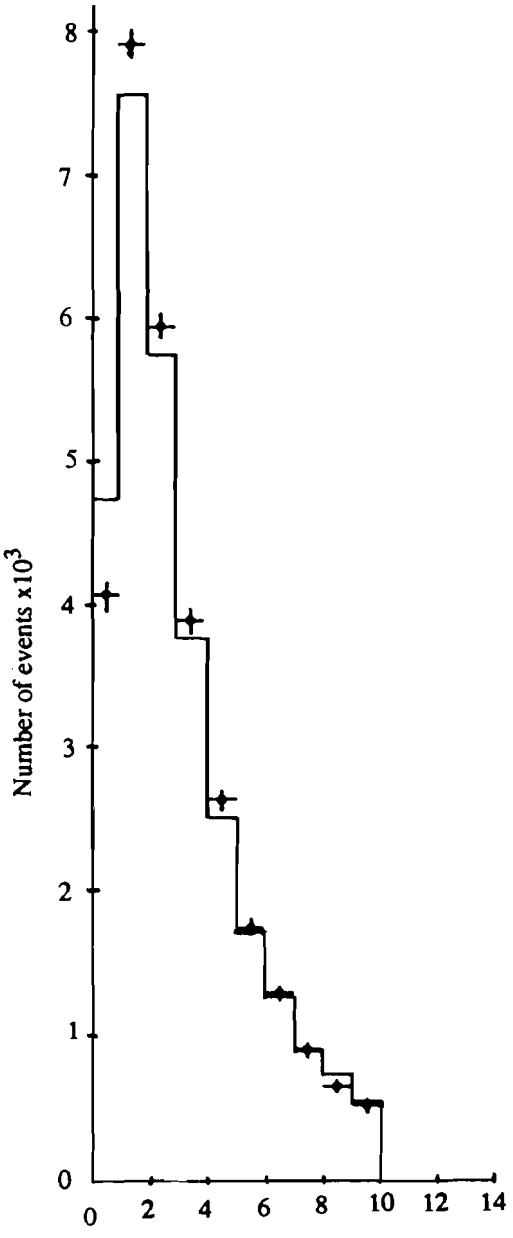

Fig. 3.14 : The chi-squared χ^2_{Ξ} from the 3-constraint fit to the $\Xi^\circ \rightarrow \Lambda\pi^\circ$ decay chain.

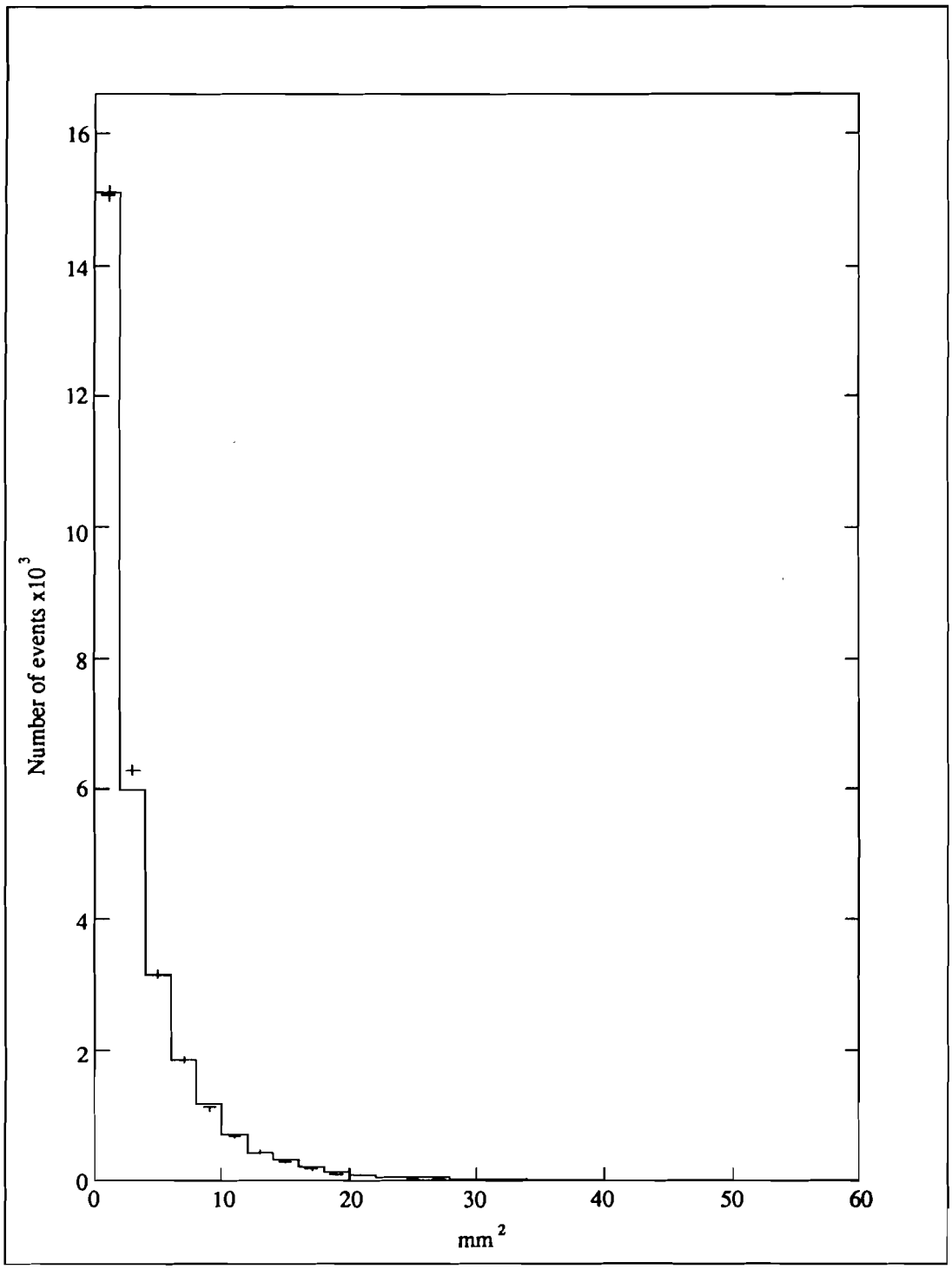

Fig. 3.15 : The distribution of the target pointing parameter R^2, for the Ξ° reconstructed from $\Xi^\circ \rightarrow \Lambda\pi^\circ$ decays. A cut was made on events with $R^2 > 35 mm^2$.

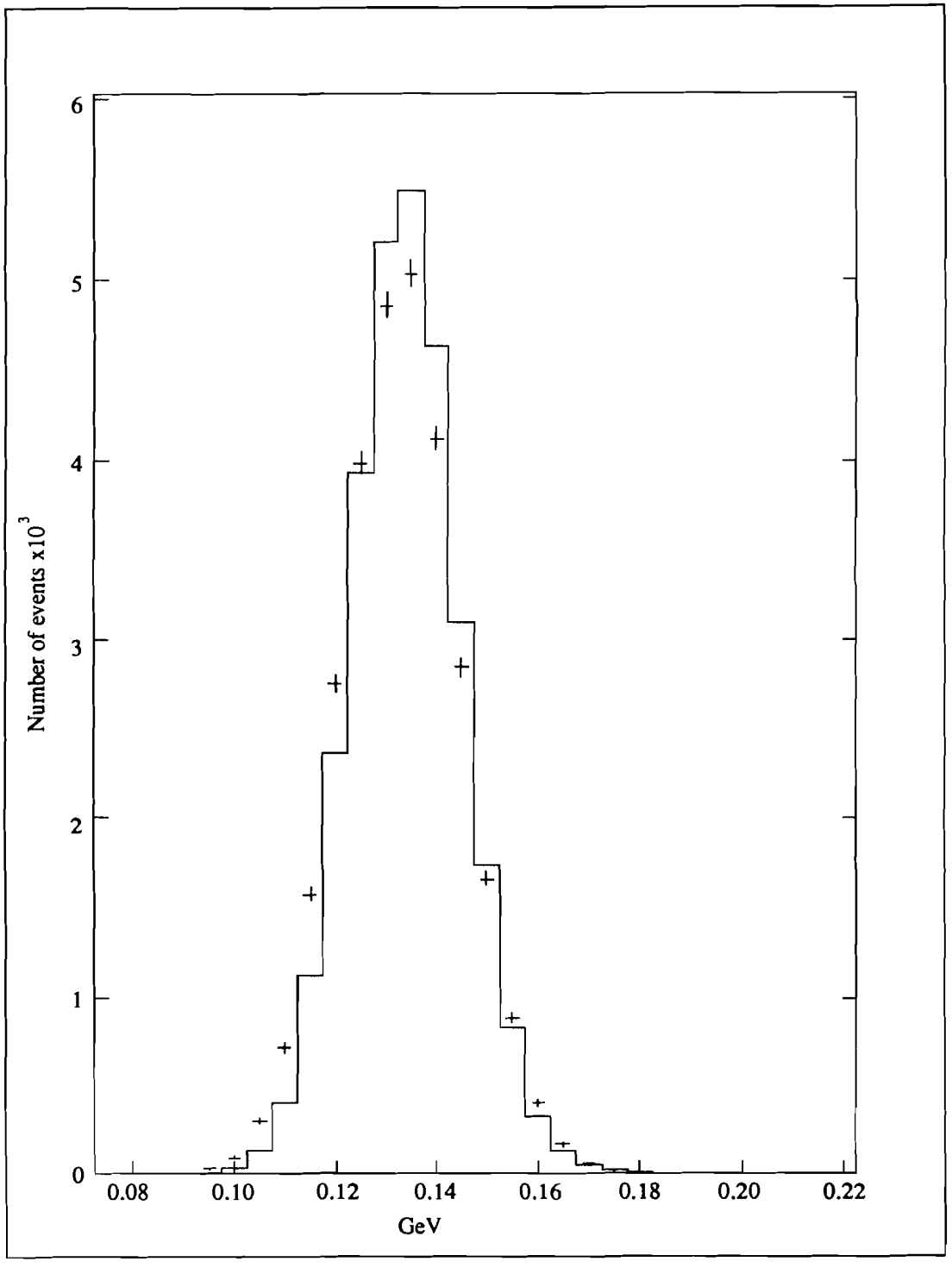

Fig. 3.16 : The mass distribution for reconstructed $\pi^\circ \rightarrow \gamma\gamma$ decays, for π°'s from $\Xi^\circ \rightarrow \Lambda\pi^\circ$ decays.

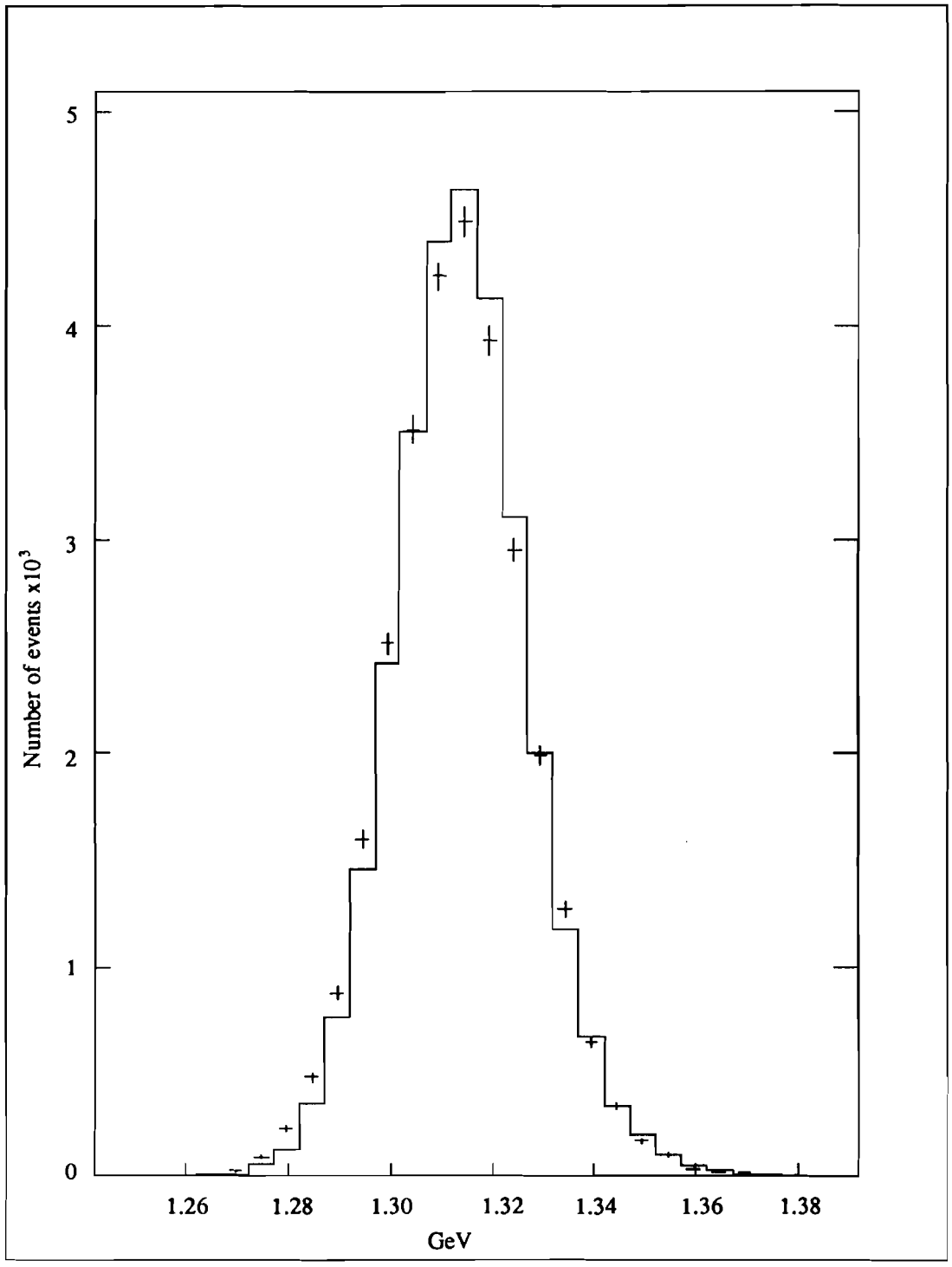

Fig. 3.17 : Ξ° mass, from fully reconstructed $\Xi^\circ \rightarrow \Lambda\pi^\circ$ decays.

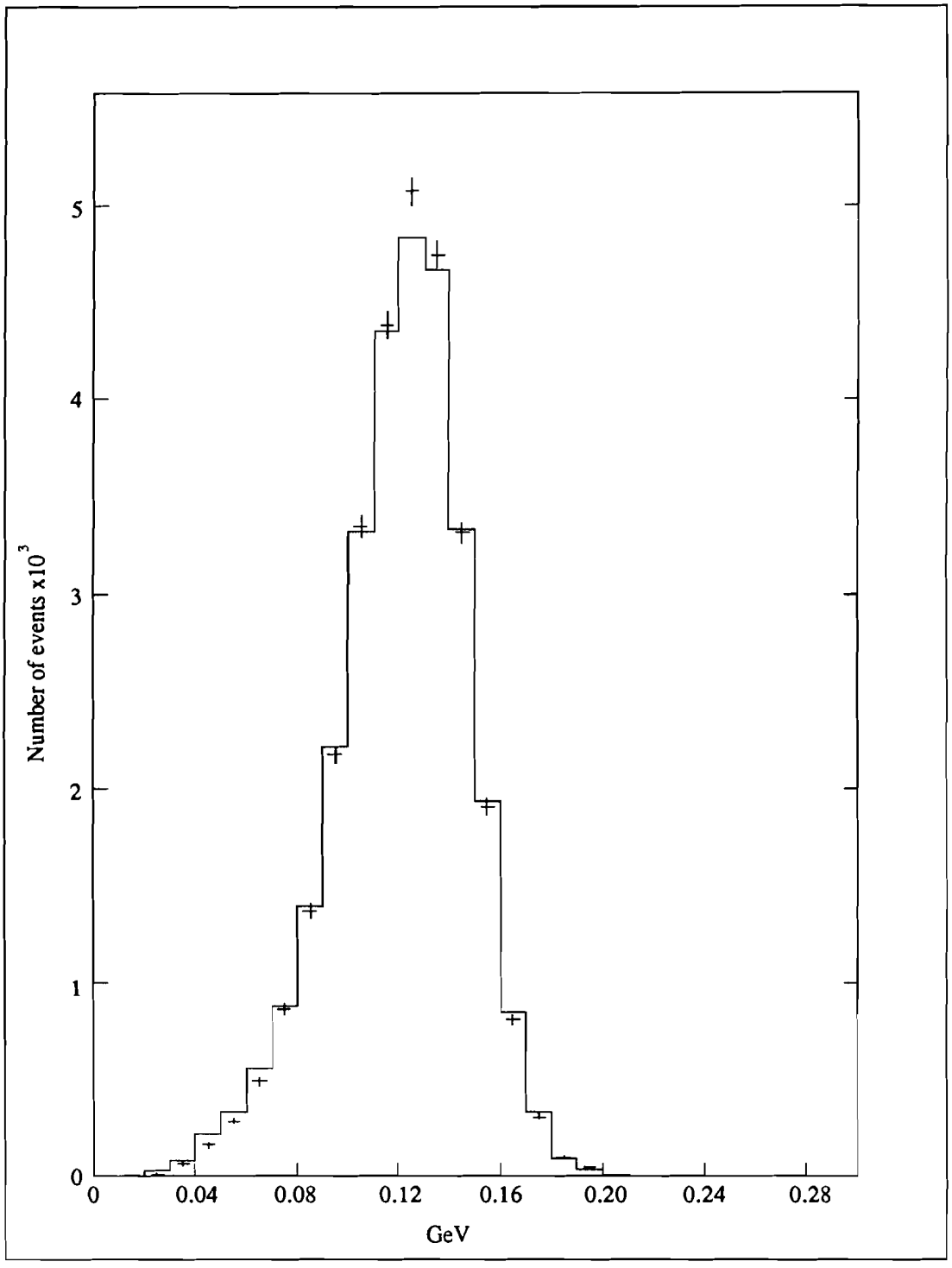

Fig. 3.18 : The transverse momentum with respect to the beam centroid, P_t, of the Λ from fully reconstructed $\Xi^\circ \rightarrow \Lambda\pi^\circ$ decays.

software. The experiment achieved good statistics for $\Xi^\circ \rightarrow \Lambda\pi^\circ$ decays, however, and the basic Monte Carlo program was tuned to correspond to this data sample as well as possible. A good correspondence means the apparatus is understood, and monte carlo programs for background and signal decay modes can be depended upon. Also, the acceptances for $\Xi^\circ \rightarrow \Lambda\pi^\circ$ and $\Xi^\circ \rightarrow \Lambda\gamma$ decays figure directly into the calculation of the branching ratio, and come out of the Monte Carlo.

The Monte Carlo simulation creates Ξ°'s coming out of the production target and through the defining collimator, decays them in flight and gives energy and momentum to the daughters according to relativistic kinematics. The detectable decay products are traced through the apertures of the apparatus and tested as to whether they satisfy the trigger requirements of the experiment. Monte Carlo events which passed the trigger were given the same digitized format as the data, and passed through the same analysis process as the data. This section will describe the Monte Carlo generation of $\Xi \rightarrow \Lambda\pi^\circ$ decays, and discuss the various methods used to simulate experimental resolutions.

The input momentum spectrum for Ξ° was obtained empirically from the data. The spectrum was required only to reproduce the observed Ξ° momentum distribution after acceptance and analysis cuts. The empirical method started with a flat spectrum which was compared to data and corrected; an acceptable match was obtained after several iterations. The spectrum was integrated and correlated with numbers between 0 and 1, so that a chosen random number would correspond to the probability that a Ξ° would have that magnitude of momentum. Fig. 3.19 shows the Ξ° momentum spectrum.

The momentum direction was determined by a line connecting a point in the production target and a point at the (x,y) plane of the defining collimator aperture. The points selected in each location were chosen to be within certain probability distributions. The radial distribution of target points was proportional to the solid angle on the cross section of the target as seen by the proton beam. The radial distribution of collimator points was gaussian with a width of 1 mm. The selection of collimator points was modified by a transverse momentum dependence observed in hyperon production cross sections.

Because of the finite size of the defining aperture and the length of the production target, Ξ°'s which could enter the spectrometer had a production angle range $\Delta\theta_p = 0.8$ mrad. The transverse

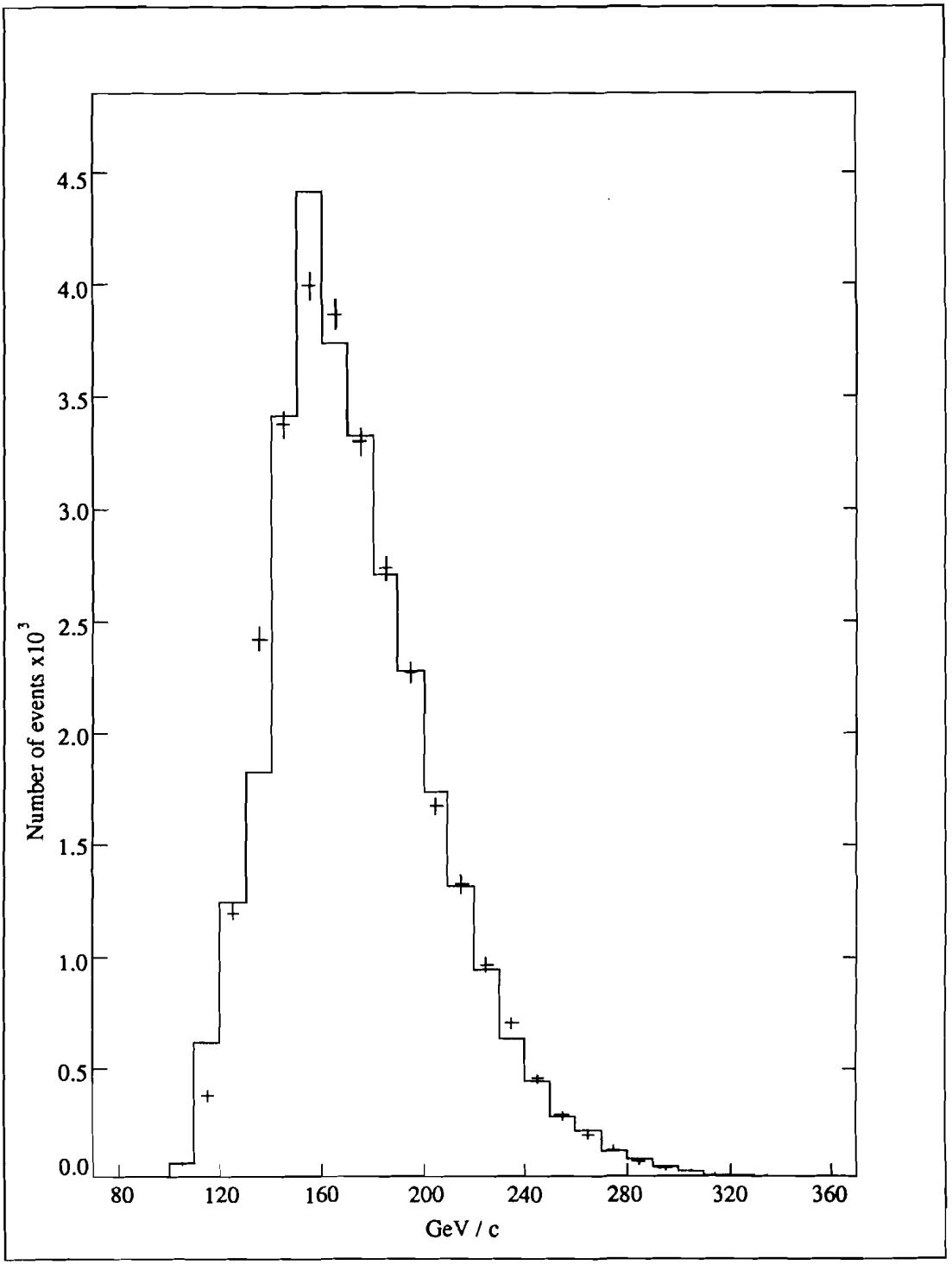

Fig. 3.19 : The momentum spectrum for $\Xi^\circ \rightarrow \Lambda\pi^\circ$ decays.

momentum, p_t, of the Ξ° 's is $|p| \cdot \theta_p$; and the production cross section of Ξ° varies as $\exp(-1.2p_t^2)$.[17] In other words, there is a higher probability for Ξ° to be produced at low p_t than at higher p_t. The effect is a slight bias in the distribution of Ξ° across the collimator : more events are produced which lie on the low p_t side of the collimator. The probability distribution was, like the momentum spectrum, correlated with numbers between 0 and 1. The angle θ_p between the proton beam and the line connecting the two points chosen at the target and collimator was calculated. A momentum was chosen from the spectrum and the p_t value calculated. The likelihood for the resulting p_t value came from comparing the correlated probability distribution to a random number.

The Ξ° decay length was calculated from $\gamma \cdot \beta \cdot c \cdot \tau \cdot (-\ln (\text{random number}))$, where γ and β are the relativistic boost variables of the Ξ°, and $c\tau = 8.69$ cm[22] is the mean lifetime. A Ξ° which decayed before or in the defining aperture was dropped from the data sample. Those which decayed between the aperture and the collimator exit were required to have the Λ and at least one γ clear the exit aperture and enter the spectrometer.

There was material in the beam in which neutral particles could interact through strong forces. Measurements of baryons scattering have been done, although none at the Λ or Ξ° energies in this experiment. Ref. 21 was used to get approximate values for the angular distribution of incoherent scattering from nuclei. The probability distribution for scattering angles was given by e^{-12t}, where $t \sim p_t^2$. The probability that a given particle would scatter at all was given by the number of collision lengths, λ, of material present, and the scattering probability was $1 - e^{-\lambda}$. The Ξ°'s were scattered in the uranium of the γ filter; Ξ°'s and Λ's were scattered in the upstream scintillators, the Primakoff target and decay volume vacuum windows.

The angular divergence of the beam of Monte Carlo Ξ°'s did not match the data if the defining aperture of the collimator was a hard-edged 2 mm. diameter hole. The data contains events which were produced in or scattered through the edges of the defining collimator. The gaussian distribution of points in the collimator gave tails on the beam divergence plots, Θ_x and Θ_y, but the tails were not large enough unless the radius of the aperture was allowed to extend 0.23 mm. further. The combination of

gaussian width at the collimator and aperture size were optimized to match the data after the Θ cuts described in section 3.32 were applied. The larger tails on the data Θ_x and Θ_y distributions stemed from collimator produced Ξ^0's. Fig. 3.13 compares the data to the Monte Carlo distributions after the cuts.

Some of the simulations described so far would have an almost unnoticable effect individually applied. Their inclusion in the Monte Carlo developed over time, and always in response to some distribution which did not match the data. For example, in addition to all the above target and collimator effects, the generated Ξ^0 'beam' was also given an offset with respect to the spectrometer coordinate system as described in Sec. 3.13. If the offset was not included, the Monte Carlo Ξ^0's probed slightly different regions of the spectrometer than the data. Any effect which could be seen was included.

A Ξ^0 which decayed upstream of the Primakoff target was sometimes self-vetoed when one of the γ's converted in material, sending charged particles into the veto scintillators S1 or S2. The largest amount of material, the Primakoff target, and target mover and holder, lay between S1 and S2. A diagram of the Primakoff target holder is shown in Fig 2.06. Each target was held at the downstream end of a long aluminum tube and inserted into the capped cylinder of scintillator S2. The tubes were mounted on a structure which could move forward or backward, to insert or remove targets from the scintillator, and rotated to change targets. The diameter of the aluminum tube, and of the Primakoff targets, was 2.0 cm, and the FWHM of the neutral beam at the point of the Primakoff target was 0.5 cm. Therefore Ξ^0's and beam Λ's did not intersect the material of the aluminum tube. Even daughter Λ's from Ξ^0 decays kept within the diameter of the tube; so strong scattering of these neutral particles was not necessary in the target holder, but only in the Primakoff targets themselves.

The π^0 from a Ξ^0 decay, however, has a lower laboratory momentum than the Λ, and consequently a larger laboratory angle from the neutral beam. The subsequent π^0 decay gives the γ's an even greater divergence. The γ's do indeed intersect parts of the Primakoff target holder, and the surrounding veto counter, S2. A γ passing through λ radiation lengths of a material has a probability $e^{-7\lambda / 9}$ [22] of converting. The Primakoff targets and most other materials in the beam had known radiation lengths which were approximately independent of the γ trajectory. If a γ passed through part of

the aluminum tube or S2 scintillator, however, the number of radiation lengths depended on the path taken. The monte carlo tracked each γ through the Primakoff target region and summed up the total radiation length of each material it traversed. A significant number of these γ's passed through enough of the aluminum tube that they were almost certain to convert and self-veto in S2. Of all Ξ°'s in the apparatus, about half have decayed before reaching the Primakoff target. Of those that have decayed, about 43% had at least one γ, and sometimes both, which passed through part of the aluminum tube and scintillator. Only 18% of the Ξ°'s that had decayed sent both γ's through the Primakoff target alone. With no Primakoff target present, about 30% of the Ξ°'s which could self veto, do, mostly due to intersections with the aluminum tube. That is 15% of the total number of Ξ°'s in the apparatus, and was a noticable effect in the Ξ° acceptances. If the Primakoff targets were present, an even greater proportion of Ξ°'s self-vetoed, up to 27% of all Ξ°'s in the apparatus. The decay vertex distribution, Fig. 3.12, never had good agreement between data and Monte Carlo until the γ self-vetoing effect was installed. Without it, the Monte Carlo distribution had too many events with a decay vertex < 3m.

Once the Primakoff target area was passed, the γ acceptance was checked, and events which did not have at least one γ in the lead glass were dropped. The γ showers were simulated by distributing the energy of a γ among the lead glass blocks surrounding the γ trajectory. The energy seen by each block was then digitized. The energy of the γ was first randomized within a gaussian distribution with a width which would ultimately give the same π° mass width as the data. Next the randomized energy was divided between the FW and the MA. The fraction of energy deposited in the FW was energy dependant. The energy dependence was estimated by examining the e^+e^- calibration data, and by using a Monte Carlo called EGS[23] which makes detailed models of electromagnetic showers. Details of the process can be found in Ref. 15. The transverse spread of the shower in both the MA and FW was simulated by two overlapping gaussian distributions to give the non-gaussian tails observed for real showers. More than 90% of the shower energy is within an area of radius $r_M = 21\ \text{MeV} \cdot L_R / E_\gamma$ [24], where L_R is the radiation length. One narrow gaussian contained a large fraction of the energy, and the second, wider gaussian had the rest. The fractions of energy and the widths of these gaussians for the FW and MA

showers were adjusted to match the number of blocks per γ shower observed from reconstructed Ξ^0's, shown in Fig. 3.09. For FW showers, 93.5% of the energy went to a gaussian of width 0.7 cm and the remainder to a gaussian of width 9.3 cm. The MA energy was divided 87.5% to 12.5% to gaussians of widths 2.6 cm and 9.5 cm.

The $\Lambda \rightarrow p\pi^-$ two body decay was carried through in the same manner as the $\Xi^0 \rightarrow \Lambda\pi^0$ decay. The p and π^- were tracked through the spectrometer, and the coordinates of the charged particle positions at each chamber were calculated. The charged particles were sent on circular arcs through the B_y bending field of the analysis magnets, and were given a deflection at each fringe field.

The Monte Carlo events were required to pass the trigger described in section 2.30, including a minimum deposited γ energy to mock the lead glass part of the trigger. An event which passed the trigger was given digitized wire hits and digitized lead glass pulse heights to make it appear as data. The Monte Carlo events were passed through the same analysis process as the data, including determination of the Ξ^0 beam offsets and the π^0 bootstrap calibration.

All of the figures in this chapter of overlayed points and line histograms show comparisons between reconstructed $\Xi^0 \rightarrow \Lambda\pi^0$ decays from the data (points) and from the Monte Carlo (line).

Chapter 4

Analysis II

4.00 Introduction

The 6.7×10^5 1 γ plus Λ events provided the data base in which to search for $\Xi^\circ \rightarrow \Lambda\gamma$ decays. Three prevalent types of background decays had a Λ and γ detected in the apparatus: a beam Λ plus an unassociated γ, $\Sigma^\circ \rightarrow \Lambda\gamma$ decays, and $\Xi^\circ \rightarrow \Lambda\pi^\circ$ decays where one γ missed the lead glass array. Other possible event types besides these three were less prevalent, such as Σ^* excited states, and will be disscussed later. With the resolution of this spectrometer, beam Λ's and Σ° decays can not reconstruct to a high enough mass region to be background for $\Xi^\circ \rightarrow \Lambda\gamma$ decays. The relevant background consisted almost entirely of $\Xi^\circ \rightarrow \Lambda\pi^\circ$ decays, where only one γ was detected. Ξ° decays of this type will be refered to as background Ξ°'s, for both data and Monte Carlo. Signal Ξ°'s are, of course, $\Xi^\circ \rightarrow \Lambda\gamma$ decays.

When the Λ–γ invariant mass is calculated, a good proportion of background $\Xi^\circ \rightarrow \Lambda\pi^\circ$ decays do not come close to the correct Ξ° mass, 1.3149 GeV, because the missing γ removes too much of the total energy in the decay. Sometimes, however, the π° decayed and sent one γ almost directly forward in the direction of the π° momentum. That one γ then took almost all the initial laboratory energy of the π°, and the other γ had very little energy. When the event was reconstructed as a Λ–γ, it was almost as good as reconstructing the Λ–π°; and the resulting mass of backround Ξ° tailed out into the region occupied by real $\Xi^\circ \rightarrow \Lambda\gamma$ decays. The whole problem in the analysis was to reduce the $\Xi^\circ \rightarrow \Lambda\pi^\circ$ decay

background by the highest possible factors without destroying any possible $\Xi^\circ \rightarrow \Lambda\gamma$ signal. The solution to the problem relies on a detailed Monte Carlo simulation of the two Ξ° decay channels in the apparatus.

The Monte Carlo programs for both $\Xi^\circ \rightarrow \Lambda\pi^\circ$ and $\Xi^\circ \rightarrow \Lambda\gamma$ decays were very important in determining the best means for background reduction. Since no signal appears until the background has been reduced by a factor of about 300, only the $\Xi^\circ \rightarrow \Lambda\gamma$ signal Monte Carlo gives information of the effects on the signal from background reduction. The signal, as will be shown, lies on the tail of misreconstructed $\Xi^\circ \rightarrow \Lambda\pi^\circ$ decays; a good Monte Carlo was necessary so that the shape of the tail was well understood.

4.10 Preliminary Background Reduction

Some simple cuts could be applied which reduced the backgrounds and had essentially no effects on the signal. Other cuts were made which had approximately equal effect on both signal and background, but had to be done anyway to insure a clean sample of data with all parameters well measured. Table 4.1 reviews all the preliminary cuts discussed in this section. In all the cited figures, the plot of points overlayed with a solid line compares the data with the background Monte Carlo (solid line). The plot of overlayed histograms compares the signal Monte Carlo (dashed line) to the background Monte Carlo (solid line). The background Monte Carlo in the comparisons to the data has been normalized absolutely, to the number of Ξ°'s expected to be present based upon the 2-γ Ξ° acceptances. Details of the normalization will be covered in Sec. 5.10. The two overlayed Monte Carlos in the other comparison plots have each been normalized to the same arbitrary number of events.

The Λ in the 1-γ data sample had the same conditions imposed upon it as the 2γ data sample. The Λ was put through the same geometric and kinematic fit as described in Sections 3.10 to 3.12.; and the same requirements on χ^2_k-χ^2_g and on the Λ decay vertex position were applied.

Like the 2-γ sample, a minimum energy per cluster was applied to even out TDC threshold imbalances. The energy cut made on the 1 γ data was 12 GeV per cluster, rather than 6. The aim was to

minimize any differences in glass trigger inefficiencies between the two data sets, and make the minimum energy deposited equal. The same TDC matching and timing requirements were made on the 1-γ as on the 2-γ data samples. Fig. 4.01 a & b shows the energy distribution of the single detected γ before the γ cuts have been applied. The arrows indicate where the energy cut is located.

Next a cut on the γ position at the lead glass array was made, requiring it to be within a fiducial volume. The cut had to be made fairly restrictive, in order to reduce the high rates of accidental gammas seen by the glass blocks next to the neutral beam hole. The fiducial volume lay 5.6 cm inside all outer edges, which is 1/2 a block width plus 1/2 cm; and was 5.6 cm around the hole. About 40% of the data events were outside the fiducial volume, and the cut had the same effect on backround Ξ° as on the signal Monte Carlo, where 30% of the events were cut.

The two following cuts had little effect on the signal, but substantially reduced the amount of data. The first was on the transverse momentum of the Λ with respect to the beam centroid. The Λ p_t distributions for beam and daughter Λ's are quite different. Beam Λ's, since they define the beam centroid, have a very small transverse momentum with respect to it. The Λ p_t also differs between daughter Λ's originating from different decays. The value of the mean in the p_t distribution for daughter Λ's scales with the total center of mass momentum available to that Λ in a two body decay. The three decays $\Sigma^\circ \rightarrow \Lambda\gamma$, $\Xi^\circ \rightarrow \Lambda\pi^\circ$, and $\Xi^\circ \rightarrow \Lambda\gamma$ each have a characteristic center of mass momentum of 74 MeV, 135 MeV and 184 Mev respectively. Fig 4.02a shows the Λ p_t for beam Λ's, Fig. 4.02 b & c overlays the Λ–γ data and signal Monte Carlo with the background Monte Carlo decays, before the cut was made. Note that the data has some beam Λ contamination. The Λ p_t distribution for $\Sigma^\circ \rightarrow \Lambda\gamma$ decays lies within the same region as beam Λ's. The arrow indicates where the cut was located, eliminating events with Λ $p_t < 0.11$ GeV.

The next preliminary cut was on the Λ–γ invariant mass. To calculate the mass a decay vertex for the parent is needed. For the 2-γ $\Xi^\circ \rightarrow \Lambda\pi^\circ$ decays, the vertex came out of the kinematic fit, where the mass of the parent was constrained. In the 1-γ sample, one does not want to force any assumption about the mass of the parent. For either $\Xi^\circ \rightarrow \Lambda\pi^\circ$ or $\Xi^\circ \rightarrow \Lambda\gamma$ decays, the Λ momentum vector must point back

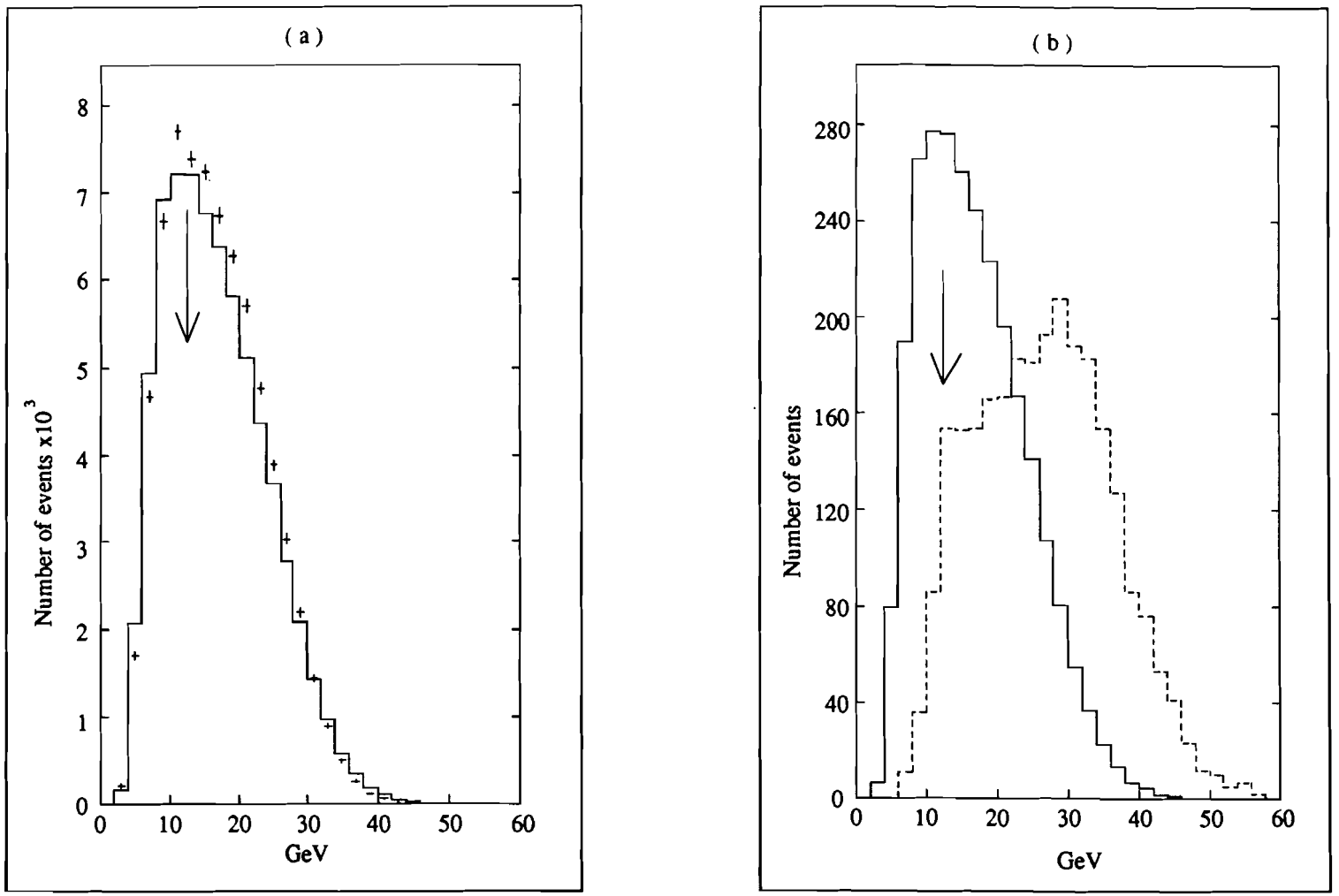

Fig. 4.01 : Distribution of γ energies for the background Monte Carlo (solid line) compared to (a) the data and (b) the signal Monte Carlo The arrows show where the energy cut was made, removing events with γ energy less than 12 GeV.

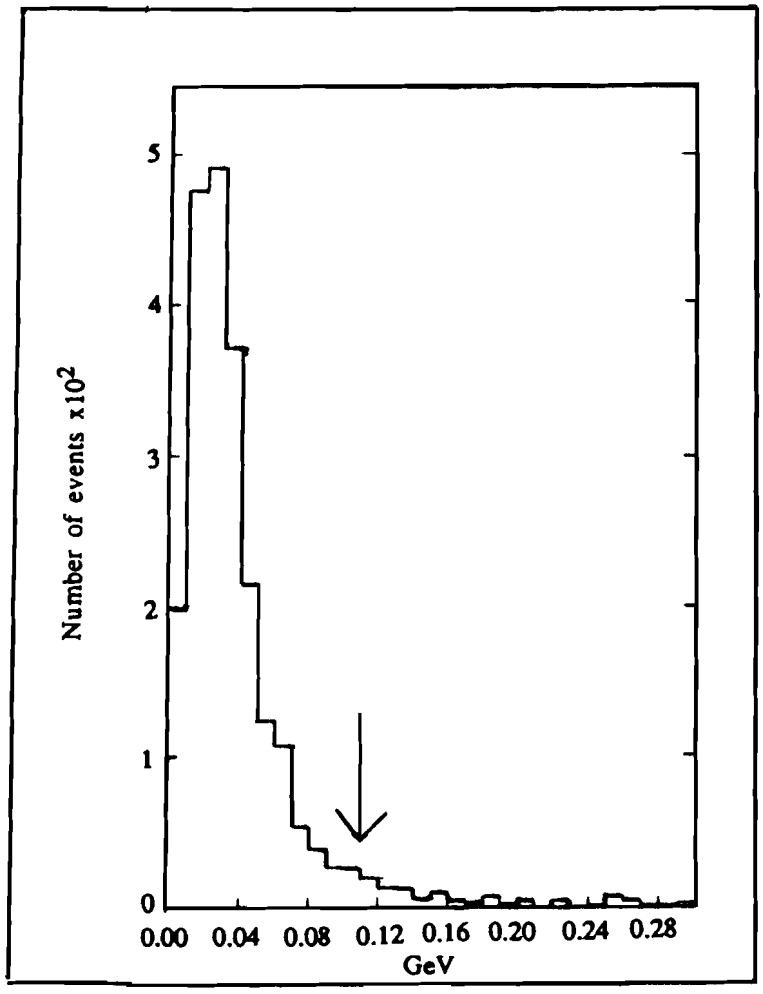

Fig. 4.02a : Transverse momentum, p_t, with respect to the beam centroid for beam Λ's. The arrow shows where the cut was applied, removing events with $p_t \leq 0.11$ GeV. The tail of this distribution, events with $p_t > 0.08$, are for the most part $\Xi^\circ \rightarrow \Lambda\pi^\circ$ decays where neither of the γ's hit the lead glass.

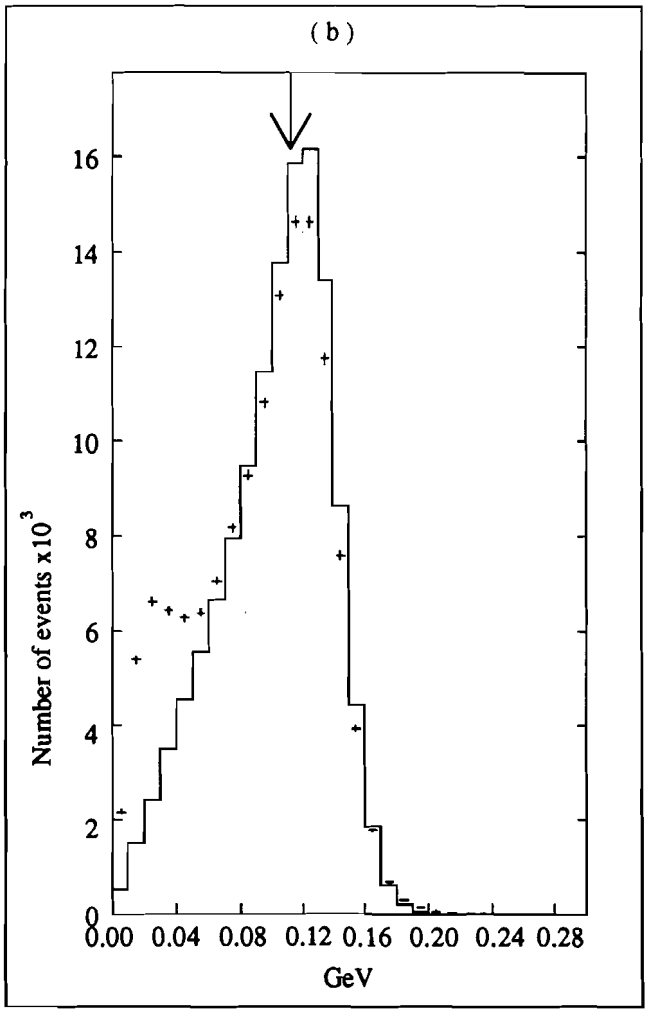

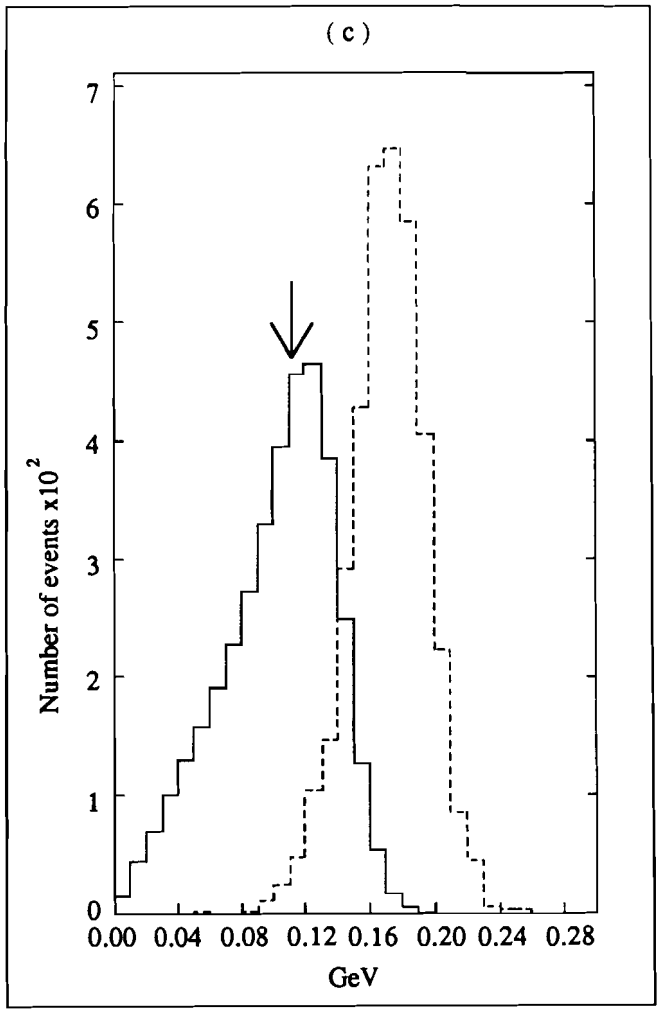

Fig. 4.02 b & c : Transverse momentum, p_t, of the Λ with respect to the beam centroid, for background Monte Carlo (solid line) compared to (b) the data, and (c) the signal Monte Carlo The arrows show where the cut was made. Note the contamination of beam Λ's in the data.

to the vertex, and the parent must lie in the neutral beam if it came from the production target. The parent decay vertex was taken to be the point of closest approach between the daughter Λ vector and the beam centroid as determined by the offsets described in section 3.13. The point of closest approach, Fig. 4.03 a & b, was a good approximation of the Ξ° decay vertex that comes out of the Ξ° kinematic fit when both γ's were detected. The z position of this vertex was required to be > 0.5 m, and less than the Λ vertex z position.

The γ momentum vector was calculated from the vertex position described above and from the shower position in the lead glass. The γ vector was used with the Λ vector to reconstruct a parent momentum vector and mass. No assumptions were made concerning the origin of the parent, for example forcing it to come from the production target. The Λ–γ mass spectrum for the data compared to the background Monte Carlo is shown in Fig. 4.04. Only Λ–γ events with an invariant mass > 1.24 GeV were retained for futher analysis, shown by the arrow. The Monte Carlo $\Xi^\circ \rightarrow \Lambda\gamma$ decays had a width of about 20-25 MeV, and the cut left plenty of width around the correct mass value.

The final preliminary cut was made on the Θ_x and Θ_y Ξ° divergence distributions. Once a Λ–γ parent mass and momentum vector was obtained, a divergence with respect to the beam centroid could be calculated. Figs. 4.05 and 4.06 a & b show the distribution comparisons, and arrows where the cut was made. Note that the misreconstructed Ξ° background shows a wider divergence than the correctly reconstructed signal Monte Carlo. The same cut was applied here as for the 2-γ data sample, requiring $\Theta_{x,y}$ to be between $\pm$0.3 mrad.

Table 4.1 shows each of the data cuts discussed so far, and the reduction factors on the data, and both monte carlos. The cuts in the table are cumulativly applied; the fraction passing each cut is the fraction of events surviving the previous cut. In addition the Λ and γ reconstruction efficiency from the Monte Carlo's is included at the top of their columns; these fractions along with the cuts applied become the analysis acceptances used in the branching ratio calculation. Figs. 4.08 to 4.11 show various kinematic variables after the preliminary cuts.

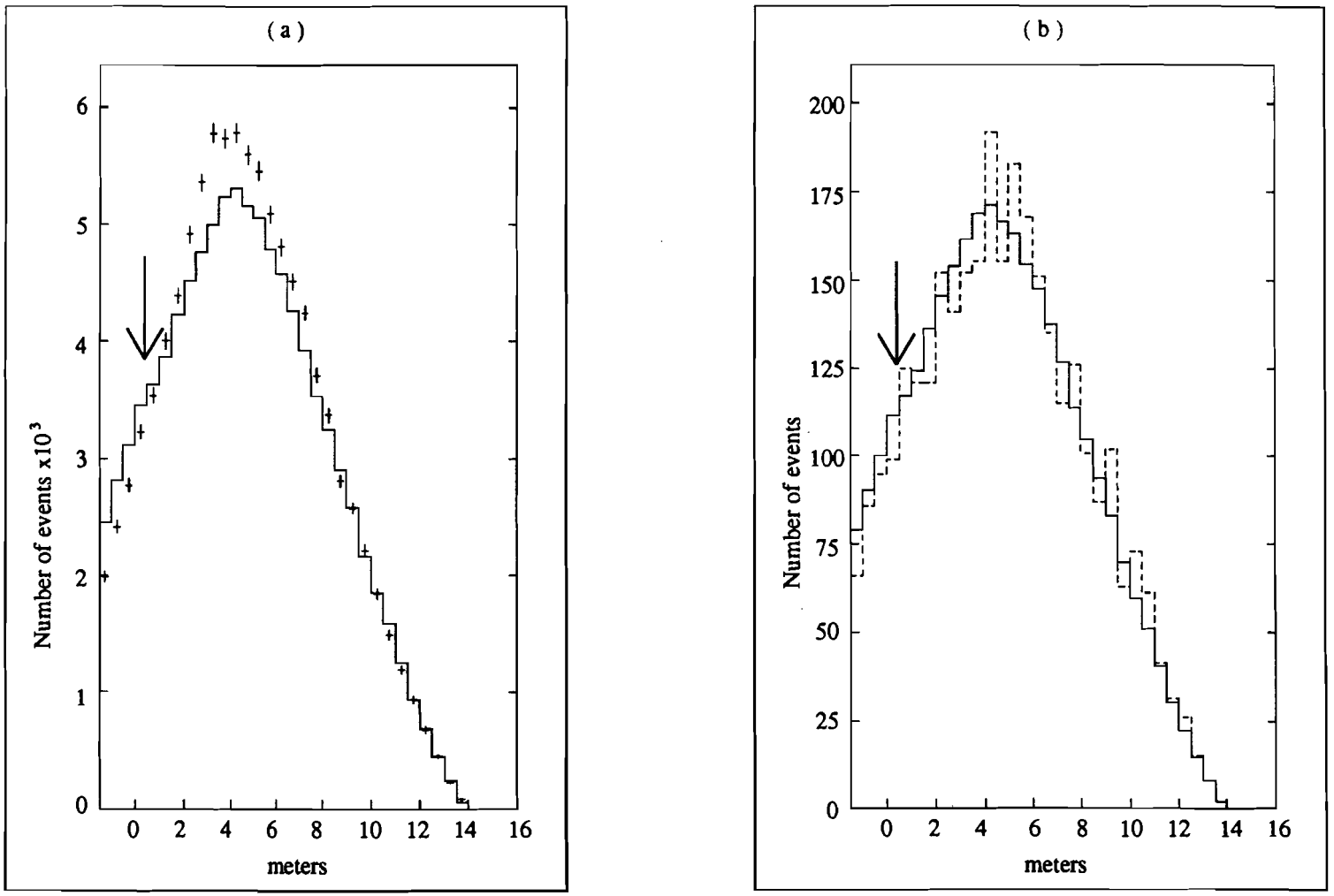

Fig. 4.03 : The position along the z axis of the closest approach of the Λ vector to the beam centroid, used as a decay vertex for the parent Λ–γ decay. The background Monte Carlo (solid line) is compared to (a) the data and (b) the signal Monte Carlo.

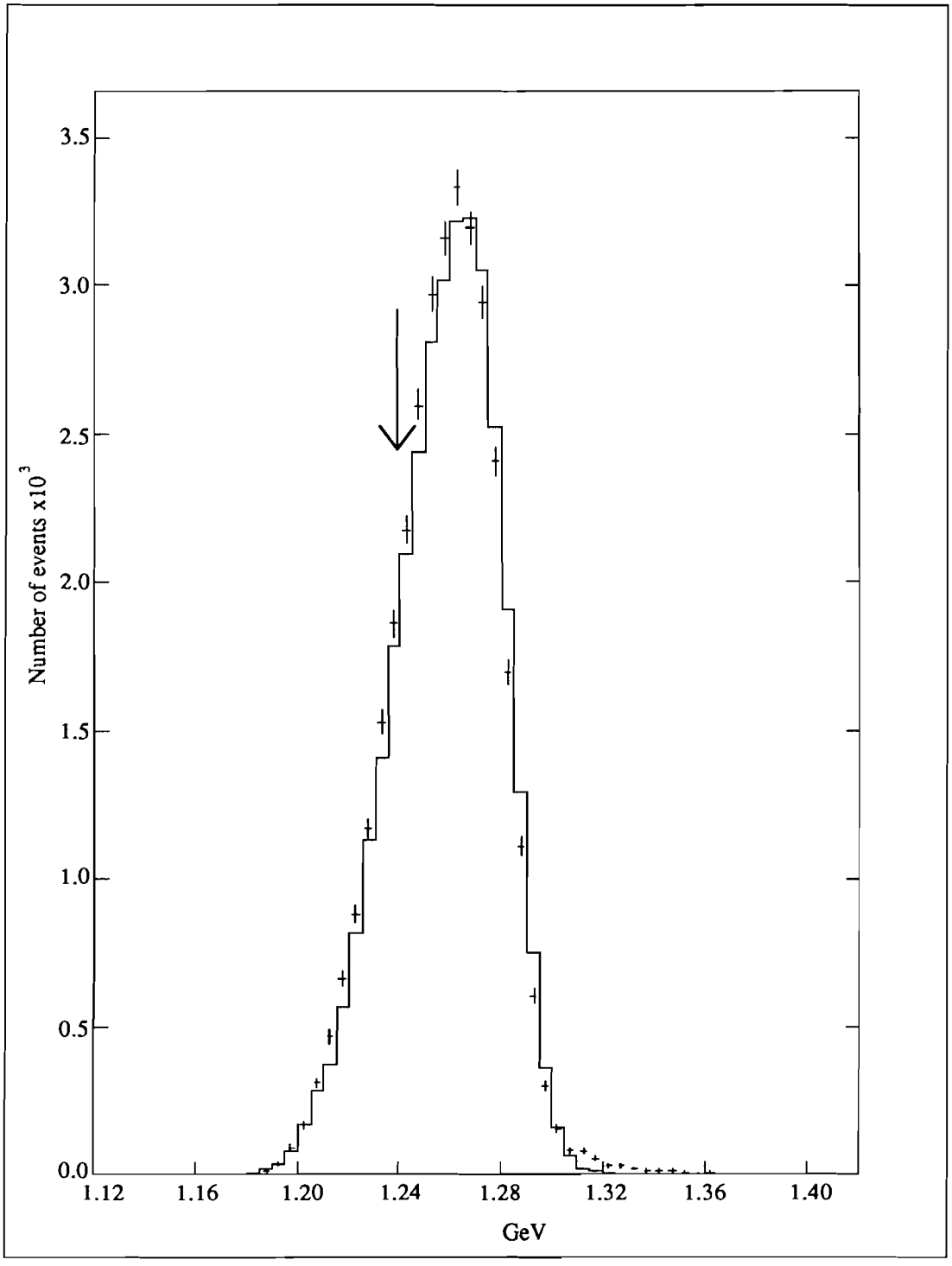

Fig. 4.04 : The $\Lambda-\gamma$ parent mass spectrum, comparing background Monte Carlo (solid line) to data. The cut eliminated events <1.24 GeV, shown by the arrow.

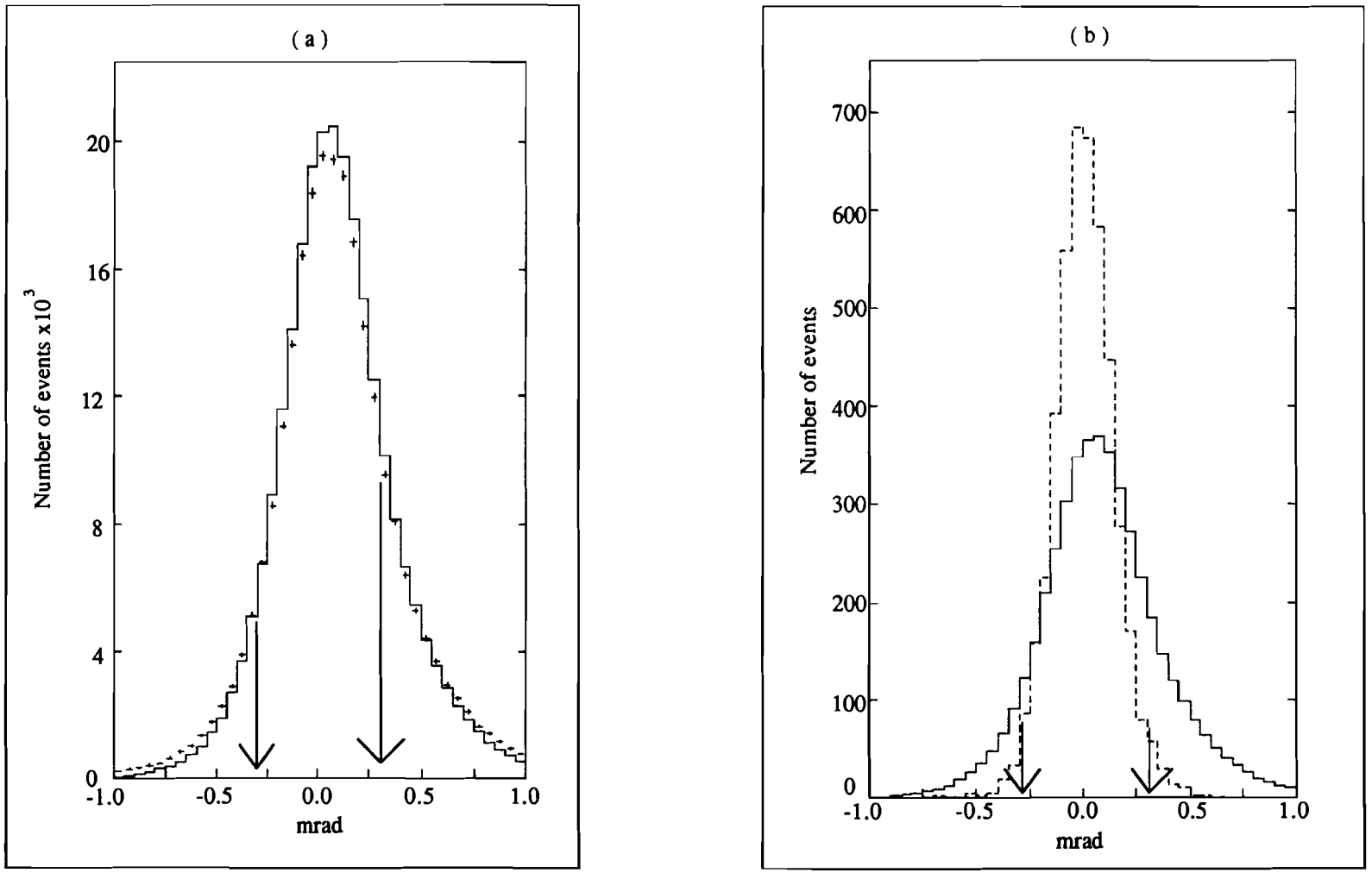

Fig. 4.05 : The divergence Θ_x of the reconstructed $\Lambda-\gamma$ parent from the beam centroid. The background Monte Carlo (solid line) is compared to (a) the data and (b) the signal Monte Carlo. The arrows show where the cut was made.

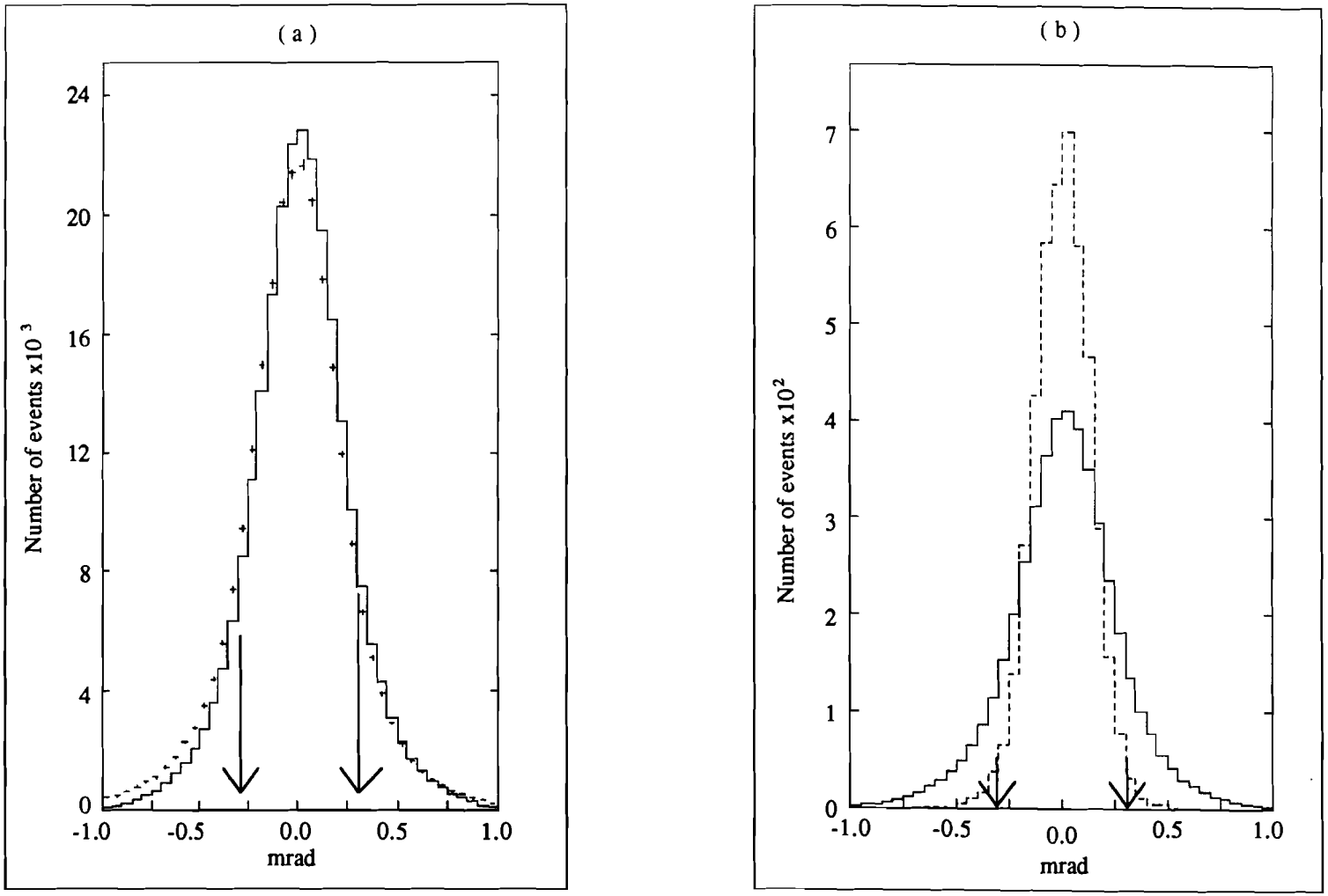

Fig. 4.06 : The divergence Θ_y, of the reconstructed $\Lambda-\gamma$ parent from the beam centroid, for background Monte Carlo (solid line) compared to (a) data and (b) signal Monte Carlo. The arrows show where the cut was located.

Table 4.1

$\Lambda-\gamma$ sample preliminary analysis cuts

cut requirements	fraction of data passing	fraction of background MC passing	fraction of signal MC passing
MC Λ reconstruction efficiency		0.782	0.787
MC γ reconstruction efficiency		0.961	0.987
Λ inside decay volume limits	0.982	0.997	0.997
$\chi^2_k - \chi^2_g < 10$	0.884	0.910	0.911
TDC matched with event	0.84	----	-----
γ inside glass fiducial volume	0.62	0.71	0.70
-0.3 mrad $< \Theta_{x,y} <$ 0.3 mrad	0.54	0.51	0.82
0.5m $< z_{close} <$ z Λ vertex	0.52	0.54	0.72
energy $\gamma > 12$ GeV	0.71	0.69	0.95
γ in time with trigger	0.98	----	-----
0.11 GeV $< \Lambda\ p_t <$ 0.23 GeV	0.68	0.70	0.99
$\Lambda-\gamma$ mass > 1.24 GeV	0.79	0.80	1.00
combined effect of preliminary cuts	0.0475	0.0686	0.353
$\Xi^\circ \rightarrow \Lambda\gamma$ Monte Carlo analysis acceptance before final cuts			0.274

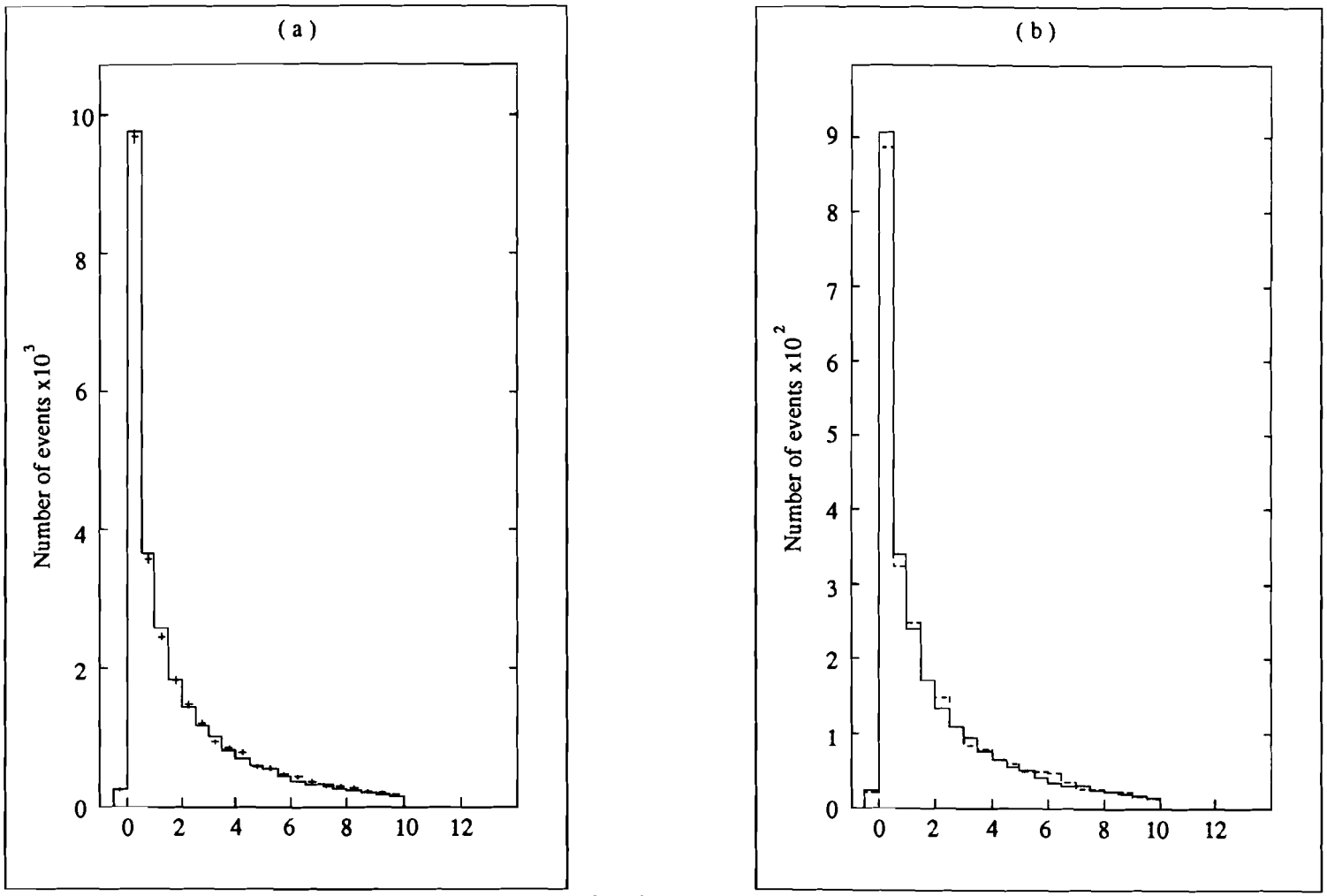

Fig. 4.07 : The difference between the two Λ chi-squares, $\chi^2_k - \chi^2_g$, for background Monte Carlo (solid line) compared to (a) data and (b) signal Monte Carlo, after the preliminary cuts have been applied.

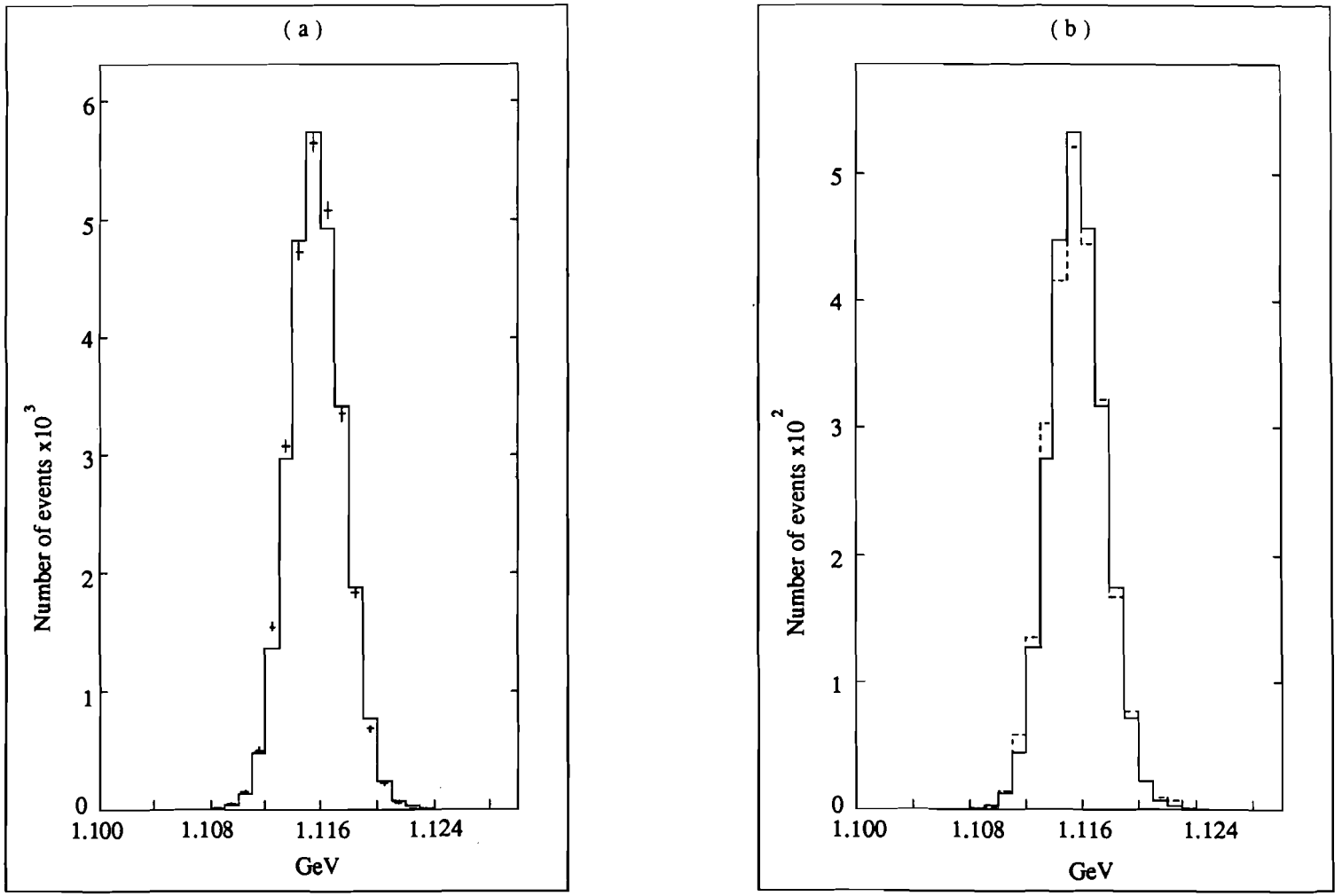

Fig. 4.08 : Λ mass distribution for background Monte Carlo (solid line) compared to (a) data and (b) signal Monte Carlo after the preliminary cuts have been applied.

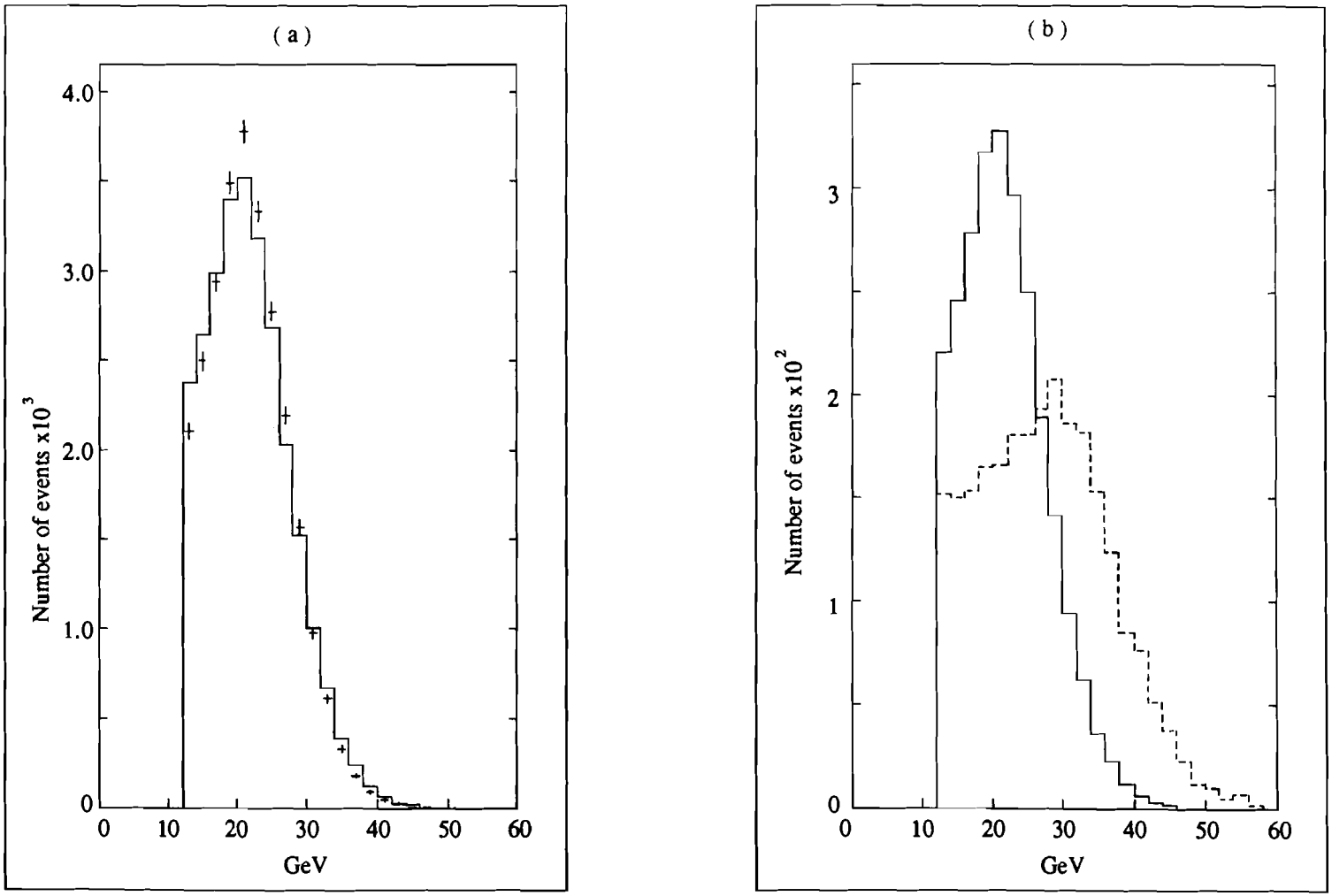

Fig. 4.09 : The γ energy distribution for background Monte Carlo (solid line) compared to (a) data and (b) signal Monte Carlo after the preliminary cuts have been applied.

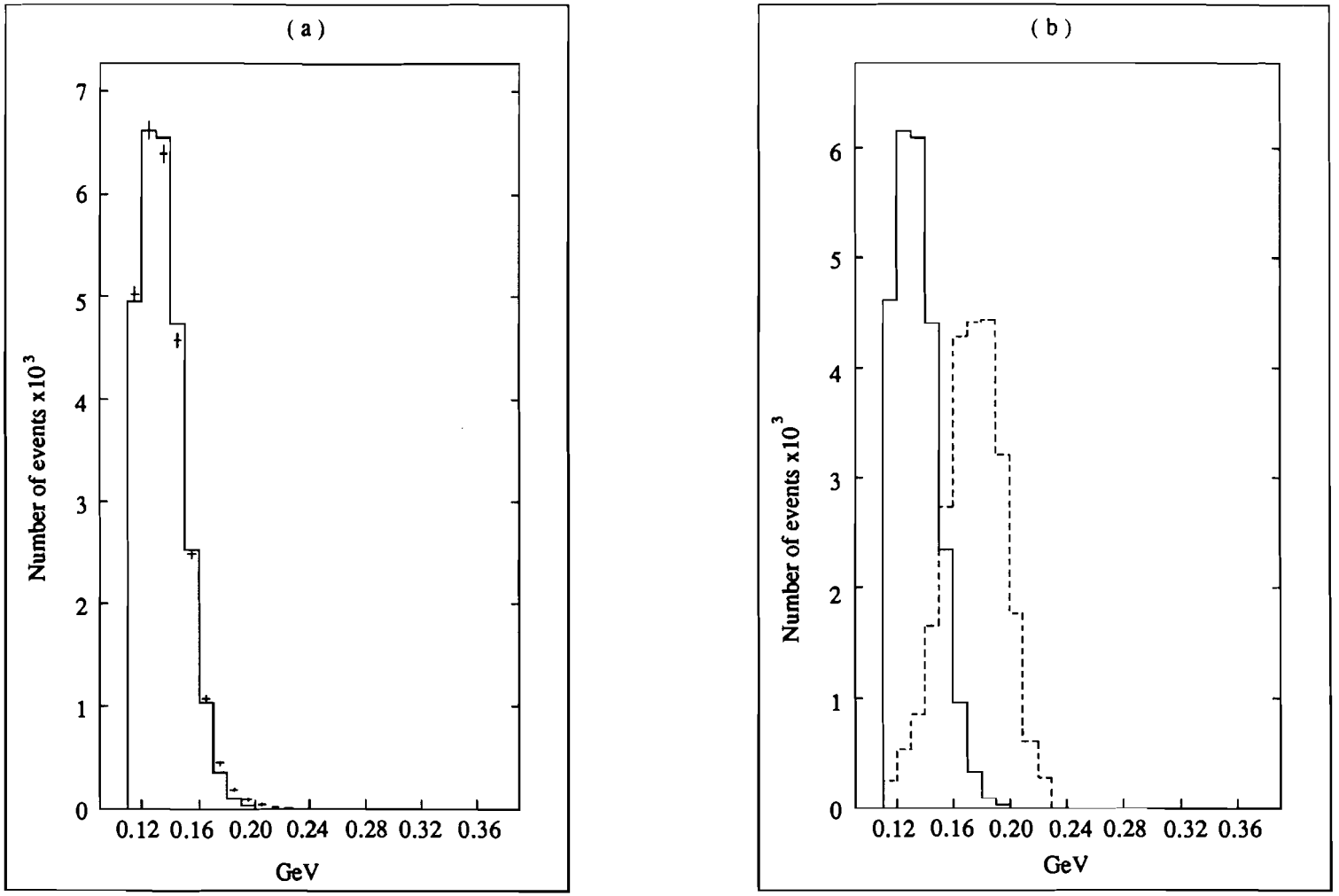

Fig. 4.10 : The Λ p_t distribution for background Monte Carlo (solid line) compared to (a) data and (b) signal Monte Carlo after the preliminary cuts have been applied.

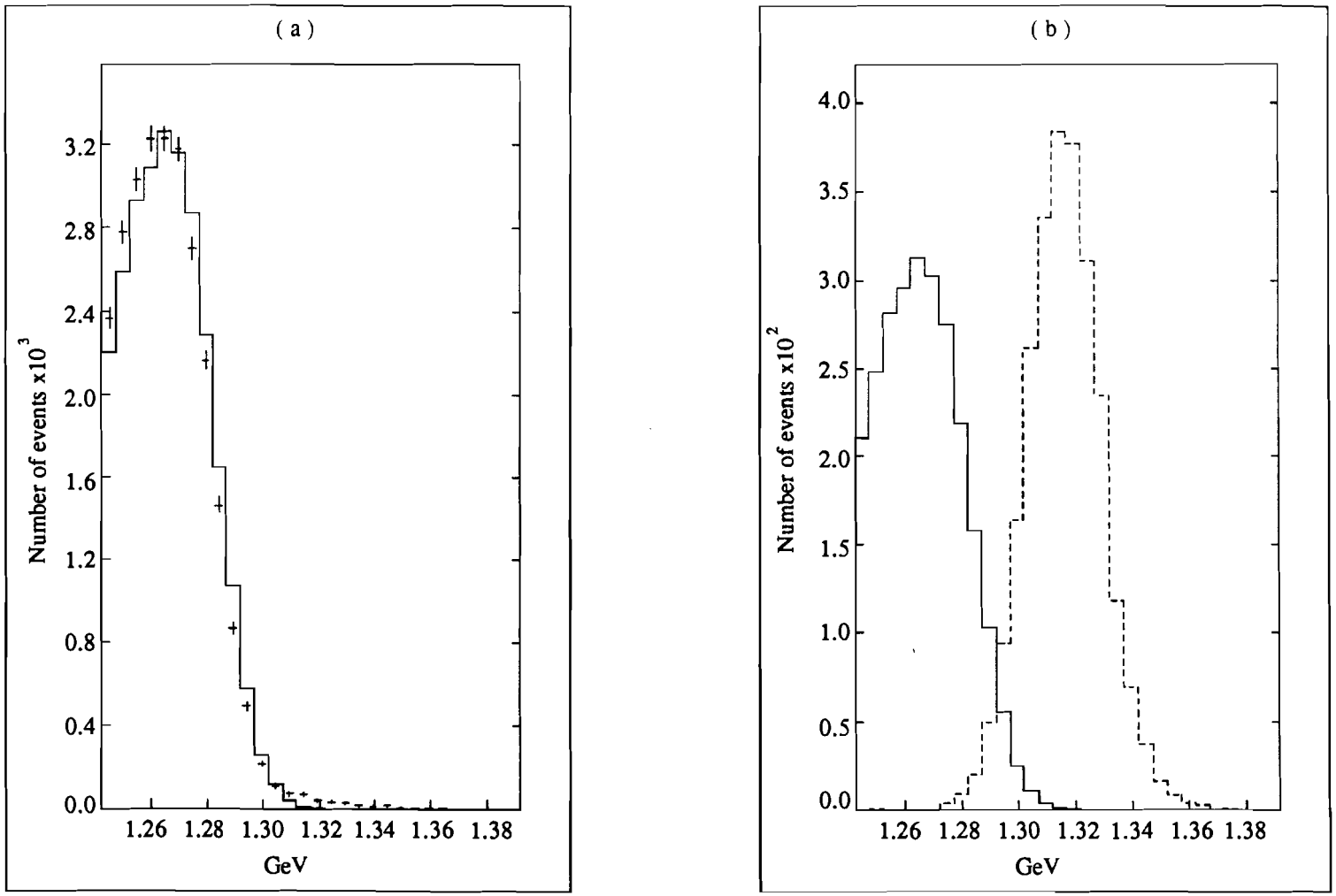

Fig. 4.11 : Λ–γ mass distribution for background Monte Carlo (solid line) compared to (a) data and (b) signal Monte Carlo after the preliminary cuts have been applied.

4.20 Separation of signal from background

After this point in the analysis, the Monte Carlo events were studied for ways to further reduce background. The preliminary cuts had reduced the signal Monte Carlo by a factor of about 2.8 compared to factor of 15 in reduction of the background Monte Carlo. Much background had been eliminated, but the background that was left had much in common with signal events, making it harder to get rid of without destroying whatever signal may be there. The $\Lambda-\gamma$ mass, Fig. 4.11, does not yet show any evidence of $\Xi^\circ\rightarrow\Lambda\gamma$ decays. Each of the following cuts will be discussed separately, and Table 4.2 gives the reductions as each set of cuts was progressively applied. One of the cuts was based upon kinematic variables directly measured in the laboratory. The other cuts stemmed from the version of the Ξ° kinematic fitting program which reconstructed $\Lambda-\gamma$ events to the assumed background decay hypothesis, $\Xi^\circ\rightarrow\Lambda\pi^\circ$ decays where one γ missed the lead glass. Another fitting program tested the decay $X\rightarrow\Lambda\gamma$ for coplanarity of the decay products and target pointing accuracy of the reconstructed X parent; the mass of X was not constrained. Information from the coplanarity test showed that the data left after other cuts were consistent with such two-body decays.

4.21 Λ p_t vs E_γ

The Λ p_t distributions for $\Xi^\circ\rightarrow\Lambda\pi^\circ$ and $\Xi^\circ\rightarrow\Lambda\gamma$ decays, shown in Fig 4.10, are somewhat separated, but overlap too much to be able to make a restrictive cut based solely on p_t. A loose Λ p_t cut was described in section 4.10. The distribution of the detected γ energy, E_γ, is shown in Fig 4.09 for the two decay types. There is even more overlap in the E_γ distributions. If the two variables are plotted against one another, however, the areas occupied by the decay types are separated more than in the one-dimensional distributions. Fig. 4.12 shows two-dimensional plots of Λ p_t vs E_γ for both Monte Carlo decay types. A two dimensional cut can be made which cuts out the area occupied by most background $\Xi^\circ\rightarrow\Lambda\pi^\circ$ decays. The two-dimensional cut ultimately used removed any event with Λ $p_t <$ .16 GeV and $E_\gamma <$ 30 GeV, and is indicated by the shaded tops of the bars in the plots. The cut by itself removed about 5% of signal Monte Carlo events and 43% of the background.

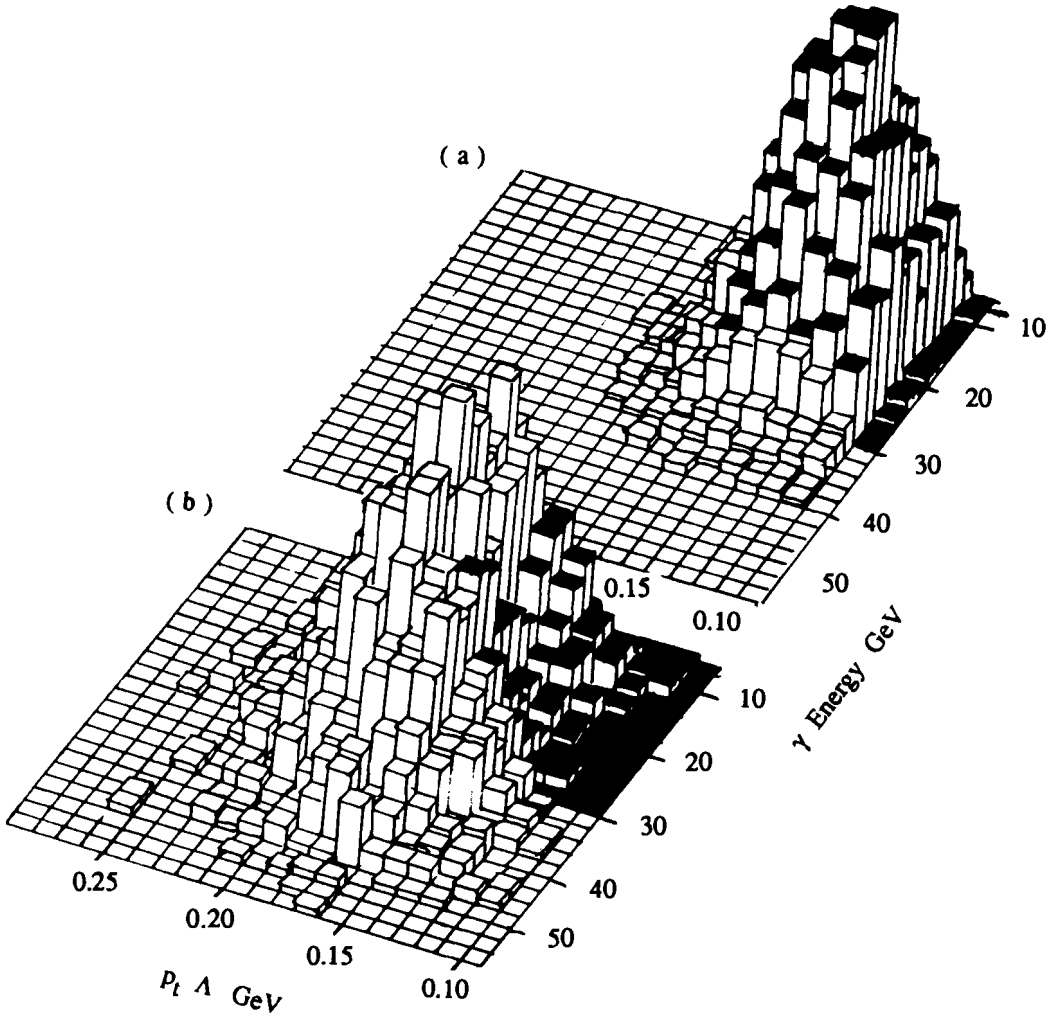

Fig. 4.12 : Scatterplots of Λ p_t vs energy of the γ. (a) is the background Monte Carlo, and (b) is the signal Monte Carlo. The shaded area shows where the cut was located, removing events with p_t<0.16 GeV and Eγ<30 GeV. Only preliminary cuts have been applied.

4.22 1-γ $\Xi^\circ \rightarrow \Lambda\pi^\circ$ kinematic fit

The $\Xi^\circ \rightarrow \Lambda\pi^\circ$ kinematic fit could be used in three modes. Two have already been discussed in section 3.4, the π° bootstrap, and the 2-γ kinematic fit where all the decay products have been detected. The third mode is when only one γ has been detected, and the energy and position of the second γ were unknown. The method attempts to find a second γ which will fit the decay chain, $\pi^\circ \rightarrow \gamma\gamma$, $\Xi^\circ \rightarrow \Lambda\pi^\circ$. The process will be referred to as the 1-γ Ξ° kinematic fit.

All of the same information on the detected decay products was given to the 1-γ fit as to the 2-γ fit, except of course that one γ was missing. The same constraint that the reconstructed Ξ° come from the target was applied. In order to have enough constraints, however,to solve the equations involved, the Ξ° decay point could no longer be treated as an unknown as it was in the 2-γ mode. The Ξ° decay point was determined by the closest approach of the Λ to the beamline, disscussed previously, and fixed there as a measured quantity. The measurement resolution on the undetected γ was made 3 orders of magnitude larger than the resolution of the measured value, so that the energy could be varied to any value allowed within the kinematics without significantly increasing χ^2_Ξ. The γ position was not a constraint, and was not required to be located off the glass array. Since the contribution to the mass resolution now comes from only one γ, the widths of the π° and Ξ° masses are narrower than for the 2-γ sample.

The 1-γ Ξ° kinematic fit was tested on the 1-γ Ξ° background Monte Carlo. The program was able to find an acceptable fit for 94% of the background and 88% of the signal Monte Carlos. The mass distributions of the $\Xi^\circ \rightarrow \Lambda\pi^\circ$ backround and $\Xi^\circ \rightarrow \Lambda\gamma$ Monte Carlo events reconstructed through the 1-γ Ξ° kinematic fit, shown in Fig. 4.13, were calculated using the momentum and energy of the fitted missing γ, and the measured momenta of the detected γ and of the Λ. Events that were $\Xi^\circ \rightarrow \Lambda\pi^\circ$ decays to start with were recovered and reconstructed to the correct Ξ° mass. Those $\Xi^\circ \rightarrow \Lambda\gamma$ events which were reconstructed gave a mass higher than the true Ξ° mass, and the distribution was wider. When a 'missing γ' could be found for $\Xi^\circ \rightarrow \Lambda\gamma$ decays; it added too much total energy and momentum, and the resulting parent mass was too high. Clearly, a powerful cut on the background events could be made here by cutting on this reconstructed Λ–π° mass.

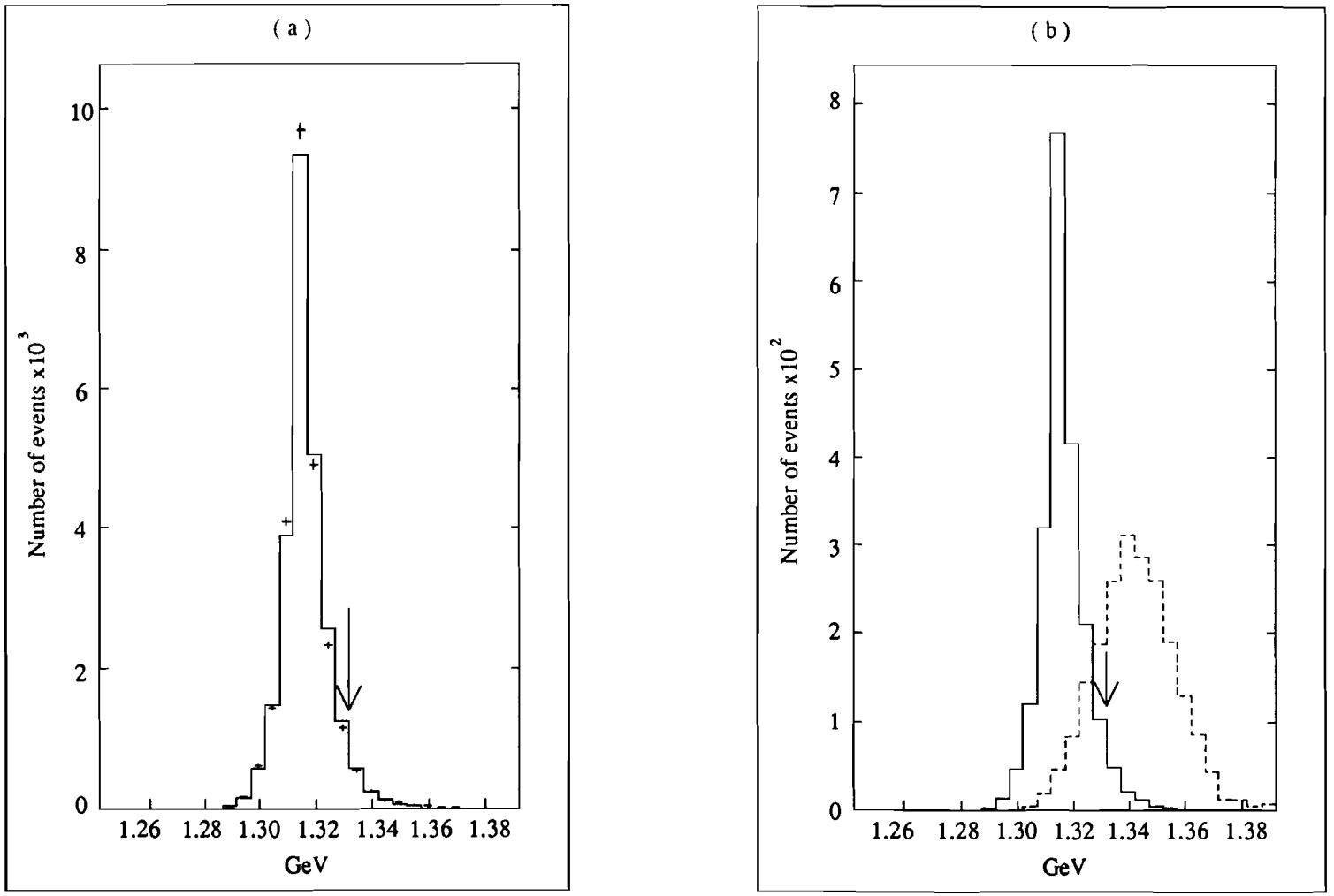

Fig. 4.13 : The Λ–π° mass from the 1-γ fit, described in section 4.22. The background Monte Carlo (solid line) is compared to (a) the data and (b) the signal Monte Carlo, after the preliminary cuts have been applied. The arrows show where the $\Xi^\circ \rightarrow \Lambda\pi^\circ$ mass cut was applied.

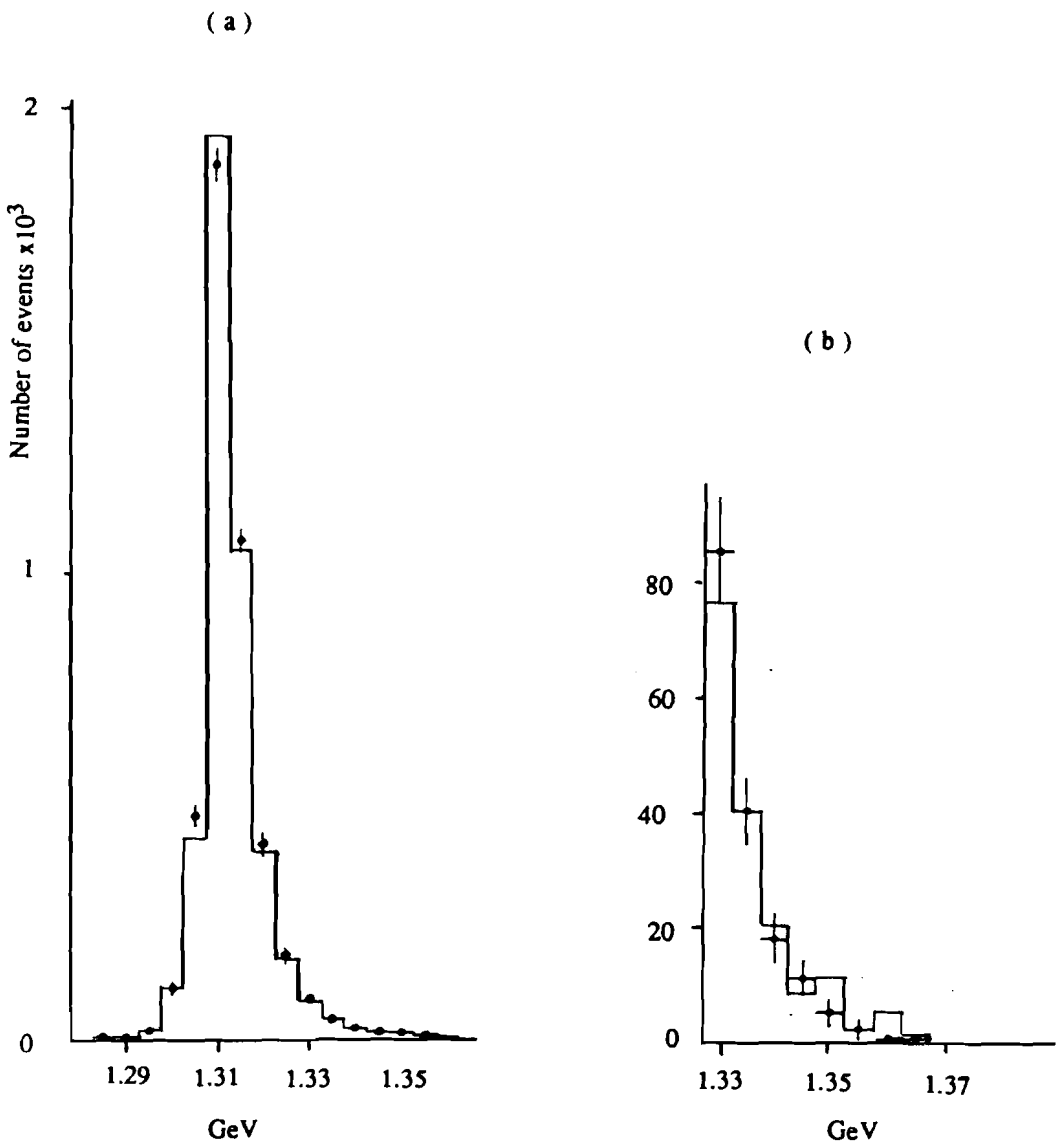

Fig. 4.14 : A test of the 1-γ $\Xi^\circ \rightarrow \Lambda\pi^\circ$ fit using the 2-γ data. The low energy γ was dropped in both the data (points) and the 2-γ Ξ° Monte Carlo (solid line), and the events were passed to the 1-γ fit. The Λ–π° mass is shown here in (a); (b) is an expansion of the scale to show the tail of the mass distribytion that would be left after a 3-σ cut.

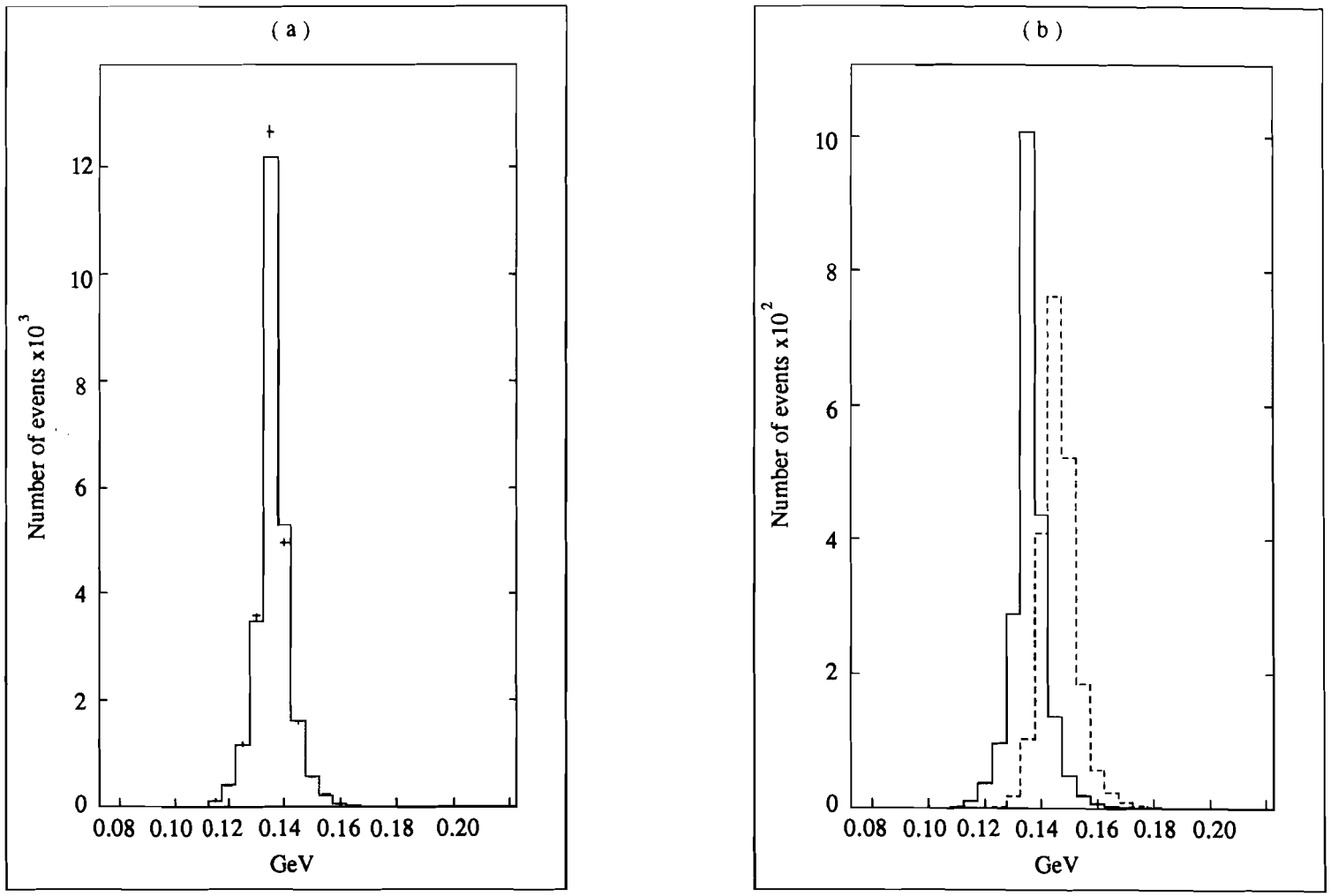

Fig. 4.15 : The π°mass from the 1-γ Ξ° fit, described in section 4.22. The background Monte Carlo (solid line) is compared to (a) the data and (b) the signal Monte Carlo, after the preliminary cuts have been applied.

The ability of the 1-$\gamma\,\Xi^\circ$ kinematic fit to recover true $\Lambda-\pi^\circ$ decays was also tested using 2-γ data and 2-$\gamma\,\Xi^\circ\rightarrow\Lambda\pi^\circ$ Monte Carlo events. This was also a test of the ability of the Monte Carlo to simulate the behavior of the data. Fully reconstructed and well identified 2-$\gamma\,\Xi^\circ\rightarrow\Lambda\pi^\circ$ decays, from both the data and Monte Carlo, had the lower energy γ dropped. All events were sent through the 1-$\gamma\,\Xi^\circ$ fit. The results are shown in Fig 4.14a which compares 2-γ data to the 2-$\gamma\,\Xi^\circ$ Monte Carlo. The Ξ° mass plot shows that the 1-γ fit really reconstructed $\Xi^\circ\rightarrow\Lambda\pi^\circ$ decays to the correct mass. Since a cut on this Ξ° mass was made, it was important to get the high mass tail of the distribution well-matched with the Monte Carlo. Fig 4.14b shows the area of the tail, on an expanded scale, left after the mass cut made in the 1 γ data sample, which remains as background. Figs. 4.15 through 4.17 show comparisons of the π° mass, the missing γ energy and the χ^2_Ξ, all from the 1-γ data, background and signal Monte Carlos reconstructed under the 1-$\gamma\,\Xi^\circ$ kinematic fit.

The fact that the $\Xi^\circ\rightarrow\Lambda\gamma$ decays do not reconstruct well as $\Xi^\circ\rightarrow\Lambda\pi^\circ$ decays also shows up in the χ^2_Ξ distribution for the 1-$\gamma\,\Xi^\circ$ kinematic fit. Fig. 4.17 shows the χ^2_Ξ for the background and signal Monte Carlo events. A cut was made requiring first that events passed the 1-$\gamma\,\Xi^\circ$ fit, and then have a value of $\chi^2_\Xi > 12$. These requirements reduced the background Monte Carlo by 93%, the data by 94%, and the signal Monte Carlo by 26%.

Fig. 4.18 shows two-dimensional plots of the mass distributions for the background and signal Monte Carlos. One axis is Fig. 4.13, the $\Lambda-\pi^\circ$ mass using the reconstructed missing γ from the 1-$\gamma\,\Xi^\circ$ fit. The other axis is the $\Lambda-\gamma$ mass from Fig. 4.11. The background events give a good Ξ° mass under the $\Xi^\circ\rightarrow\Lambda\pi^\circ$ hypothesis, but not as $\Xi^\circ\rightarrow\Lambda\gamma$ decays. The reverse was true for the $\Xi^\circ\rightarrow\Lambda\gamma$ Monte Carlo events; they give a good Ξ° mass assuming a $\Lambda-\gamma$ decay, but not assuming a $\Lambda-\pi^\circ$ decay. The $\Lambda-\pi^\circ$ mass cut used in the analysis was made at 3σ around the background mass peak in Fig. 4.13, and removed any events in the data sample with $\Lambda-\pi^\circ$ mass < 1.332 GeV. The two dimensional plots show the mapping between the two mass reconstructions. The area cut is shaded. The $\Lambda-\pi^\circ$ mass cut preferentially removes events which fall on the lower side of the $\Xi^\circ\rightarrow\Lambda\gamma$ mass distribution, thus shifting the apparant final mass peak to slightly higher mass.

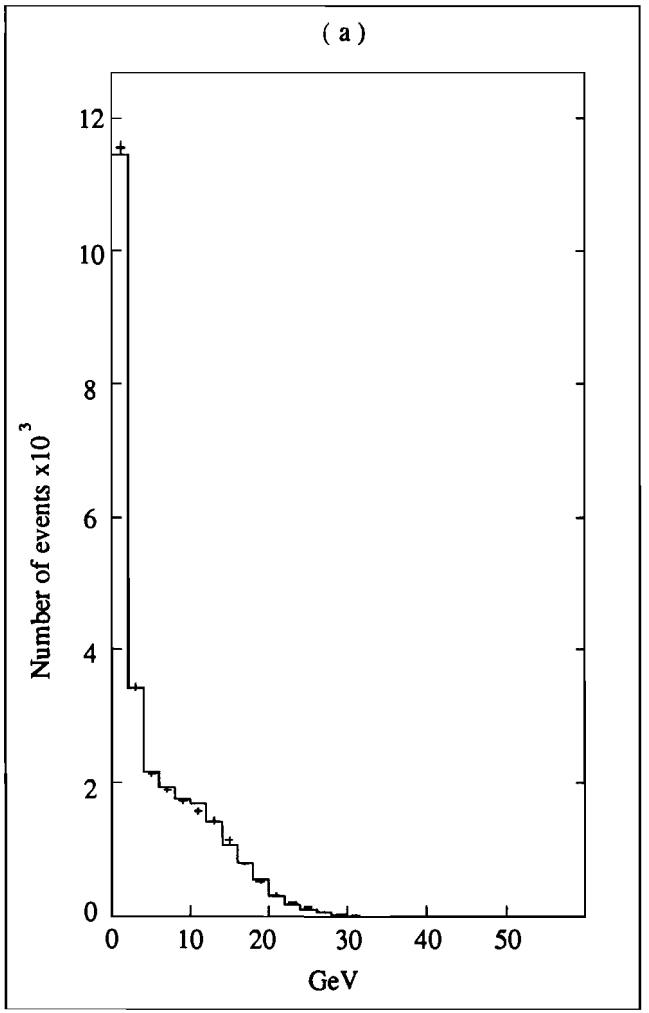

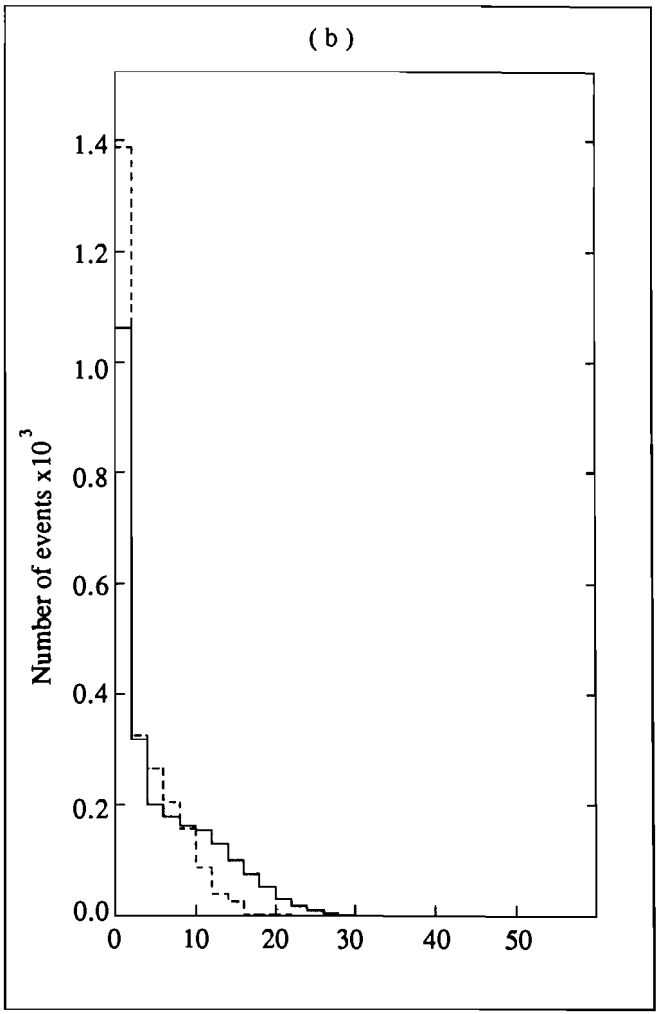

Fig. 4.16 : The missing γ energy, as determined from the 1–γ $\Xi^0 \rightarrow \Lambda\pi^0$ fit. The background Monte Carlo is compared to (a) the data and (b) the signal Monte Carlo, after the preliminary cuts have been applied.

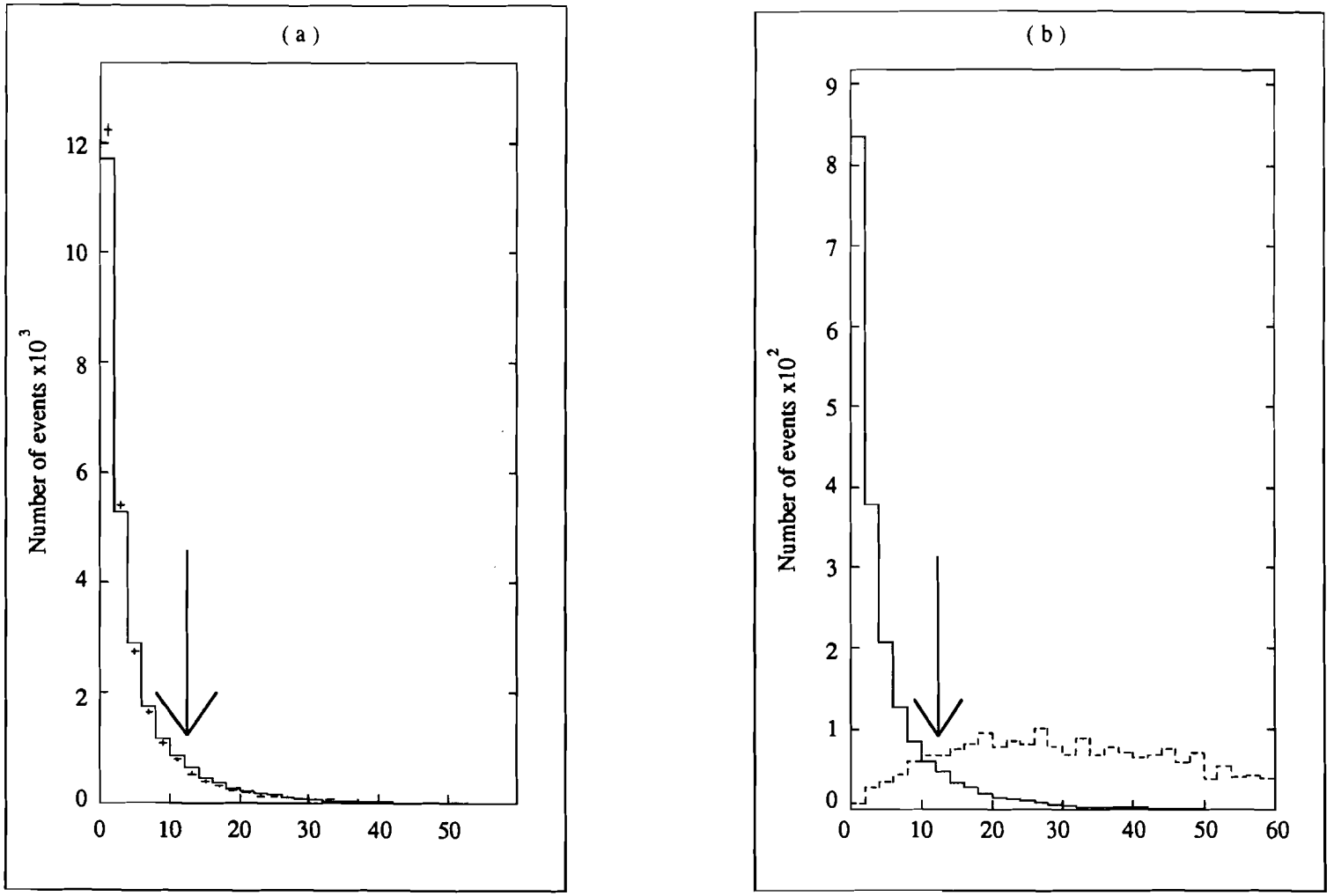

Fig. 4.17 : The chi-squared χ^2_{Ξ} from the 1–γ $\Xi^0 \rightarrow \Lambda\pi^0$ fit. The background Monte Carlo (solid line) is compared to (a) the data and (b) the signal Monte Carlo after the preliminary cuts have been applied. The arrows show where a cut was applied.

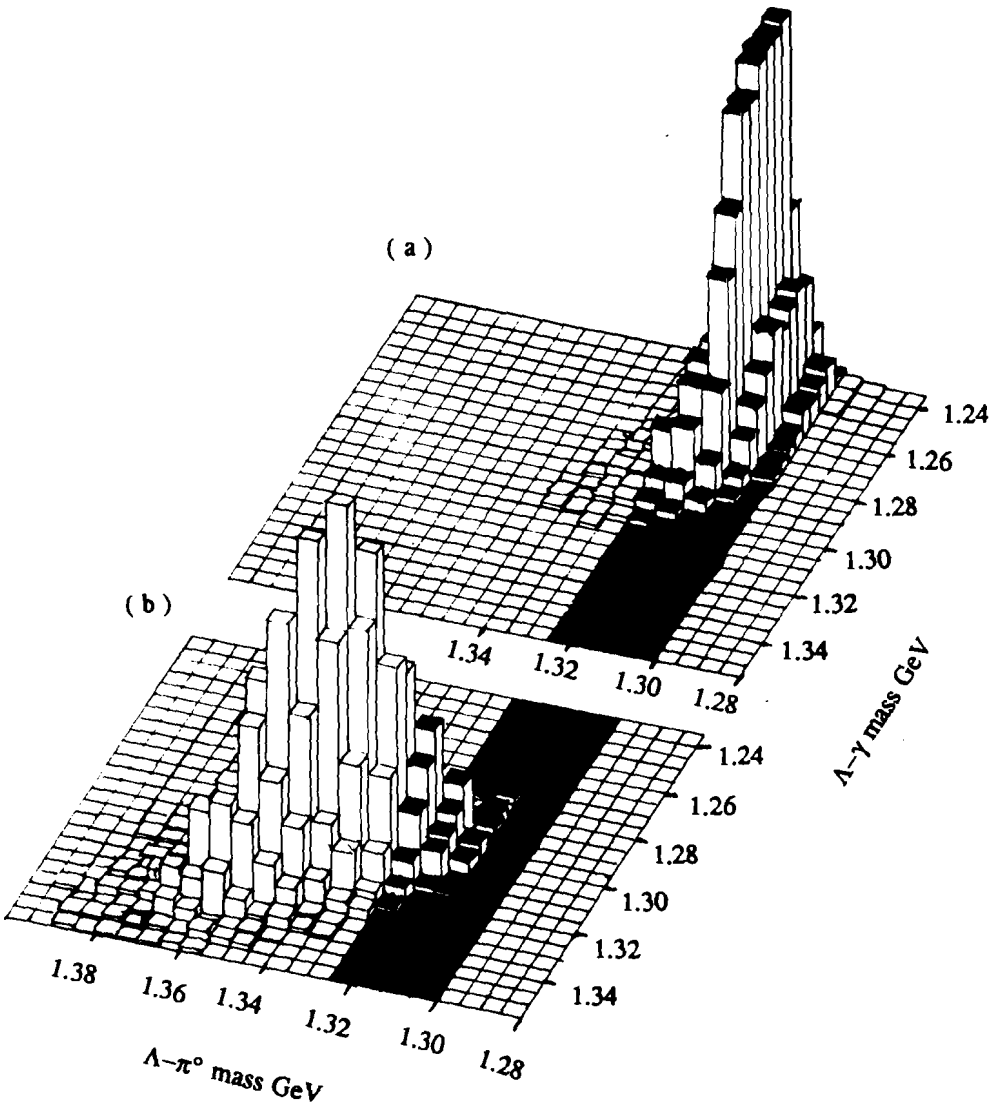

Fig. 4.18 : A two dimensional plot of Λ–γ mass vs the 1-γ fit Λ–π° mass. (a) is the background Monte Carlo and (b) is the signal Monte Carlo. The plot shows the correlation between low $\Xi^\circ \rightarrow \Lambda\gamma$ mass and Λ–π° mass.

4.23 High Λ p_t vs. Primakoff target pointing

There was some background present not accounted for by the Ξ° background Monte Carlo. When some of the cuts discussed so far had been applied and a possible $\Xi^\circ \rightarrow \Lambda\gamma$ signal began to appear, there were also some high mass - high p_t events that appeared. Upon investigation, many of the high p_t events pointed back to the Primakoff target. The effect could be seen by comparing the data close approach vertex distribution, Fig. 4.19, with the distributions from the background Monte Carlo, after cuts were applied to reduce the data Ξ° background. The distributions were normalized to the number of data events outside the primakoff target area, >6m. The data was found to have an excess of events in the area of the Primakoff target, between 2.5m and 4.5m. The vertex distribution of data taken with 1 radiation length Primakoff targets was also compared to the vertex distribution of data taken with radiation length < 0.15; the large radiation length Primakoff target data had a higher proportion of Λ's which pointed to the target area and had high p_t. The high p_t events could be very large angle Λ scatters in the Primakoff target material not accounted for in the Monte Carlo; or they could be Λ's from the decay of excited hyperon states, like Σ^*'s, produced in the Primakoff target. A Monte Carlo of Σ^*'s produced at the Primakoff target indicated that virtually all the daughter Λ's would point back to the target area, between 2m and 5m. Analysis of the data (both 2-γ and 1-γ samples) for Σ^*'s indicated that there were too few to account for the final Λ–γ mass peak, and the shape of their Λ–γ mass distribution was wider than the one observed. Because the Σ^* has a higher mass (1.380 GeV) than the Ξ°, the decay $\Sigma^* \rightarrow \Lambda\pi^\circ$ gives the Λ a higher p_t than either the decays $\Xi^\circ \rightarrow \Lambda\pi^\circ$ or $\Xi^\circ \rightarrow \Lambda\gamma$. A cut was devised eliminating any event with the close approach vertex between 2.5m and 4.5m, and a Λ p_t > .20 GeV. Events with p_t > .23 GeV, no matter where their vertex was, were already removed by the preliminary cuts. This cut removed about 3% of the signal Monte Carlo and 10% of the data.

4.24 The Coplanar Test

Another kinematic fit important to the analysis tested the coplanarity of the decay products in the decay $X \rightarrow \Lambda\gamma$. In any real two body decay the momentum vectors of the decay products and the parent

must lie in a plane. The mass of X was not constrained, but X's momentum vectors were constrained to point back to the production target. The initial decay point was taken to be the closest approach of the Λ to the neutral beam, the same decay point used in the 1-γ Ξ° fit. The momenta of the decay products were varied, within errors, to make the momentum componets transverse to the boost of X lie in the same plane. A χ^2 was calculated for the fit; then, as in the 2-γ Ξ° fit, the decay vertex of X was moved along the z-axis, but constrained to be within the neutral beam cone, until the minimum χ^2 was found. The z position of the decay vertex was not allowed to be less than zero, or greater than the z position of the Λ decay vertex. The result of the fit was a new decay vertex and fitted X vectors, and the coplanarity chi-squared χ^2_c. The $\Lambda-\gamma$ mass shown in the final analysis was the one calculated from this fitted vertex of X, and from the measured Λ and γ momenta. A Λ-γ mass could also be calculated from the fitted Λ and γ vectors.

The fitted vertex z position and χ^2_c are shown in Figs. 4.20 and 4.21. When only the preliminary cuts were applied, as for these distributions, the background χ^2_c behaves much like the signal. However, when the other cuts discussed so far have been applied, then the χ^2_c distribution for background differs from that for the signal, as will be seen in the next section.

4.30 Combining Cuts

Any one of the cuts discussed so far, on the $\Lambda-\pi^\circ$ mass, the χ^2_Ξ or on p_t vs E_γ, if taken alone, did not reduce the background enough to see a clear $\Xi^\circ \rightarrow \Lambda\gamma$ signal. Taken together, however, evidence for a signal did appear. Table 4.2 gives the cumulative effects of these cuts on the data, the background Monte Carlo, and on the signal Monte Carlo.

Each of the following paragraphs describes briefly a combination of cuts applied, the reduction effects, and the number of events left after a subtraction of background. The number of events were counted in the region occupied by the signal Monte Carlo under the same cuts. Note that after these cuts are applied, particularly the $\Lambda-\pi^\circ$ mass cut, the $\Lambda-\gamma$ Monte Carlo mass has its low mass side cut out. Figs. 4.22 through 4.28 show the Λ-γ mass, for data, background and signal Monte Carlos, after the

discussed cuts have been applied, and the Λ-γ mass after background subtraction with the normalized signal Monte Carlo superimposed on it.

Fig. 4.22 shows the X→Λγ mass calculated from the fitted vectors from the coplanarity fit. The cuts applied require the event to have passed the 1-γ Ξ°→Λπ° fit and have a $\chi^2_{\Xi} > 12$, and a Λ $p_t > 0.17$. The cuts reduce the data by a factor of 30, the background Monte Carlo by a factor of 40, and the signal Monte Carlo by a factor of 1.7. A bin by bin subtraction of the background from the data in Fig. 4.22a, shown in Fig. 4.23, gives an estimated 183±14 events in the area occupied by the Ξ°→Λγ peak in Fig. 4.22b, between 1.29 and 1.36 GeV.

Fig. 4.24 shows the Λ–γ mass calculated from the detected Λ momentum and γ energy, but using the vertex from the X→Λγ coplanarity fit. The cuts applied require, as above, the event to have passed the 1-γ Ξ°→Λπ° fit and have a $\chi^2_{\Xi} > 12$. In addition, the Λ pt vs. Eγ cut has been applied, removing events with $p_t < 0.16$ and Eγ < 30 GeV. The data has been reduced by a factor of about 23, the background Monte Carlo by a factor of 26, and the signal Monte Carlo by 1.4. Again, a bin by bin subtraction of background in Fig.4.24a, shown in Fig. 4.25, yeilds 182±13 events in the region occupied by the Ξ°→Λγ mass in Fig. 4.24b, between 1.29 and 1.36 GeV.

The final set of combined cuts, Figs. 4.26 and 4.27, applies the same cuts discussed for Fig. 4.24. Also applied are the 3σ cut on the Ξ°→Λπ° mass from the 1-γ fit discussed in Sec. 4.22, the Λ p_t vs. vertex location cut discussed in Sec. 4.23, and a cut on the coplanarity chi-squared, requiring $\chi^2_c <$ 20. This set of cuts reduced the data by a factor of about 110, the background Monte Carlo by a factor of 230, and the signal Monte Carlo by 1.94. A bin by bin subtraction of the background in Fig. 4.26, shown in Fig. 4.28, yields 139±12 events in the mass region occupied by Ξ°→Λγ decays in Fig. 4.27, between 1.29 and 1.36 GeV. Fig. 4.29 shows the χ^2_c for the data and the background Monte Carlo, superimposed, and for the signal Monte Carlo. The background distribution is now relatively flat whereas before the final cuts it overlapped the signal distribution. The data has the peaked shape of the signal distribution, above the background. The χ^2_c distribution gives evidence of two-body decay coplanarity of the events left on the mass plot. Note that because of the cuts imposed, the mass peak of

the signal, both in data and Monte Carlo, has been shifted slightly higher than the Ξ° mass. Agreement between the widths of the data signal and the $\Xi^\circ \rightarrow \Lambda\gamma$ Monte Carlo is also good evidence that the signal really are $\Xi^\circ \rightarrow \Lambda\gamma$ decays. Figs. 4.30 to 4.34 show the Λ mass, Λ-γ decay vertex distribution, the γ energy, the Λ P_t and the Λ decay vertex distributions for set #3 cuts. As mentioned earlier, the background has been normalized absolutely to the number of $\Xi^\circ \rightarrow \Lambda\pi^\circ$ decays expected from the 2-γ analysis in the comparisons between data and background Monte Carlo; whereas the comparisons between the two Monte Carlos are normalized to the same number of events.

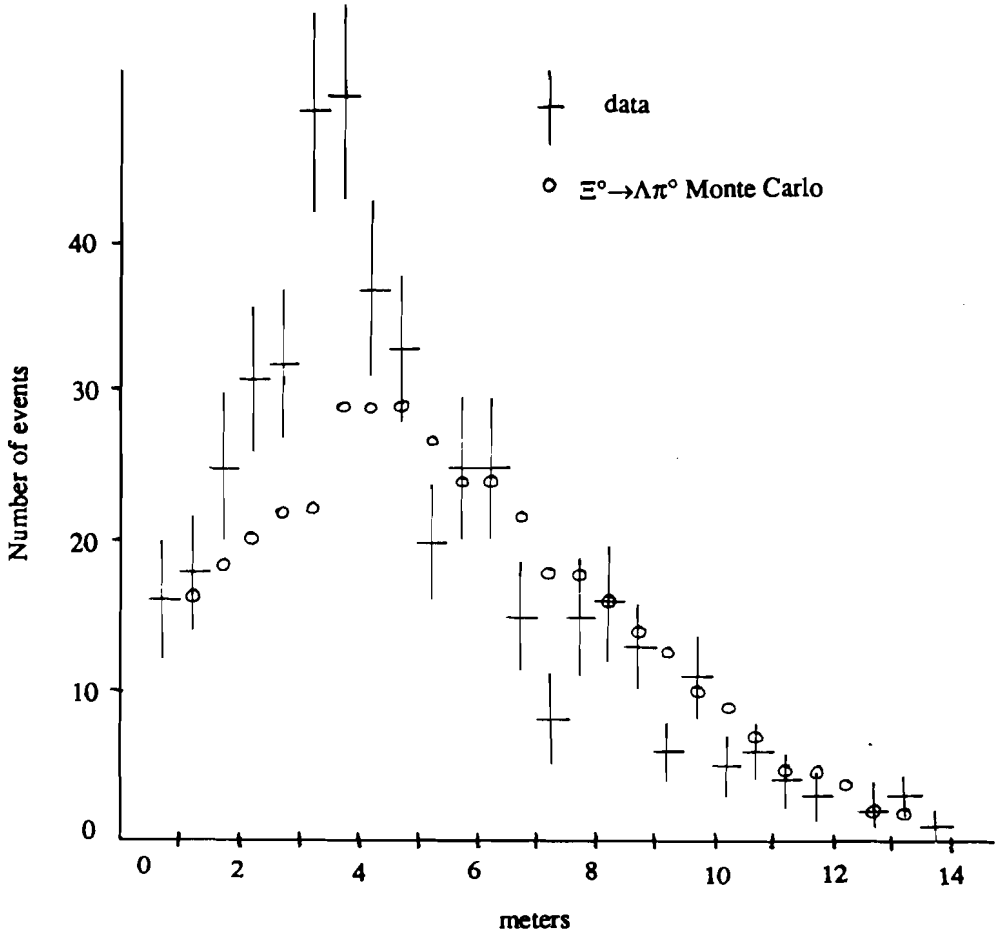

Fig. 4.19 : The vertex of Λ closest approach, after cuts similar to those used for set #2. The data shows an excess of events in the Primakoff target area, and they are correlated with high Λ p_t.

Table 4.2

$\Lambda-\gamma$ final cuts

requirements	fraction of data passing	fraction of $\Xi^\circ \to \Lambda\pi^\circ$ MC passing	fraction of $\Xi^\circ \to \Lambda\gamma$ MC passing	# of candidate events
combined set 1:				
pass 1-$\gamma\,\Xi^\circ \to \Lambda\pi^\circ$ fit				
$\chi^2_\Xi > 12$				
$p_t > 0.17$ GeV	0.033	0.025	0.580	183
combined set 2:				
pass 1-$\gamma\,\Xi^\circ \to \Lambda\pi^\circ$ fit				
$\chi^2_\Xi > 12$				
p_t vs E_γ	0.044	0.039	0.702	182
combined set 3:				
pass 1-$\gamma\,\Xi^\circ \to \Lambda\pi^\circ$ fit				
$\chi^2_\Xi > 12$				
p_t vs E_γ				
$\Lambda-\pi^\circ$ 3σ mass cut				
$\chi^2_c < 20$				
p_t vs vertex location	0.009	0.004	0.520	139

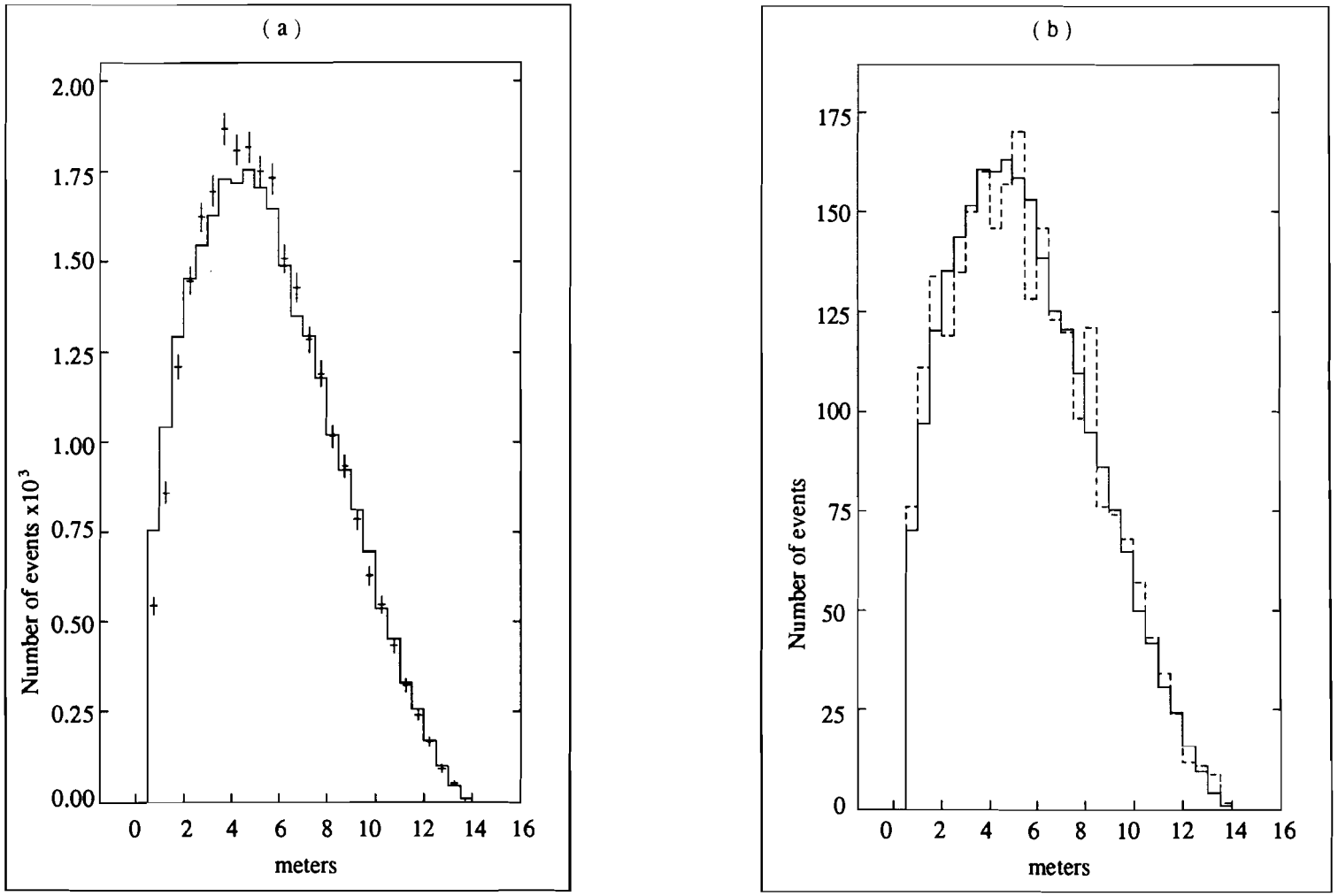

Fig. 4.20 : The vertex from the X→Λγ fit. The background Monte Carlo (solid line) is compared to (a) data and (b) the signal Monte Carlo, after only the preliminary cuts have been applied.

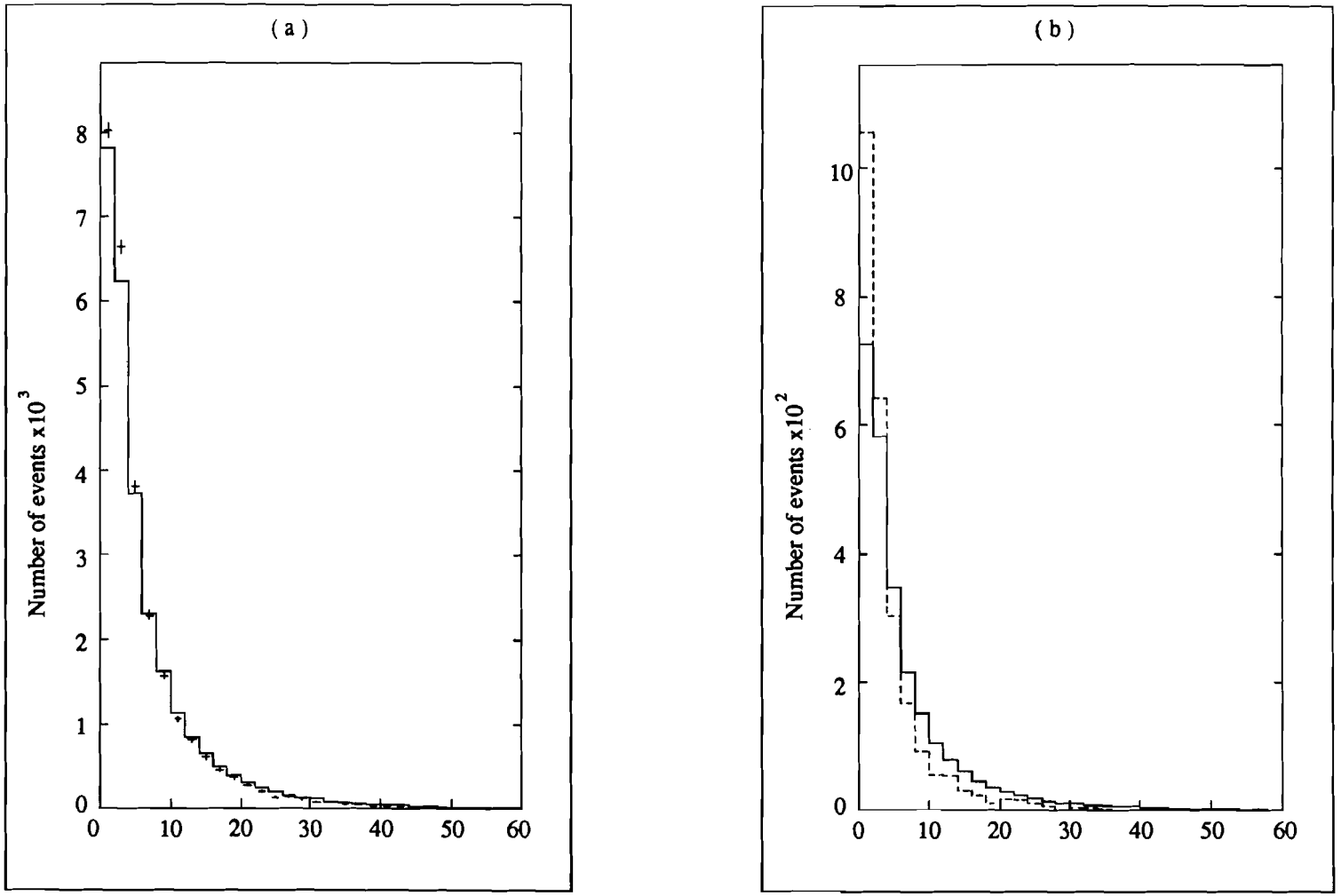

Fig. 4.21 : The chi-squared from the $X \rightarrow \Lambda\gamma$ coplanar fit. The background Monte Carlo is compared to (a) the data and (b) the signal Monte Carlo, after only the preliminary cuts have been applied.

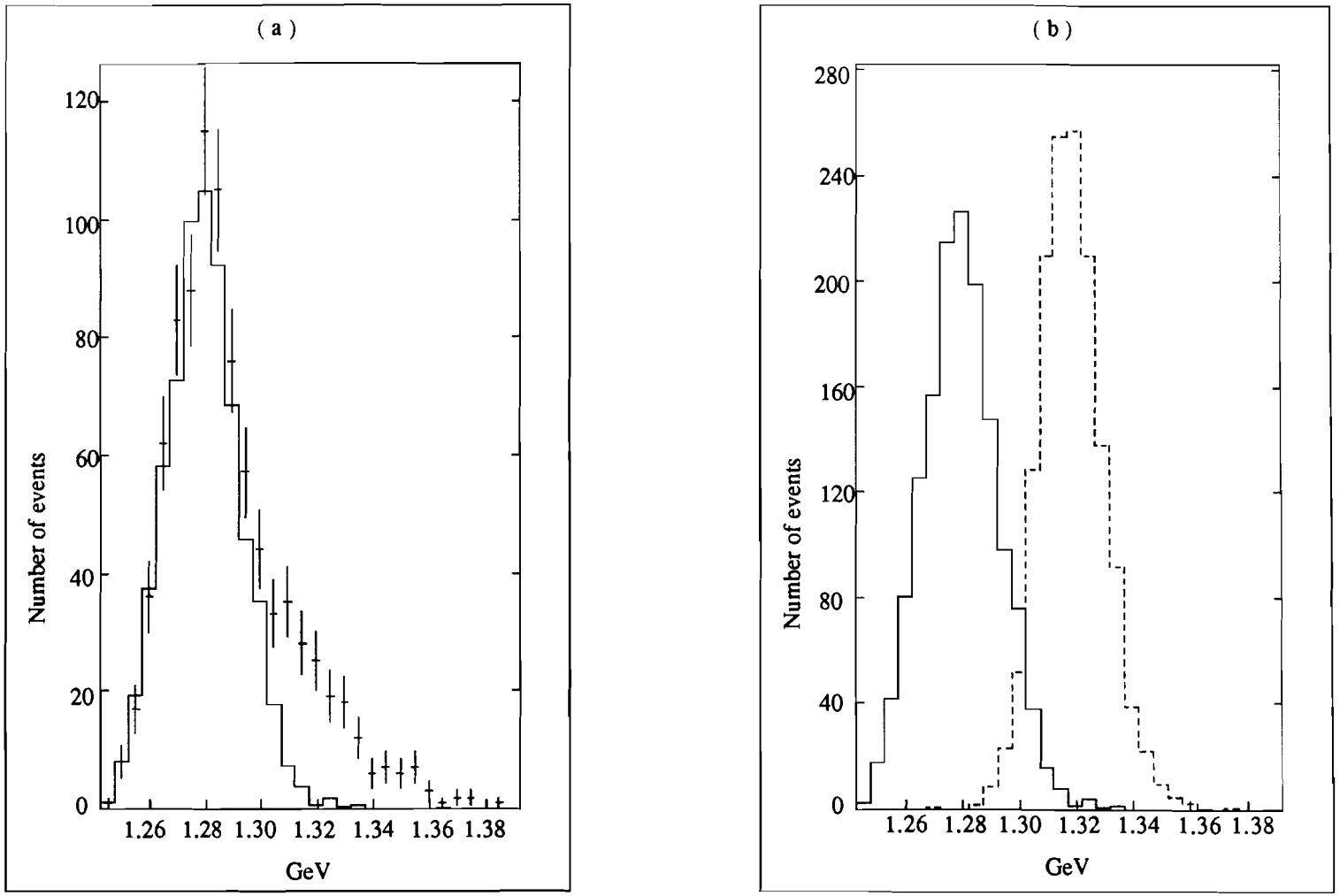

Fig. 4.22 : The mass calculated with the fitted vectors from the $X \rightarrow \Lambda\gamma$ coplanar fit, with set #1 cuts as shown on Table 4.2. The background Monte Carlo (solid line) is compared to (a) the data and (b) the signal Monte Carlo.

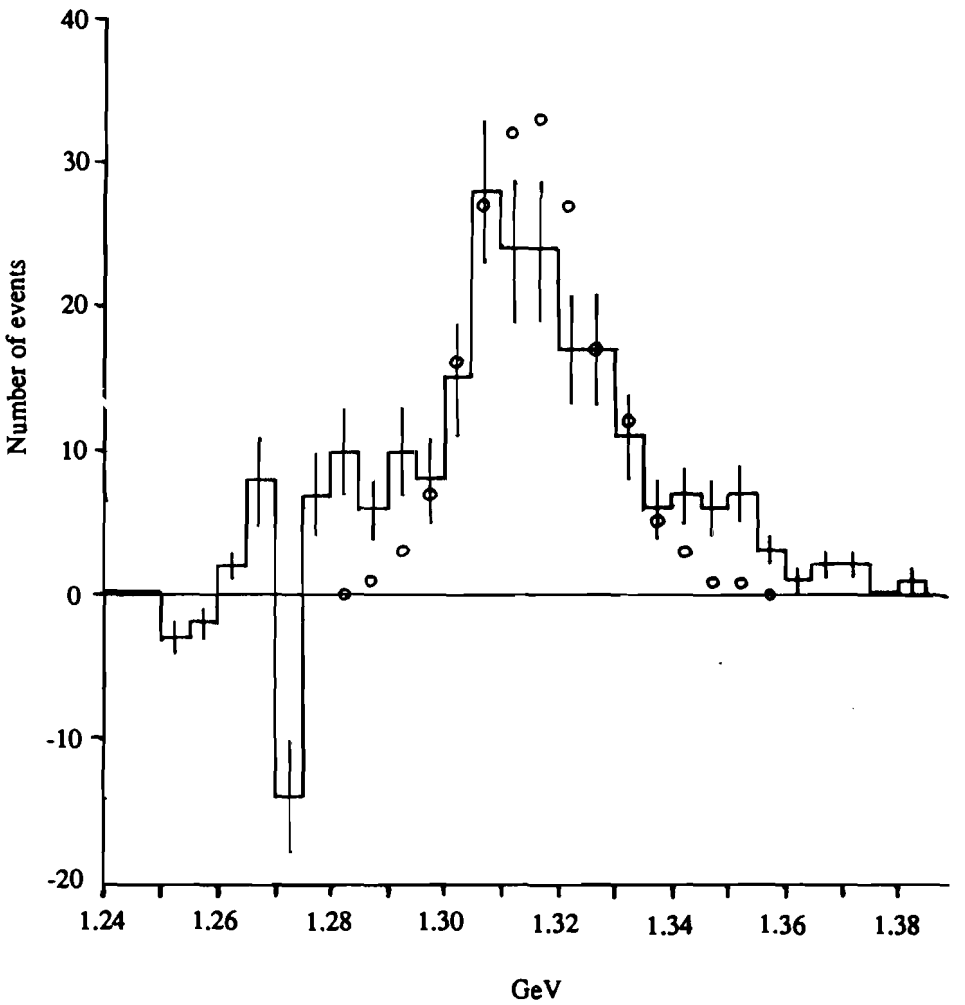

Fig. 4.23 : The Λ-γ mass plot of Fig. 4.22a, after a bin by bin background subtraction. The number of events between 1.29 and 1.36 GeV is 183. The circles are the signal Monte Carlo under the same set of cuts and normalized to 183 events.

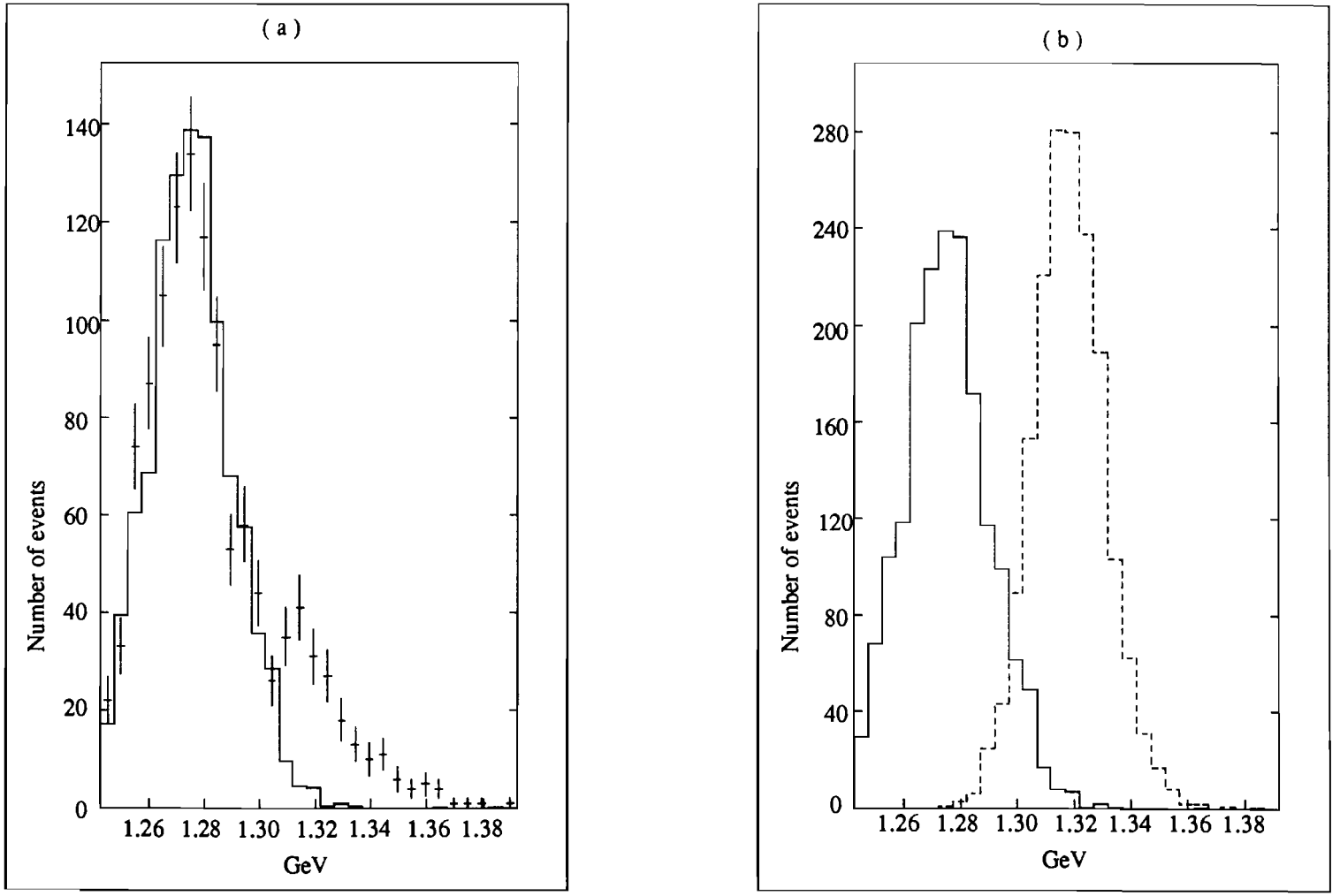

Fig. 4.24 : The $\Lambda-\gamma$ mass distribution, with set #2 cuts as given in Table 4.2. The background Monte Carlo is compared to (a) the data and (b) the signal Monte Carlo.

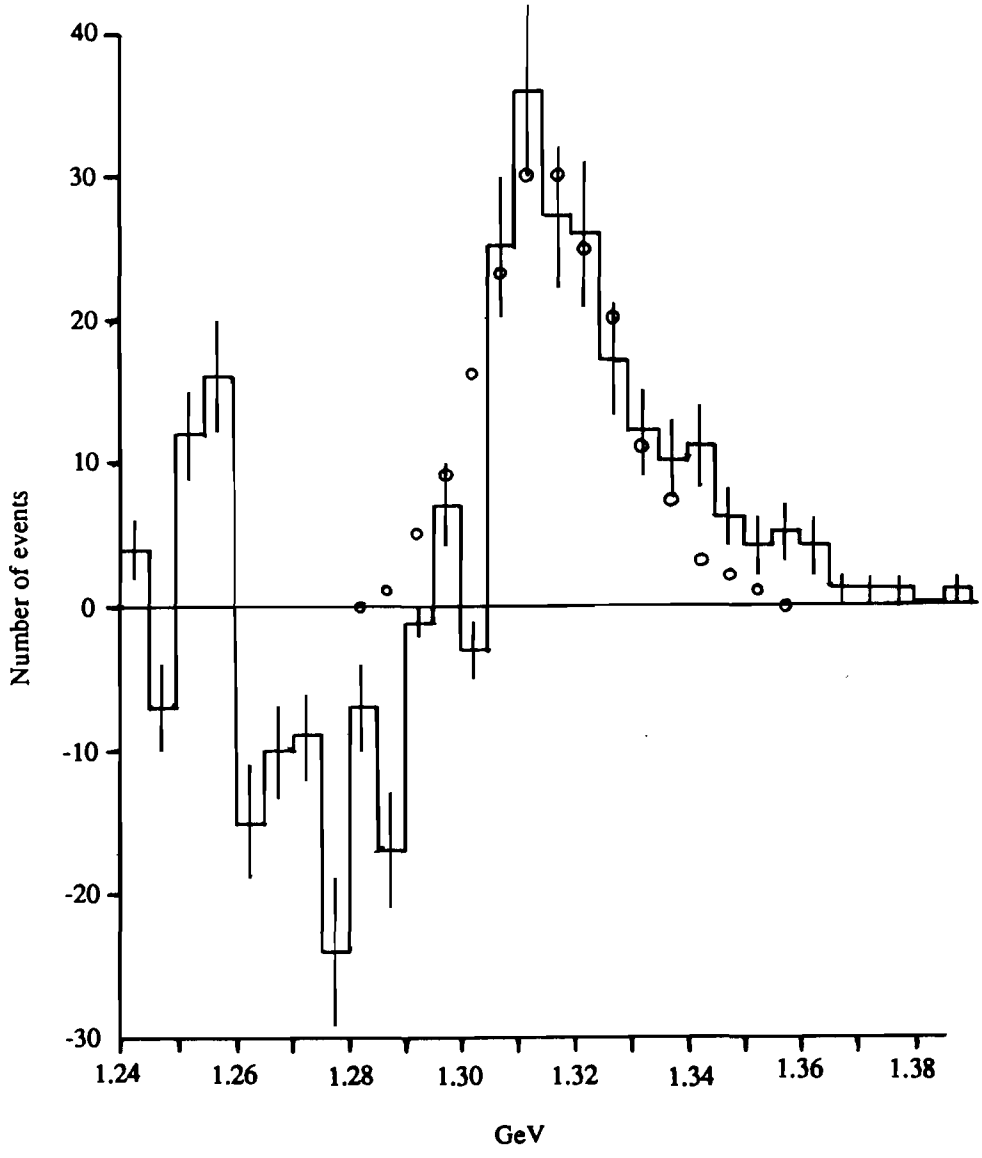

Fig. 4.25 : The Λ-γ mass plot of Fig. 4.24a, after a bin by bin background subtraction. The number of events between 1.29 and 1.36 GeV is 182. The circles are the signal Monte Carlo under the same set of cuts and normalized to 182 events.

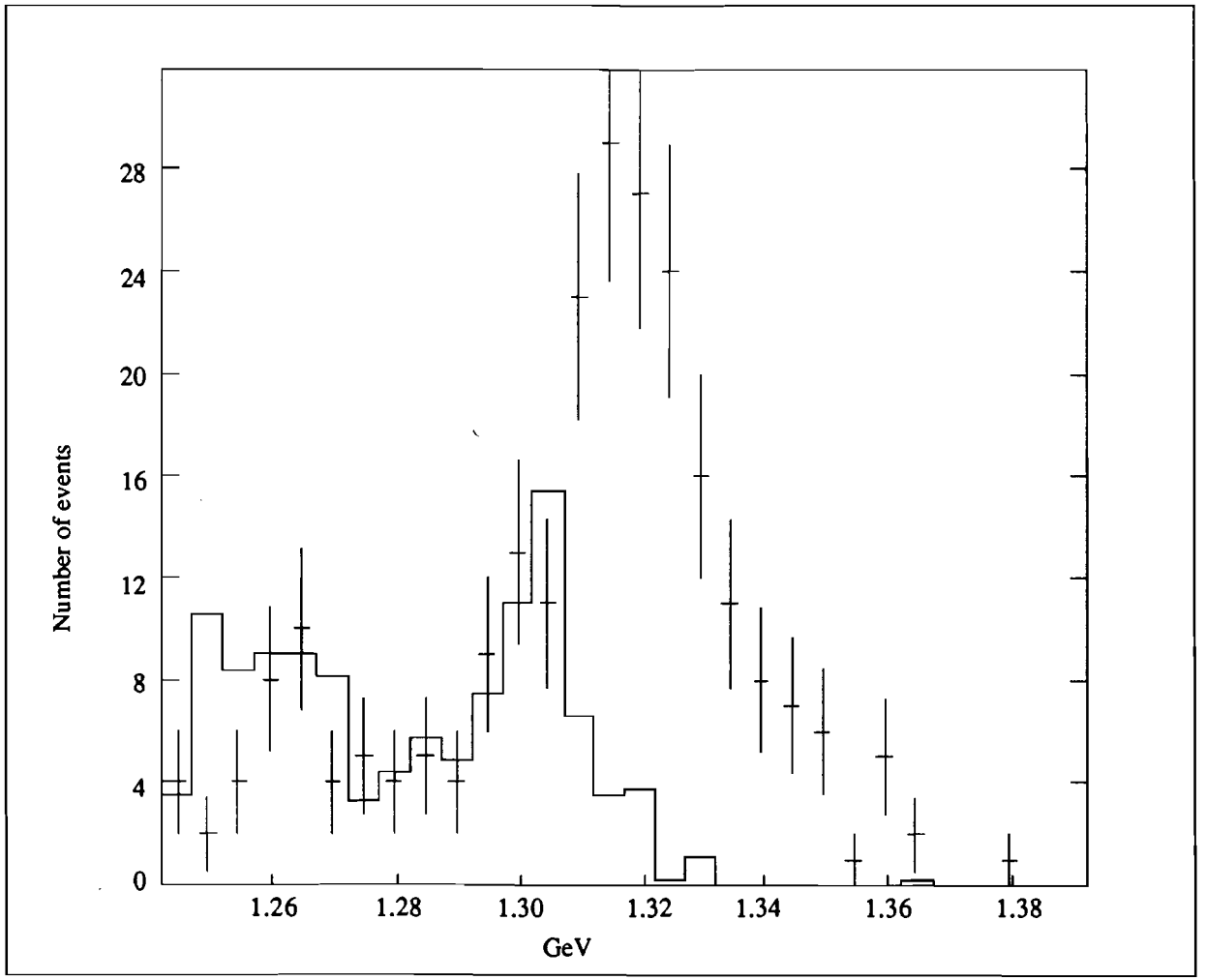

Fig. 4.26 : The $\Lambda-\gamma$ mass distribution with set #3 cuts as given in Table 4.2. The background Monte Carlo (solid line) is compared to the data. The background has been normalized to an absolute number of Ξ° expected to be present.

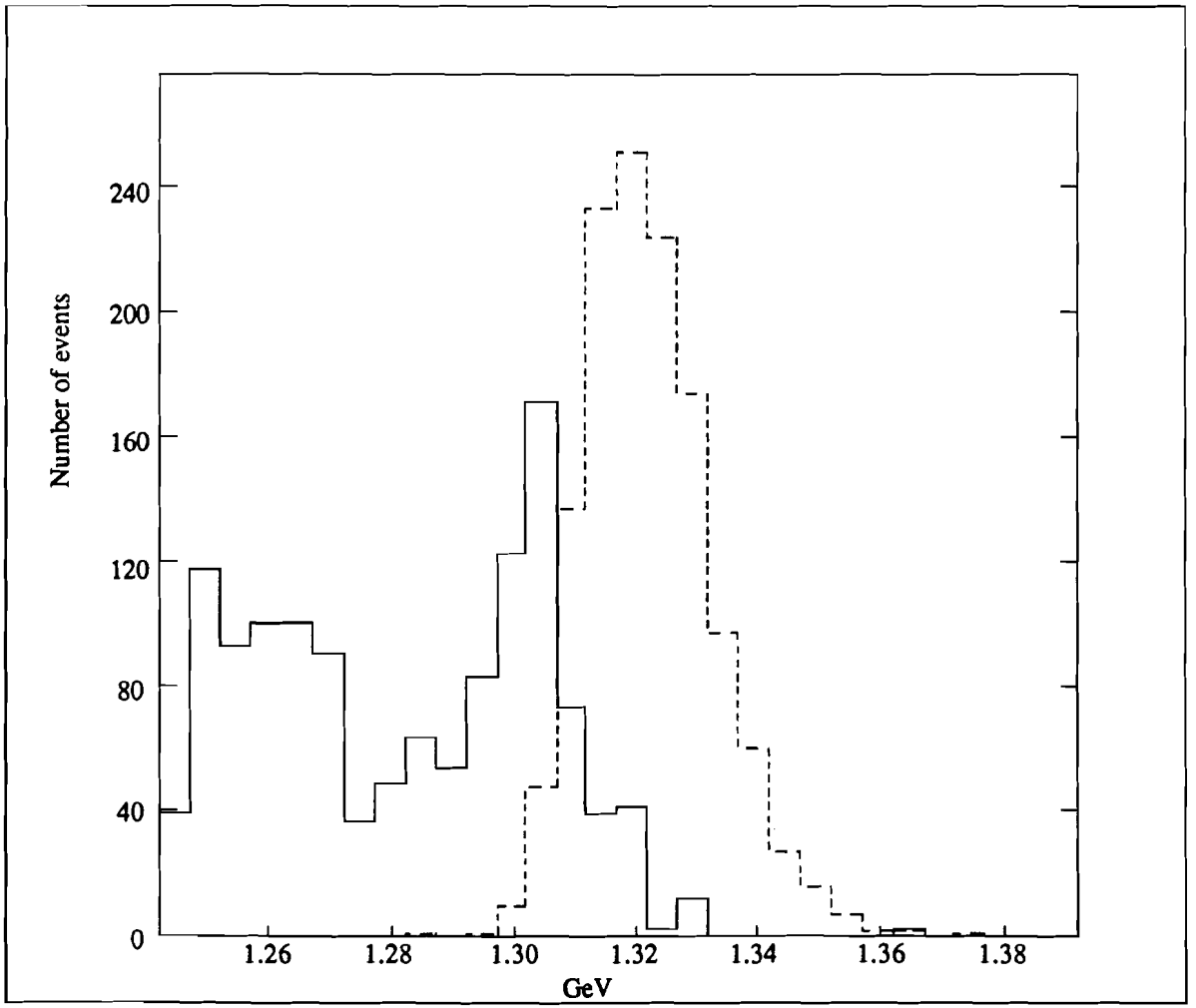

Fig. 4.27 : The Λ–γ mass distribution with set #3 cuts as given in Table 4.2. The background Monte Carlo (solid line) is compared to the signal Monte Carlo. The two MC sets have been normalized to the same arbitrary number of events.

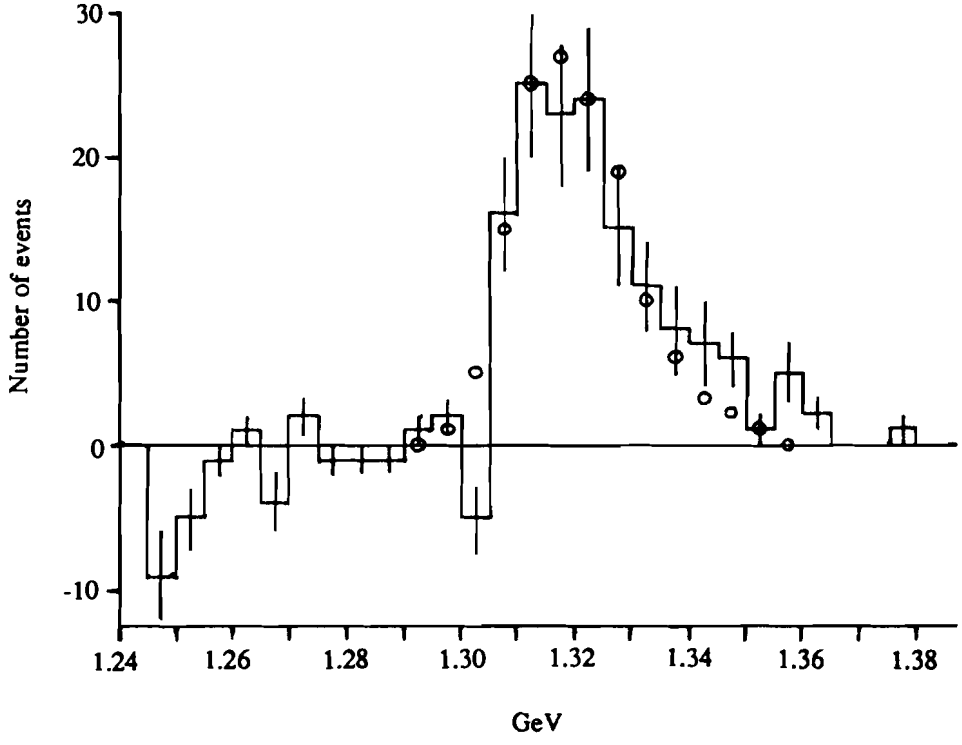

Fig. 4.28 : The Λ-γ mass plot of Fig. 4.26, after a bin by bin background subtraction. The number of events between 1.29 and 1.36 GeV is 139. The circles are the signal Monte Carlo under the same set of cuts and normalized to 139 events.

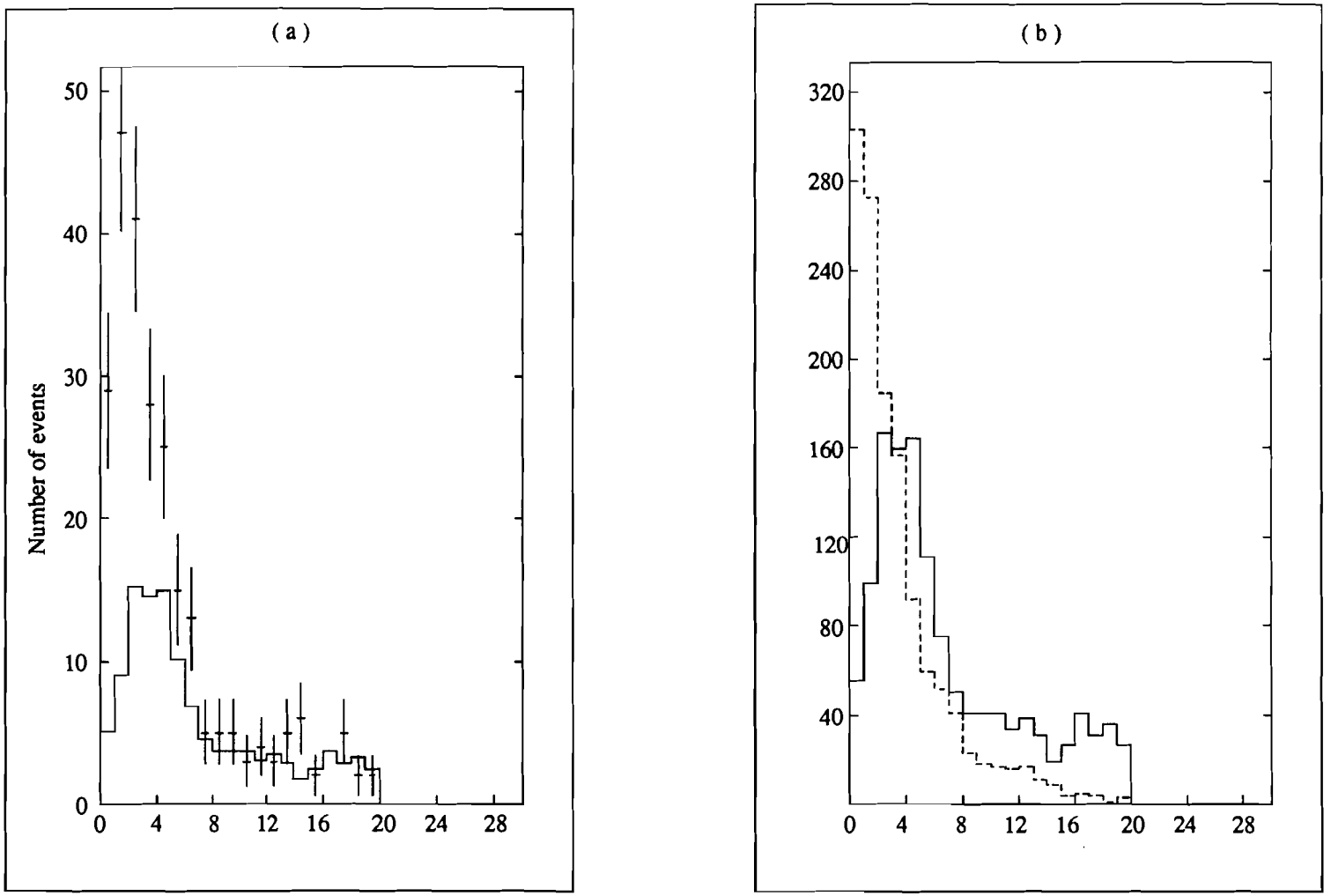

Fig. 4.29 : The chi-squared from the $X \rightarrow \Lambda\gamma$ fit, with set #3 cuts applied, comparing background Monte Carlo (solid line) to (a) the data and (b) the signal Monte Carlo. The remaining data behaves similar to the signal $\Xi^0 \rightarrow \Lambda\gamma$ Monte Carlo decays.

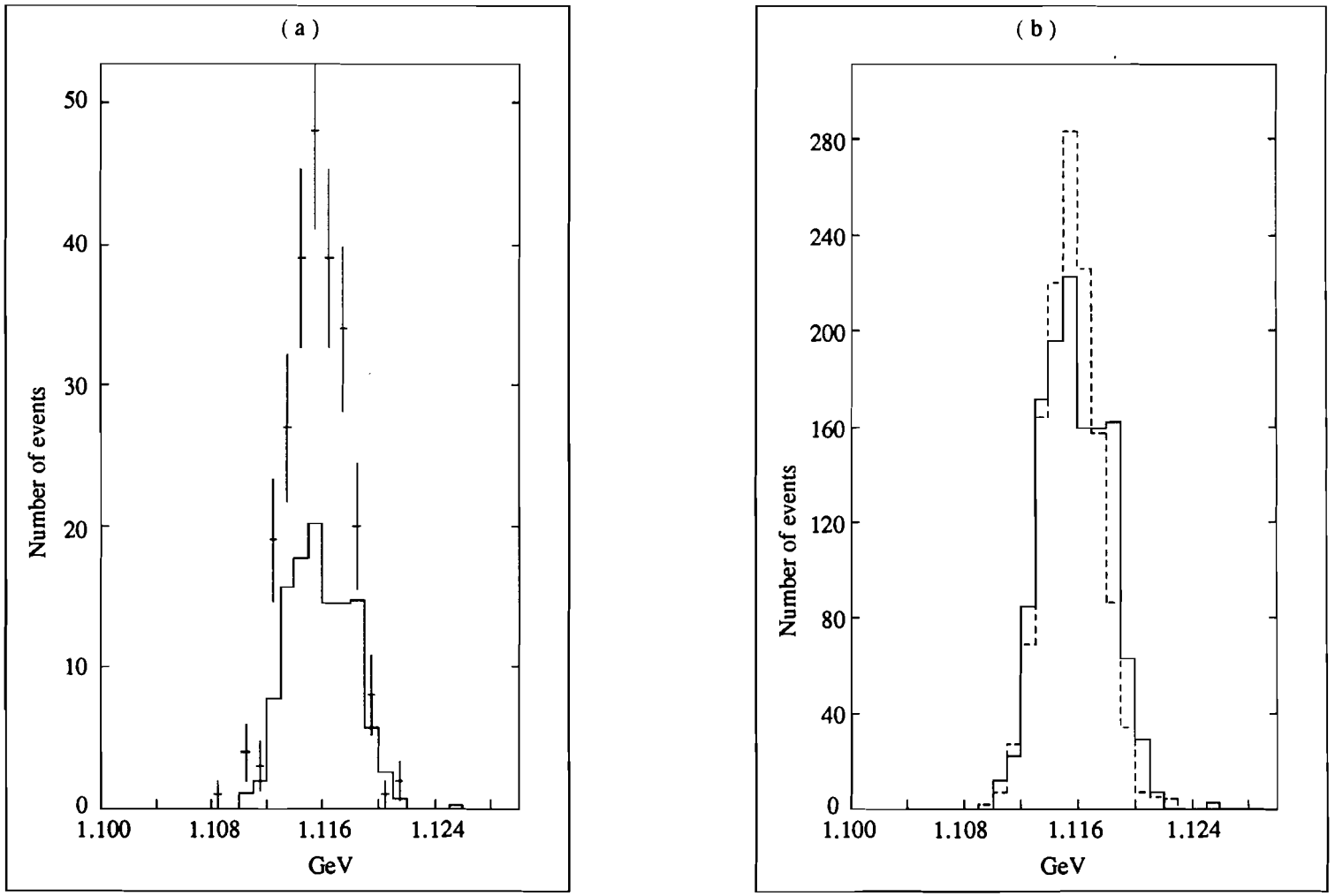

Fig. 4.30 : The Λ mass distribution with set #3 cuts applied, comparing background Monte Carlo (solid line) to (a) the data and (b) the signal Monte Carlo.

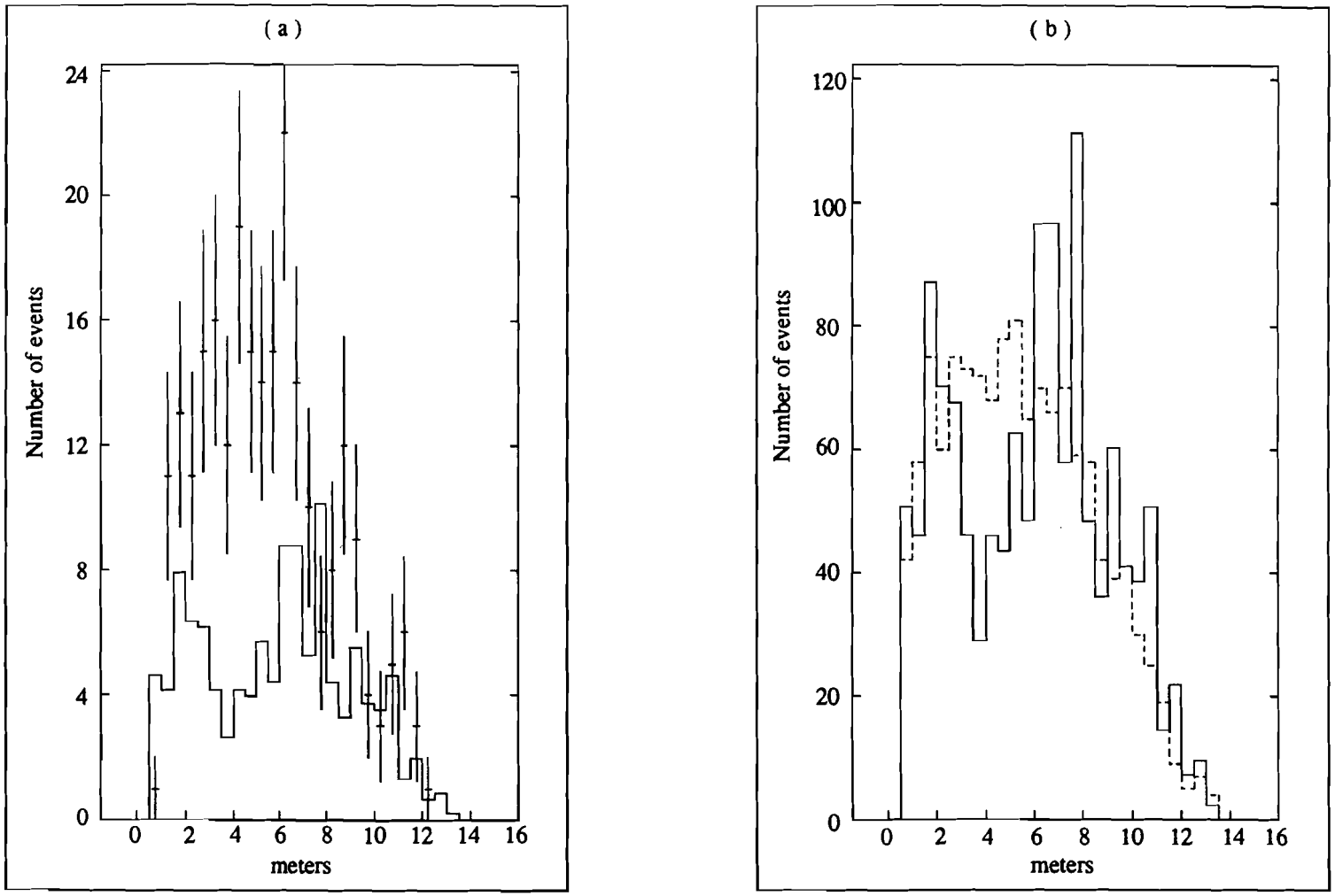

Fig. 4.31 : The Λ–γ parent decay vertex, with set #3 cuts applied, comparing background Monte Carlo (solid line) to (a) the data and (b) the signal Monte Carlo.

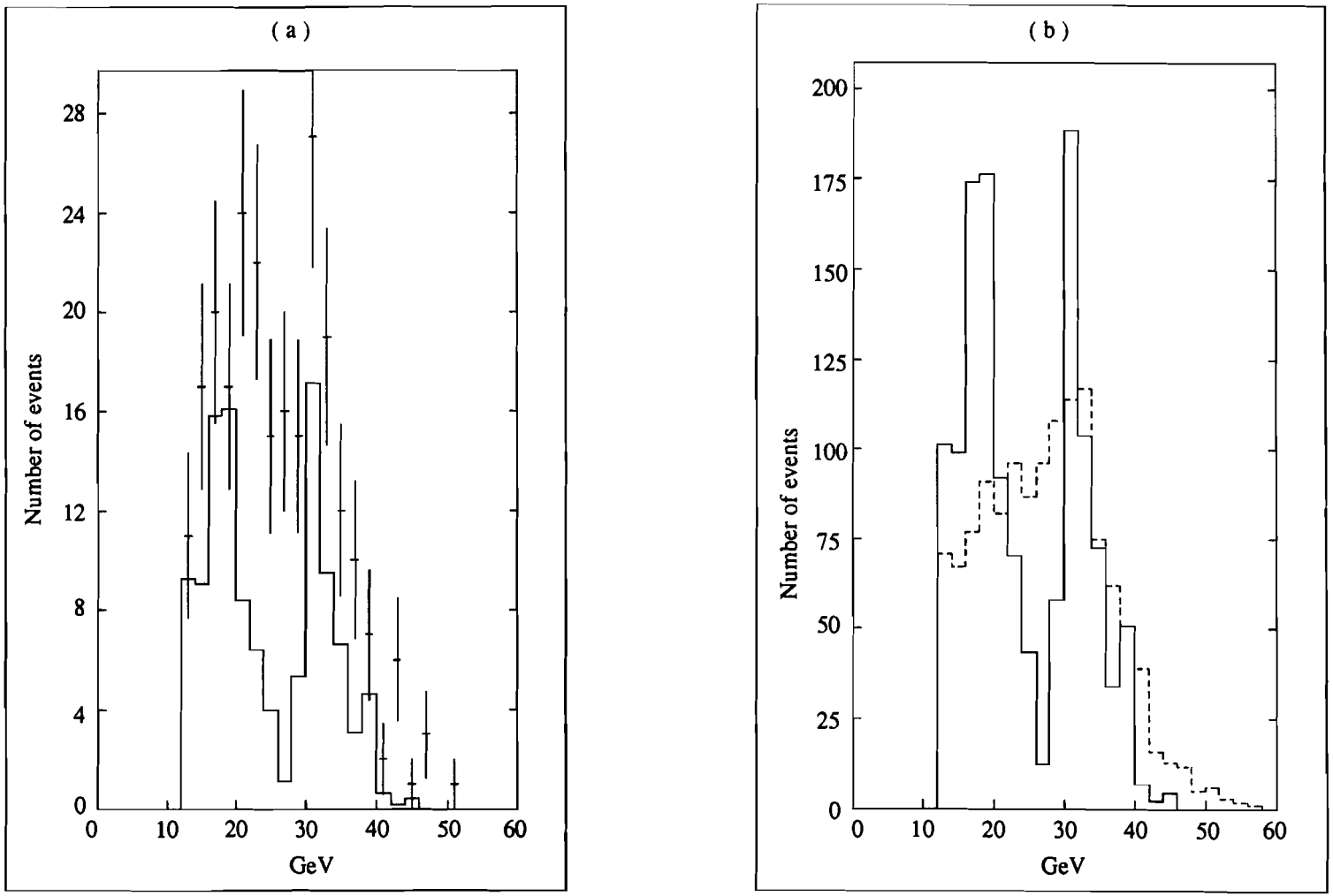

Fig. 4.32 : The gamma energy, with set #3 cuts applied, comparing the background Monte Carlo (solid line) to (a) the data and (b) the signal Monte Carlo.

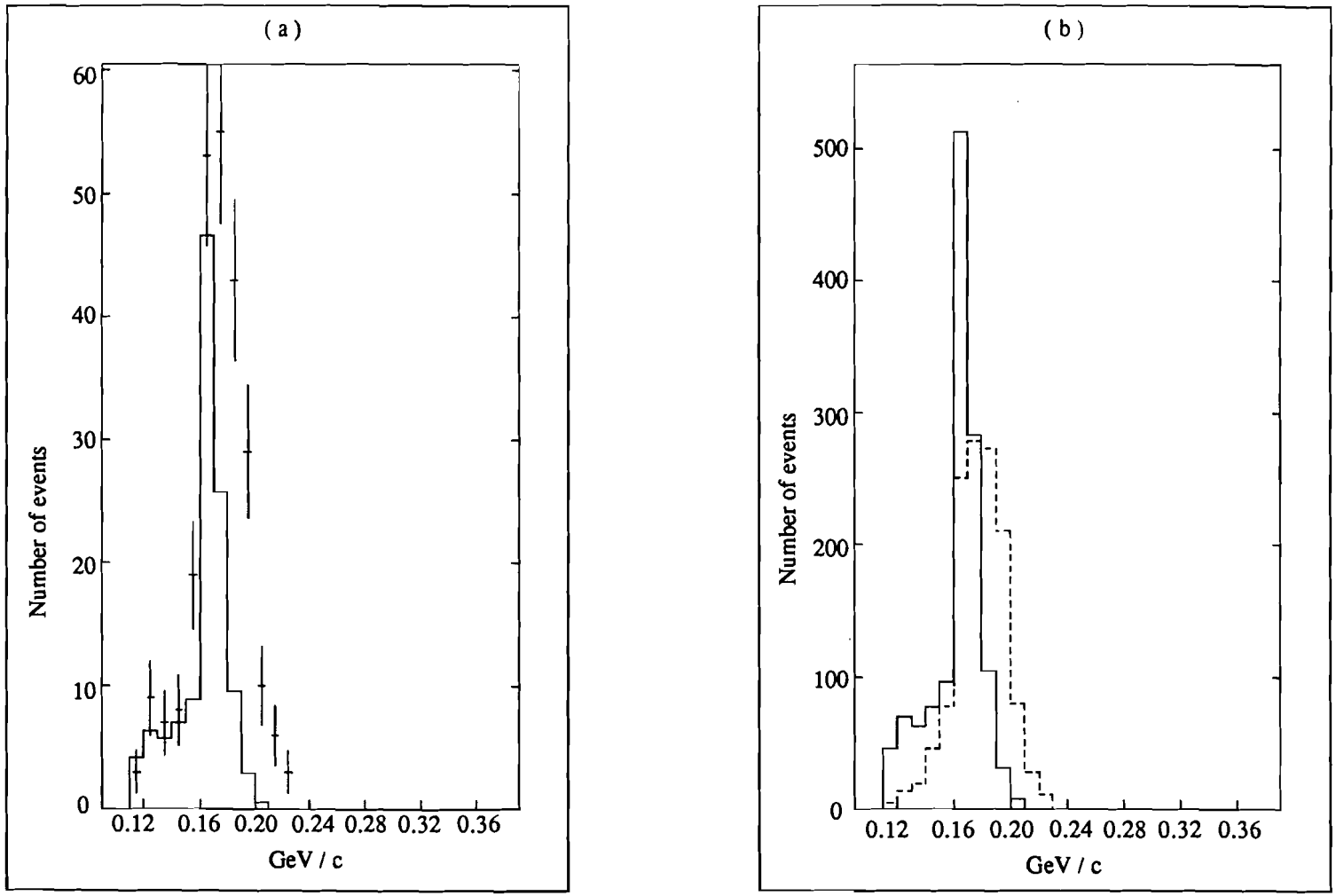

Fig. 4.33 : Transverse momentum of the Λ, with set #3 cuts applied, comparing the background Monte Carlo (solid line) to (a) the data and (b) the signal Monte Carlo.

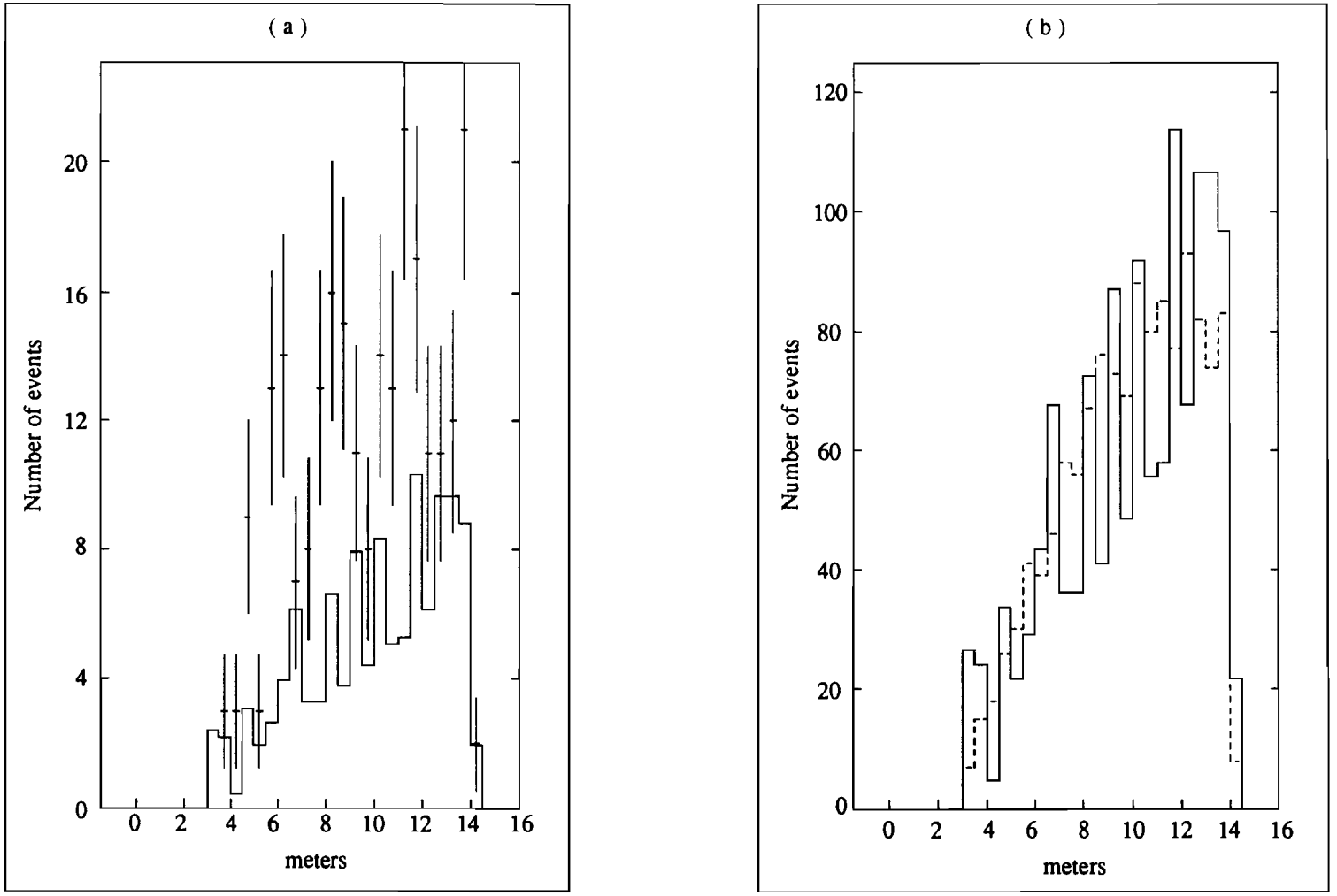

Fig. 4.34 : The Λ decay vertex distribution, with set #3 cuts applied, comparing the background Monte Carlo (solid line) to (a) the data and (b) the signal Monte Carlo.

Chapter 5

Results

The branching ratio is calculated by dividing the number of $\Xi^\circ \to \Lambda\gamma$ decays in the apparatus by the number of $\Xi^\circ \to \Lambda\pi^\circ$ decays in the apparatus. The number of each decay type in the apparatus is not the number detected, since the geometrical effects and analysis cuts on the two types are different. The fractions, called acceptances, of the number of Ξ°'s detected to the number of Ξ°'s originally in the apparatus come from the Monte Carlos for the two decay types. The equation for the branching ratio is then

$$\frac{\Xi^\circ \to \Lambda\gamma}{\Xi^\circ \to \Lambda\pi^\circ} = \frac{N_{\Lambda\gamma} \Big/ (\alpha_1 \cdot \alpha_2)}{N_{\Lambda\pi^\circ} \Big/ (\beta_1 \cdot \beta_2)}$$

where

$N_{\Lambda\gamma}, N_{\Lambda\pi^\circ}$ = the number of each decay type detected

α_1 , β_1 = the geometrical acceptance in the apparatus of $\Xi^\circ \to \Lambda\gamma$ and $\Xi^\circ \to \Lambda\pi^\circ$ respectively

α_2 , β_2 = the analysis acceptance of $\Xi^\circ \to \Lambda\gamma$ and $\Xi^\circ \to \Lambda\pi^\circ$ respectively

The number $N_{\Lambda\pi^\circ}$ was the number of fully detected and reconstructed Ξ° where both γ's were in the lead glass. The geometrical acceptance β_1 was the fraction of all generated $\Xi^\circ \to \Lambda\pi^\circ$ decays in the apparatus which passed the trigger requirements, had both γ's in the lead glass, and a reconstructed Λ. The phrase 'in the apparatus' was taken to be after the parent particle or its decay products had exited the

sweeping magnet M1. The fraction α_1 gave the proportion of generated $\Xi^\circ \rightarrow \Lambda\gamma$ decays which passed the trigger, had the γ in the lead glass, and a reconstructed Λ. The fractions are on the order of a few percent, due to the apertures in the acceptance of the apparatus.

The geometrical acceptances include the self-vetoing effect of the Primakoff target and target holder. Different acceptances were found for three different Primakoff target lengths : a length ≤ 0.15 radiation lengths, a length ~ 0.5 radiation lengths, and a length ~ 1.0 radiation lengths. The self-vetoing reduced the number of $\Xi^\circ \rightarrow \Lambda\pi^\circ$ triggers by a larger amount than the $\Xi^\circ \rightarrow \Lambda\gamma$ triggers, because the first decay has two γ's, either of which may self-veto the event. The Λ-π° geometric acceptances β_1 for the three Primakoff target radiation lengths are in Table 5.1. If the $\Xi^\circ \rightarrow \Lambda\gamma$ events were broken up into groups of Primakoff target radiation length, there would be too few events to make a good estimate of the number of candidates present. Therefore the geometric acceptance for $\Xi^\circ \rightarrow \Lambda\gamma$ decays was averaged over the different Primakoff target acceptances, weighted by the proportion of data taken on each target. The Λ-γ geometric acceptances α_1 were : 0.0700±0.0004 for Primakoff targets with a radiation length <0.15; 0.0640±0.0004 for the 0.5 radiation length Primakoff target; and 0.0620±0.0004 for the 1 radiation length Primakoff targets. The weighted average for α_1 was 0.0643±0.0004.

The fractions α_2 and β_2 are the analysis acceptances; the number of events passing the software analysis cuts used to detect clean samples of $\Xi^\circ \rightarrow \Lambda\pi^\circ$ and $\Xi^\circ \rightarrow \Lambda\gamma$ decays divided by the number of generated triggers, which passed all the geometrical criteria. These fractions can be broken up into parts dealing with the Λ analysis, the γ analysis, and the final event selection. The analysis acceptances include software cuts imposed to guarantee uniform efficiency of parts of the apparatus. For example, the veto counters S7 and S7a were supposed to exclude from the G.E. triggers any event where a charged particle hit the glass. These counters had some inefficiency, however, and some events with a π^- in the glass were flagged as G.E. triggers. A software cut eliminated any reconstructed events from the data and Monte Carlos where a π^- was tracked in to the glass. The inefficiencies of the counters did not then need to be included in the generation of Monte Carlo events. All the parts of β_2 are

contained in Table 3.1 for $\Xi^\circ \rightarrow \Lambda\pi^\circ$ decays; the parts that make up α_2 for $\Xi^\circ \rightarrow \Lambda\gamma$ decays are in Tables 4.1 and 4.2. Both α_2 and β_2 were the same for all Primakoff target radiation lengths.

There were two corrections to the acceptance due to effects in the data not included in the Monte Carlo. One was the TDC matching efficiency for 1-γ and 2-γ data sets; the numbers are on Tables 4.1 and 3.1. The error associated with these efficiencies is statistical. The other was another self-vetoing effect associated with veto counter S7. One cm downstream of the veto counter was a sheet of lead. Some of the γ's which converted in the lead sent a backscattered charged particle albedo into the counter, which vetoed the event. The fraction of events for which this occured was calculated by examining data for which counter S7 was not in veto, but was flagged if it saw a signal. The details of the calculation are found in Ref. 15. For events with one γ in the lead glass, 22% of them would self-veto. For events with two γ's in the glass, the fraction is larger, 39%, because either γ could veto the event.

Table 5.1 gives the calculation estimating the number of $\Xi^\circ \rightarrow \Lambda\pi^\circ$ decays in the apparatus. This number is the denominator in the branching ratio equation. All errors are statistical, and have been added in quadrature. Also shown is the calculation for the absolute normalization of the 1-γ background Monte Carlo decays for their comparisons to the data in the figures of Chapter 4. The total number of Ξ°'s in the apparatus is corrected for the albedo and matching effects not included in the Monte Carlo. It is then divided by the total number of generated background $\Xi^\circ \rightarrow \Lambda\pi^\circ$ decays. The normalization factor, 0.226 ± 0.004 is in good agreement with the normalization expected just by comparing the number of events outside the $\Xi^\circ \rightarrow \Lambda\gamma$ mass region on the histograms of Λ-γ mass for background Monte Carlo and data.

The branching ratio calculation is in Table 5.2 for the three different sets of final cuts in Sec. 4.30. The results, using the three different sets of cuts, are: $1.49\pm0.12 \times 10^{-3}$; $1.23\pm0.09 \times 10^{-3}$; and $1.27\pm0.11 \times 10^{-3}$. All the errors are statistical. The number of detected $\Xi^\circ \rightarrow \Lambda\gamma$ events for all the sets is simply the number of events on the background subtracted plots, Figs. 4.23, 4.25 and 4.28, in the mass region between 1.29 and 1.36 GeV, occupied by the signal Monte Carlo in Figs. 4.22b, 4.24b, and 4.27.

Possible systematic errors can be estimated by looking at the range of the results obtained by the three different sets of cuts. The range between the three results is 0.22 x 10^{-3}, mostly due to set #1, which differs more than #2 or #3. The Λ-γ mass plot for set #1, Fig. 4.22, was obtained through a different analysis than for sets #2 or #3. The Λ and γ momentum vectors used to calculate the parent mass came out of the coplanar kinematic fit X→Λγ, discussed in Sec. 4.24. The Λ and γ momentum vectors used to reconstruct the parent mass in sets #2 and #3 were the detected vectors described in Sec. 4.10. All three sets have in common the cuts requiring passing the 1-γ Ξ°→Λπ° fit and have a $\chi^2_{\Xi} >$ 12 (Sec. 4.22). Set #1 has only one other additional cut imposed, which is different from the cuts applied to sets #2 and #3, (set #2, in fact, is a subset of the cuts on set #3). The coplanar kinematic fit was capable of forcing poorly detected Ξ°→Λπ° events into the Ξ°→Λγ mass region. To generate the correct proportion of badly 'busted' Ξ°→Λπ° Monte Carlo events was very difficult. As such, the mass reconstruction and cuts used for set #1 give an estimate, when compared to the other sets, of the systematics due to the ability of the Monte Carlo to mock tails of distributions.

Another estimate of systematics can be obtained by looking at intermediate results. These results varied depending on the cuts used and the sophistication of the Monte Carlo simulations. Monte Carlos which did not mock the data exactly still gave branching ratios within the range of the results from the three final sets of cuts. For example, when the effect of γ self vetoing in the Primakoff target, discussed in Sec. 3.40, was not included, the Monte Carlo raised the geometric acceptances through the apparatus by 15% to 30%, depending on the target and the number of γ's. The number of Ξ°'s in the apparatus was then being overestimated. The Monte Carlo Ξ° decay vertex distribution clearly had an excess of events upstream of the Primakoff target. Yet, the result obtained with such a Monte Carlo was 1.1±0.3 x 10^{-3}. Another example involves the Λ P_t distribution. Before the $\Theta_{x,y}$ cuts were imposed, Sec. 3.32, the Λ P_t distributions in Figs. 3.18 and 4.10 showed a high tail, which was never successfully mocked by the background Monte Carlo. The high P_t events mapped to high Λ–γ mass, and caused some concern as to their origins (discussed briefly in Sec. 3.40). The Λ–γ mass plots after cuts similar to set #3 showed the same Ξ°→Λγ signal, but there was more background

present. Yet, the result obtained at that stage of the analysis was $1.3\pm0.2 \times 10^{-3}$, which is within the statistical error of the final results. These examples give an estimate of the maximum systematic error to be $\pm0.22 \times 10^{-3}$.

Since the mass plot for set #1 originates from a kinematic fit which forces the vectors, it should not be used as a measurement of the branching ratio, but only as an estimate of the systematics in the analysis. The final result is from set #3, which has all the final cuts imposed. The branching ratio measured, $\Xi^\circ \rightarrow \Lambda\gamma / \Xi^\circ \rightarrow \Lambda\pi^\circ$ is $1.27\pm0.11 \times 10^{-3}$ with a possible systematic error of 0.22×10^{-3}.

Table 1.2 gives some predictions for the branching ratio of this decay, which range from 10×10^{-3} to 0.12×10^{-3}. Of all the predictions made for the $\Xi^\circ \rightarrow \Lambda\gamma$ radiative decay, the one which has the closest value to this result is by Kamal and Verma[11], who predict a branching ratio of 1.36×10^{-3}. The measurement of one branching ratio, however, is not a definitive test for any one theory. The real test for any model is to be able to predict the branching ratios of all the radiative decays using inputs from any one decay. To do that, more complete information on all the hyperon radiative decays is needed. With the availability of high energy hyperon beams, high statistics experiments on hyperon radiative decays are possible; and the hyperon radiative decays will, in time, be well measured.

Table 5.1

Acceptances for $\Xi^\circ \rightarrow \Lambda\pi^\circ$ decays, when both γ's have been detected

acceptance	Primakoff target radiation length <0.15	0.5	1.0
β_1 geometric	0.03398±0.00008	0.03080±0.00006	0.02947±0.00004
β_2 analysis	0.0999±0.0004	0.0999±0.0004	0.0999±0.0004
TDC match correction	0.86±0.01	0.86±0.01	0.86±0.01
S7 albedo correction	0.61	0.61	0.61
totals	0.00178±0.00002	0.00161±0.00002	0.00154±0.00002
Number of $\Xi^\circ \rightarrow \Lambda\pi^\circ$ decays detected in the 2-γ data	8991±95	5506±74	15013±123
Total number of $\Xi^\circ \rightarrow \Lambda\pi^\circ$ decays estimated in the apparatus	5.051±0.078 M	3.412±0.062 M	9.749±0.150 M

Sum from the three target lengths.....18.212±0.180 M

Estimate the number of background $\Xi^\circ \rightarrow \Lambda\pi^\circ$ decays in the apparatus. Take the above total and multiply by the 1-γ TDC matching and albedo corrections:

$$18.212\pm0.180 \text{ M} \times 0.82\pm0.01 \times 0.78 = 11.648\pm0.183 \text{ M}$$

Divide this by the number of generated background Ξ° decays in the apparatus:

$$11.648\pm0.183 \text{ M} + 51.561\pm0.007 \text{ M} = 0.226\pm0.004$$

This factor of 0.226 was used to normalize the background Monte Carlo in Chapter 4 comparisons.

Table 5.2

Calculation of the branching ratio. All errors are added in quadrature.

	Set #1 cuts Fig 4.23	Set #2 cuts Fig.4.25	Set #3 cuts Fig. 4.28
α_1 geometric wieghted average	0.0643±0.0004	0.0643±0.0004	0.0643±0.0004
α_2 analysis cuts from Table 4.1	0.274±0.002	0.274±0.002	0.274±0.002
α_2 final cuts from Table 4.2	0.580±0.002	0.702±0.002	0.520±0.002
TDC matching	0.84±0.01	0.84±0.01	0.84±0.01
S7 albedo correction	0.78	0.78	0.78
total acceptances	0.0067±0.0001	0.0081±0.0001	0.0060±0.0001
Number of events	183±14	182±13	139±12
Number ÷ acceptance = total $\Xi^\circ \to \Lambda\gamma$ decays in the apparatus	27,313±2129	22,469±1629	23,167±2037
Branching ratio = total $\Xi^\circ \to \Lambda\gamma$ ÷ 18.212±0.180 M , the total $\Xi^\circ \to \Lambda\pi^\circ$ decays in the apparatus	0.00149±0.00012	0.00123±.00009	0.00127±0.00011

REFERENCES

(1) P. Petersen et al., Phys. Rev. Lett., **57**, 949 (1986)

(2) S.L. Glashow, J. Iliopoulos, L. Maiani, Phys. Rev., **D2**, 1285 (1970)

(3) M. Kawaguchi, K. Nishijima, Prog. Theor. Phys., **15**, 182 (1956)

(4) R.E. Marshak, Riazudin, C.P. Ryan : Theory of Weak Interactions in Particle Physics, New York, Wiley 1969

(5) M.A. Ahmed, G.G.Ross, Phys.Lett., **59B**, 293 (1975)
N. Vasanti, Phys.Rev., **D13**, 1889 (1976)

(6) A.I. Vainshtein, V.I. Zakharov, M.A. Shifman, Sov. Phys. JETP, **45**, 670 (1977)

(7) F.E. Close, H.R. Rubinstein, Nucl. Phys., **B173**, 477 (1980)

(8) K.G. Rauh, Z. Phys., **C10**, 81 (1981)

(9) D. Wu, J.L. Rosner, Phys. Rev., **D33**, 1367 (1986)

(10) F.J. Gilman, M.B. Wise, Phys. Rev., **D19**, 976 (1979)

(11) A.N. Kamal, R.C. Verma, Phys. Rev., **D26**, 26 (1982)
P. Eckert, B. Morel, preprint UGVA-DPT 1982/03-340

(12) M.K. Gaillard, B.W. Lee, Phys. Rev. Lett, **33**, 108 (1974)

(13) M.K. Gaillard, X.Q. Li, S. Rudaz, Phys. Lett, **158B**, 158 (1985)
Xue Qian Li, Ph. D. thesis, University of Minnesota, July 1985, unpublished

(14) C. Bernard, et al.,Phys. Rev. Lett., **55**, 2770 (1985)

(15) P.C. Petersen, Ph. D. thesis, "The Sigma-Lambda Transition Magnetic Moment", Rutgers University, 1985, unpublished

(16) Yeh et al., PRD, **10**, 3545 (1974)

(17) P. Skubic et al., Phys. Rev., **D18**, 3115 (1978)
A. Beretvas et al., Phys. Rev., **D34**, 53 (1986)

(18) P. Skubic Ph. D. thesis, "Neutral Strange Particle Production from Nuclear Targets by 300 GeV Protons", University of Michigan, (1977), unpublished

(19) J.F. Bartlett et al., "RT/RSX MULTI : Packages for Data Acquisition and Analysis in High Energy Physics", Topical Conf. on Computerized Data Acquisition Systems in Particle and Nuclear Physics, Sante Fe (1979)

(20) P. T. Cox et al., Phys. Rev. Lett., **46**, 877 (1981)

P. T. Cox, Ph. D. thesis, "The Magnetic Moment of the Cascade-Zero Hyperon", University of Michigan, (1980), unpublished

(21) A. Schiz et al., Fermilab pre-print "Hadron-Nucleus elastic scattering at 70, 125, and 175 GeV

(22) Review of Particle Properties, Phys. Lett., **170B**, (April 1986)

(23) R.L. Ford and W.R. Nelson, SLAC-210 (1978)

(24) G. Bathow et al., Nucl. Phys., **B20**, 592 (1978)